Facultad de Ciencias Físicas
Universidad Complutense de Madrid

Electronic and Spin Reconstruction at Complex Oxide Interfaces

Memoria presentada por

Flavio Yair Bruno

para optar al grado de Doctor en Ciencias Físicas

Director:

Jacobo Santamaría Sánchez-Barriga

Madrid, 2011

Cover: Artistic composition based on: X-ray magnetic circular dichroism signal of a [$LSMO_6/STO_2$] as a function of temperature, scanning transmission electron microscopy Z-contrast image of a [$LSMO_6/STO_{18}$], and X-Ray reflectivity spectra of a [$LSMO_8/STO_{10}$]. For an exact reproduction and a scientific explanation see figures 4.16 (a), 4.5 (a) and 4.3 (a).

“All in all it's just another brick in the wall”

R. Waters

Agradecimientos

Se acaban cuatro años de experimentos, algunos exitosos y otros fallidos. Pero todos ellos me han enseñado algo y para llevarlos a cabo siempre tuve la suerte de contar con la ayuda de los científicos (y amigos) que me rodeaban. Aquí va mi agradecimiento a todos ellos, que han puesto mucho más de lo que su posición les suponía.

Javi Barriocanal, te agradezco por la infinita paciencia que has tenido conmigo, por enseñarme a trabajar con el sputtering y por compartir tu entusiasmo cada día de medida en Grenoble. Alberto, por ser la persona "siempre disponible", por ayudar en cada detalle. Cristina, por las charlas y los cantos mientras trabajábamos en la sala blanca. Norbert, por la eficacia en las medidas magnéticas, por incomodarme y hacerme pensar cada vez que me preguntaste ¿y?. Fabián, por tu detallismo y perfeccionismo. Javi Tornos, por obligarme a agudizar mi ingenio cada vez que entraba en la sala blanca y te saludaba *amablemente*. Mirko, por enseñarme lo que es ser un italiano. Y a todos ustedes, por ser buenos amigos.

Quiero agradecer también a Carlos (y sus sermones), Zouhair, Rainer y Diego, por sus aportes y opiniones en la convivencia diaria. Durante estos años tuve la suerte de ayudar con sus trabajos de Máster y Proyectos Fin de Carrera a Elizabeth, Zalan, Marcos y Gabriel; gracias por su entusiasmo y por hacerme ver las dificultades del oficio de "profesor".

Muchos de los experimentos de esta tesis no hubieran sido posibles sin la colaboración de científicos de otras instituciones, que me han ayudado y han puesto a mi disposición sus equipos siempre que los he necesitado. Quiero agradecer a Mar García-Hernández por las medidas de magnetotransporte realizadas en el ICMM y por la estancia que realicé en mis comienzos en su laboratorio. A María Varela y a S.J. Pennycook por todas las medidas de STEM-EELS realizadas en el STEM-group en O.R.N.L. También quiero agradecer a los C.A.I. de la Universidad Complutense: Nacho, Julián y Emilio del C.A.I. de rayos x, y a Ana del C.A.I. de microscopía.

Durante este tiempo tuve la suerte de pasar cuatro meses en el grupo de óxidos funcionales de la “Unite Mixte de Physique CNRS/THALES” en Palaiseu, Francia. Agradezco a Cristina, Javi Villegas, Manu Bibes y Agnès Barthélémy por haberme dado esta oportunidad y por haberme ayudado en el día a día en su laboratorio.

Aunque no formen parte de esta tesis, los momentos fuera del laboratorio compartidos con familia y amigos han sido muy importantes en estos años. Quiero agradecerles a ellos, que con sus diversos puntos de vista y sus variopintas opiniones me han hecho una persona más completa y me han ayudado a afrontar la tesis. Gracias Nacho, Rocío, María, Emilio, Mario, Ángel y Johanna, por los viajes, las cervezas, las caminatas en las montañas (aunque no quisieran subir las Five Sisters), por su amistad. Gracias Andrés, por tus opiniones, por tu ejemplo de perseverancia, por la portada y la plantilla. A los muchachos que se quedaron en Argentina: al Primo, Negro, Andrés, Mariano, Catra, Moncho y Jorge.

Gracias a Edurne por enseñarme a tratar bien a la vida, gracias Granada.

Gracias a mi familia: a mis padres por educarme, a Silvina por poner en palabras claras las ideas que tanto me cuesta expresar y a Diego por saber entender desde la distancia, y a los dos por siempre tener razón en todo lo que dicen.

CONTENTS

1

Introduction

Many transition metal oxides (TMOs) are materials with strongly correlated electrons. What makes these materials interesting is that a broad range of different ground states occur in them; from metallic, semiconducting and insulating to colossal magnetoresistance, high temperature superconductivity, multiferroicity, etc. An important characteristic of these materials is the existence of several competing interactions, as exemplified by their complicated phase diagrams [1]. The complexity in these materials is a consequence of the interaction between several degrees of freedom – spin, charge, lattice and/or orbital – that are simultaneously active. Moreover, the fact that many of these different phases are close in energy originates the giant responses to small perturbations. These features make TMOs interesting materials to study. Many reviews cover in detail these topics [2-4].

The progress in thin-film deposition techniques (by sputtering, pulsed laser deposition and molecular beam epitaxy) in the 1980s and 1990s has made possible to grow thin layers of TMOs with epitaxial relationships with the underlying substrates, showing sometimes crystalline quality as good as that of single crystals. More importantly, it is now possible to combine different materials in a single heterostructure with high crystalline perfection. The region in which two different materials meet, called the interface, can be atomically sharp.

1 Interfaces

Electrons in conventional semiconductors, such as silicon, travel through the crystal lattice essentially as independent, free particles, barely interacting with one another. However, interfaces in semiconductor structures are the birthplace of a multitude of fascinating discoveries in fundamental science such as the Quantum Hall effect [5]. Moreover, practical devices of common use today like transistors, solar cells, etc, are based on interfaces between conventional semiconductors. If the combination of "boring" conventional semiconductors yields so much rich physics and enables so many new devices, it is natural to expect novel phenomena to emerge at complex oxide interfaces [6]. To better illustrate the phenomena that may influence the behavior of complex oxide interfaces we will describe a few examples below.

1.1 Charge leakage

In 2002 Ohtomo *et al.* studied heterostructures composed of $SrTiO_3$ (STO) and $LaTiO_3$ (LTO). STO is a band insulating material with an empty d-band in which the formal Ti oxidation state is 4+, whereas LTO has one d-electron per site (Ti^{3+}), however as a consequence of a strong Coulomb repulsion the material is a Mott insulator. The most illustrative result of the experiment was that when an atomic plane of LTO was inserted in a STO matrix electrons spread into the STO; this can be observed in Figure 1.1. In this figure the distribution of Ti^{3+} and La acquired by electron energy loss spectroscopy (EELS) are shown. The spread of the extra electron can be seen in the fractional Ti^{3+} signal that is clearly wider than the La signal. This delocalization of charge is an intrinsic property of the LTO/STO interface and is not a consequence of roughness or interface disorder. This "leakage" of electronic charge density out of the LTO and into the STO region is controlled mainly by the electrostatic potential arising from the La [7].

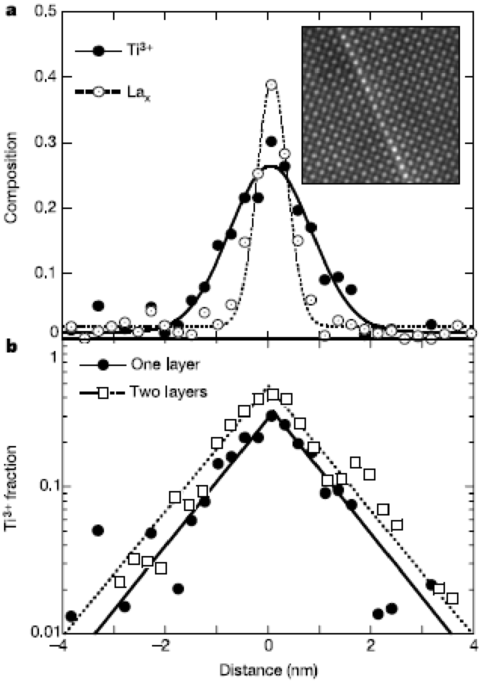

Figure 1.1. Spatial distribution of the Ti^{3+} signal in the vicinity of the $LaTiO_3$ layer and bilayer. (a) EELS profiles for La and Ti recorded across a $LaTiO_3$ monolayer. Inset, the ADF image for the monolayer. The La M edge is recorded simultaneously with the Ti L edge, yet the Ti^{3+} signal is considerably wider than that of the La. The absolute fractions of La and Ti^{3+} were calibrated from bulk $LaTiO_3$ and $SrTiO_3$. (b) The decay of the Ti^3 signal away from the $LaTiO_3$ monolayer of (a) as well as that from a bilayer. The tails of the Ti^{3+} signal for both structures fit an exponential decay with a decay length of $\lambda = 1.0 \pm 0.2$ nm. Adapted from ref [8].

This first example demonstrates that because transition metals like Ti may exist with different oxidation states, 3+ or 4+, close to the interface the electronic charge may spread or rearrange to screen the electrostatic potential that naturally arises at TMOs interfaces.

A second example of charge leakage is the case of $LaMnO_3/SrTiO_3$ interface. In this interface it was found that the charge leakage direction can be modified and even reversed by changing the LMO/STO thickness ratio. When this ratio is high the manganite is relaxed and doped with holes. However, at low ratios it is doped with electrons, and under epitaxial strain, which deeply modifies the magnetism and transport properties. This finding highlights the importance of relative layer thicknesses and/or epitaxial strain in controlling doping at the interface [9]. This second case demonstrates that another driving force for charge leakage is the epitaxial strain.

1.2 Conducting sheets at interfaces

Conducting sheets at interfaces between insulating materials represent an ideal configuration for electronic applications. The seminal discovery of conducting electron systems at interfaces between the band insulators $LaAlO_3$ and $SrTiO_3$ is a realization of this idea [10]. When this two materials are grown epitaxially along the (001) orientation, a polar discontinuity results at the interface (Figure 1.2). Two possible configurations arise at this interface which can be defined by the composition of the termination layer: $AlO_2/LaO/TiO_2$ (n-type) or $AlO_2/SrO/TiO_2$ (p-type). Unlike conventional semiconductors where each ion has a fixed valence, in complex oxides compositional roughening is not the only option for charge rearrangement: mixed valence charge compensation can occur if electrons can be redistributed at lower energy cost than redistributing ions. Conceptually, one can first construct the interface from neutral atoms and then allow ionization. Because $SrTiO_3$ can be regarded as a stacking of neutral $(SrO)^0$ and $(TiO_2)^0$ planes and $LaAlO_3$ as a stacking of charged $(LaO_2)^+$ and $(AlO_2)^-$ planes a polar discontinuity will always occur at sharp interfaces between these materials. This will result in the net transfer of half an electron per two-dimensional unit cell from $LaAlO_3$ to $SrTiO_3$ across the interface. This process leaves the overall structure neutral, with the Ti ion at the interface becoming $Ti^{3.5+}$ [11].

This third example highlights the role played by polar discontinuities at complex oxide interfaces. As mentioned in the preceding examples this may be another driving force behind the charge transfer phenomena.

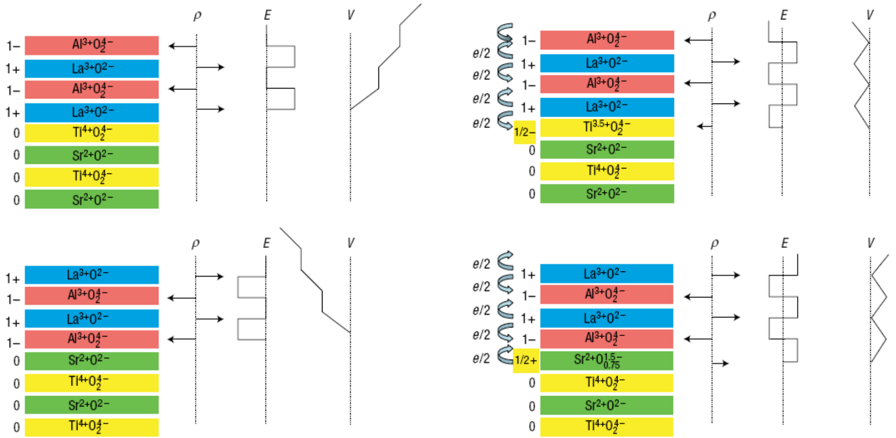

Figure 1.2. The polar catastrophe illustrated for atomically abrupt (001) interfaces between $LaAlO_3$ and $SrTiO_3$. (a) The unreconstructed interface has neutral (001) planesin $SrTiO_3$, but the (001) planes in $LaAlO_3$ have alternating net charges (ρ). If the interface plane is $AlO_2/LaO/TiO_2$, this produces a non-negative electric field (E), leading in turn to an electric potential (V) that diverges with thickness. (b) If the interface is instead placed at the AlO2/SrO/TiO2 plane, the potential diverges negatively. (c) The divergence catastrophe at the $AlO_2/LaO/TiO_2$ interface can be avoided if half an electron is added to the last Ti layer. This produces an interface dipole that causes the electric field to oscillate about 0 and the potential remains finite. The upper free surface is not shown, but in this simple model the uppermost AlO_2 layer would be missing half an electron, which would bring the electric field and potential back to zero at the upper surface. The actual surface reconstruction is more complicated [12].(d) The divergence for the $AlO_2/SrO/TiO_2$ interface can also be avoided by removing half an electron from the SrO plane in the form of oxygen vacancies. Adapted from ref [11].

1.3 Covalent bonds

The interface between $YBa_2Cu_3O_7$ (YBCO) and $La_{0.7}Ca_{0.3}MnO_3$ (LCMO) has been widely investigated [13-15]. This interface is very interesting because it provides benchmark for the study of proximity effect between a high temperature superconductor (YBCO) and a half metallic ferromagnetic material (LCMO). In YBCO holes predominantly occupy the Cu $d_{x^2-y^2}$ orbital. However at the YBCO/LCMO interface holes are found both in the $d_{x^2-y^2}$ and in the $d_{3z^2-r^2}$. Chakhalian *et al.* explained their results by postulating the hybridization of the Cu $d_{3z^2-r^2}$ and the Mn $d_{3z^2-r^2}$ via the oxygen ion [15]. This process is illustrated in Figure 1.3. As a consequence of the hybridization process “molecular orbitals” are formed. The charge transfer process occurs when the antibonding (AB) molecular orbital crosses the Cu $d_{x^2-y^2}$ level, in this case a hole is “created” at the

$d_{3z^2-r^2}$ AB molecular orbital. This orbital reconstruction at the interface also affects the magnetic properties of this system. YBCO is and antiferromagnetic material. Close to the interface, the magnetic interaction between Mn and Cu caused by the hybridization between these atoms produces the existence of a finite ferromagnetic moment in the Cu atoms [14] that is not found on the bulk material.

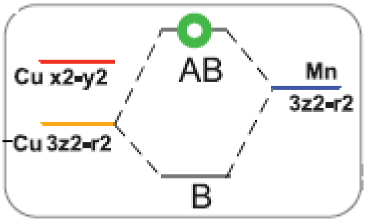

Figure 1.3. Orbital level scheme at the interface, including extended bonding (B) and antibonding (AB) "molecular orbitals" formed by hybridized Cu and Mn $d_{3z^2-r^2}$ orbitals. The hole is indicated as the green circle. Adapted from ref [15].

This fourth example of interface phenomena has introduced us to two new concepts. On the one hand, orbitals that point towards the interface like $d_{3z^2-r^2}$ $d_{xz, yz}$ may hybridize and form molecular orbitals; on the other hand this hybridization may have important consequences such us charge transfer and magnetic interactions.

1.4 Discussion

We have discussed examples of interfacial phenomena, these examples allow us to identify some key parameters that determine these phenomena. Charge leakage occurs at complex oxide interfaces and may have different origins: covalent bonding, the screening of atomic potentials, strain or polar discontinuities. Also we have mentioned the case of magnetic interactions at the interface between different transition metal atoms as a consequence of hybridized orbitals. Charge leakage in different interfaces will be discussed in chapters 3 and 4, and magnetic interactions at the interfaces will be discussed in chapters 4 and 5.

2 Thesis Outline

- Chapter 2: in this chapter the experimental techniques that are used throughout the thesis are briefly explained. Details on the growth method, magnetotransport measurements, x-ray diffraction, and x-ray magnetic circular dichroism are given.

- Chapter 3: In this chapter we study the electronic reconstruction that takes place at the $Sm_2CuO_4/LaFeO_3$. The Sm_2CuO_4 is the parent compound of the n-type high temperature superconductors. The selected composition of SCO is insulating, as is also LFO. In the chapter we demonstrate by different spectroscopical techniques that at the interface with $LaFeO_3$ the material becomes electron doped, moreover this interface presents a metallic character.

- Chapter 4: deals with the electronic and spin reconstruction that takes place at the $La_{0.7}Sr_{0.3}MnO_3/SrTiO_3$ interface. $La_{0.7}Sr_{0.3}MnO_3$ is a metallic and ferromagnetic material with Curie temperature above room temperature. However, magnetic and metallic characters of this material close to the interface with $SrTiO_3$ are depressed in a so called “dead layer”. In this chapter we discuss how the magnetic correlations at this interface may be at the origin of the dead layer problem.

- Chapter 5: we analyze the magnetotransport properties of $La_{0.7}Sr_{0.3}MnO_3/LaFeO_3/La_{0.7}Sr_{0.3}MnO_3$ magnetic tunnel junctions, and discuss the possibility of spin filtering by an induced magnetic moment in the antiferromagnetic barrier.

- Chapter 6: in this chapter we study the transport properties of $La_{0.8}Sr_{0.2}CoO_3/SrTi_{0.98}Nb_{0.02}O_3$ heterojunctions. We study the current-voltage, capacitance-voltage and capacitance-frequency characteristics and employ different models to obtain the built-in potential barrier at the interface.

3 References

[1] E. Dagotto, Science **309**, 257 (2005).

[2] E. Dagotto, T. Hotta, and A. Moreo, Phys. Rep. **344**, 1 (2001).

[3] M. Imada, A. Fujimori, and Y. Tokura, Rev. Mod. Phys. **70**, 1039 (1998).

[4] P. Lee, N. Nagaosa, and X. Wen, Rev. Mod. Phys. **78**, 17 (2006).

[5] K. Klitzing, G. Dorda, and M. Pepper, Phys. Rev. Lett. **45**, 494 (1980).

[6] J. Mannhart, and D. Schlom, Science **327**, 1607 (2010).

[7] S. Okamoto, and A. Millis, Nature (London) **428**, 630 (2004).

[8] A. Ohtomo, D. A. Muller, J. L. Grazul, and H. Y. Hwang, Nature (London) **419**, 378 (2002).

[9] J. Garcia-Barriocanal, F. Y. Bruno, A. Rivera-Calzada, Z. Sefrioui, N. M. Nemes, M. Garcia-Hernández, J. Rubio-Zuazo, G. R. Castro, M. Varela, S. J. Pennycook, C. Leon, and J. Santamaria, Adv. Mater. **22**, 627 (2010).

[10] A. Ohtomo, and H. Y. Hwang, Nature (London) **427**, 423 (2004).

[11] N. Nakagawa, H. Hwang, and D. Muller, Nature Mater. **5**, 204 (2006).

[12] R. J. Francis, S. C. Moss, and A. J. Jacobson, Phys. Rev. B **64**, 235425 (2001).

[13] V. Pena, Z. Sefrioui, D. Arias, C. Leon, J. Santamaria, J. L. Martinez, S. G. E. t. Velthuis, and A. Hoffmann, Phys. Rev. Lett. **94**, 057002 (2005).

[14] J. Chakhalian, J. Freeland, G. Srajer, J. Strempfer, G. Khaliullin, J. Cezar, T. Charlton, R. Dalgliesh, C. Bernhard, and G. Cristiani, Nature Phys. **2**, 244 (2006).

[15] J. Chakhalian, J. Freeland, H. Habermeier, G. Cristiani, G. Khaliullin, M. van Veenendaal, and B. Keimer, Science **318**, 1114 (2007).

2

Experimental Techniques

1 Sample preparation

Samples are prepared by sputter deposition in high O_2 pressure. This method is based on the ballistic impact of atoms against a substrate after being removed from a material source. The sputtered ions come from targets made of the stoichiometric compound while the oxygen plays the role of the sputtering element. In our case the substrate is placed on a heater plate below the targets. The growth takes place inside a chamber in which a high vacuum of about 10^{-6} mbar is previously realized. The chamber, shown in Figure 2.1, is connected to a turbo-molecular pump supported by a membrane pump. A constant oxygen flow is injected and controlled by a system of needle valves. Since the sputter yield depends on the energy of the incoming O_2 ion and the source atom species, the material removed from the target will deposit on the substrate in a manner which strongly depends on several controllable parameters such as the temperature of the substrate, the applied RF power and the pressure inside the chamber. In order to grow epitaxial oxide heterostructures high temperature and pressure are usually required. All the samples studied in this work have been grown on $SrTiO_3$ substrate (100)-oriented. The high oxygen pressure (2.9 mbar) applied during the deposition, favors a complete thermalization of the extracted species and at the same time prevents them from back-sputtering and loss of oxygen in the final crystal structure. The substrate temperature is kept constant at a temperature ranging from 650ºC to 900ºC. Under these conditions the deposition rate is slow (0.3nm/min) and ensures the epitaxial growth of the sample. To preserve the optimal oxygen content of the structure an *in-situ* annealing at 900 mbar O_2 pressure is necessary. The procedure is slightly different depending on the grown material.

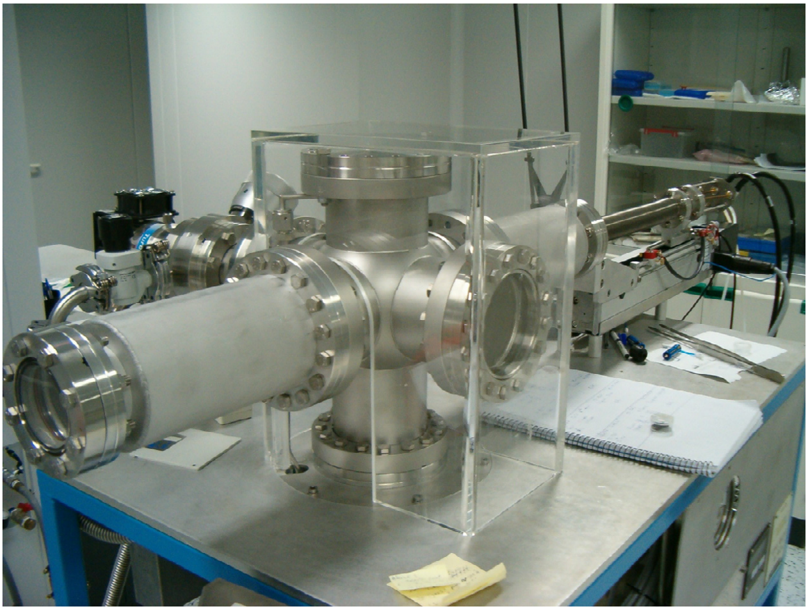

Figure 2.1. View of the sputtering chamber. The targets are mounted on a remote controlled arm to switch between the different materials.

2 Structural characterization: XRR, XRD

X-ray reflectivity (XRR) and diffraction (XRD) patterns allowed determining the thickness and the structural quality of our samples. XRR and XRD measurements have been carried out at CAI de Difracción de Rayos-X (UCM), with a Philips X'pert MRD diffractometer, using a Cu tube as X-ray source (λ_x= 0.15418nm) operating at 45kV an 40mA. Selected samples were also characterized with synchrotron x-rays at the beamline BM25 of E.S.R.F. (Grenoble, France).

2.1 X-ray reflectivity

The coherent and collimated radiation coming from an X-ray source is reflected at the interface between layers with different electronic densities (the substrate, the film, the air). The different refractive indexes induce a change in the path length of the X-ray and consequently a constructive/destructive interference of the different reflected beams. In an analogous way, the interference resulting from a layered structure produces oscillation in the reflectivity pattern. This pattern is obtained by measuring the reflected intensity as a function of the incident angle (2θ) through a detector which is set in θ-2θ (Bragg) geometry with respect to the source (see Figure 2.2).

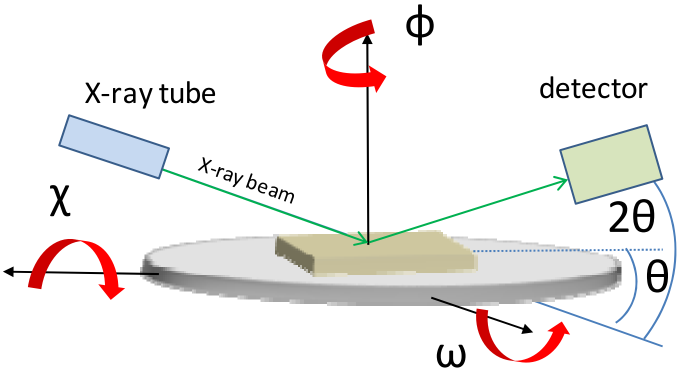

Figure 2.2. Schematic diagram of the θ-2θ geometry

Reflectivity scans showed in this work are usually taken up to an angle of $2\theta \sim 10$ degrees. In this range of angle we are able to see finite size oscillations ($2\theta<7^{\circ}$), related to the total thickness of the sample as shown in Figure 2.3. The period of the finite size oscillations is inversely related to the thickness d of the whole sample. By indexing the position of the maxima and minima (m=1,2..) we can calculate the total thickness using the formula:

$$\sin^2\theta = \left[\frac{(m-k)\lambda_x}{2d}\right] + 2\delta\,, \tag{2.1}$$

where k=0 correspond to a minimum, k=1/2 to a maximum and δ is the real part of the refraction index:

$$n = 1 - \frac{\rho_n r_e \lambda_x}{2\pi}(f_0 + \Delta f' - i\Delta f'') = 1 - \delta + i\beta\,, \tag{2.2}$$

where ρ_n is the electronic density, r_e is the electron radius, f_0 is the atomic dispersion factor, *Δf'* and *Δf''* are corrections due to the anomalous dispersion [1, 2]. In Figure 2.3 we show a representative reflectivity curve of a thin film.

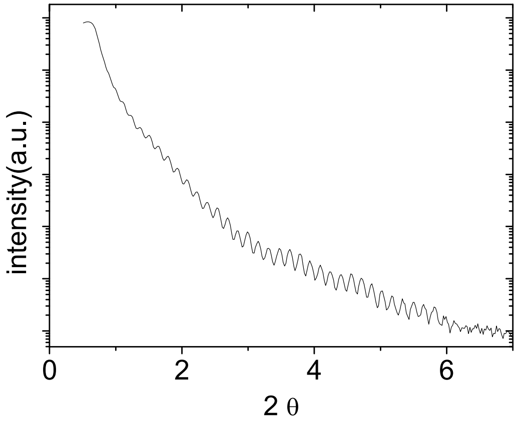

Figure 2.3. Reflectometry scan from a 57 nm thick $La_{0.8}Sr_{0.2}CoO_3$ thin film.

2.2 X ray diffraction

Atomic layers in a crystal are separated by a distance *d*. Specular reflected X-rays will travel different distances due to this separation and will yield constructive interference if the difference in path is an integer multiple of the X-ray wavelength. For an epitaxial structure of different materials, a diffraction scan carried out in *θ-2θ* geometry, after optimizing around one of the (00*l*) diffraction peaks of the substrate will show only the Bragg peaks of the same family [3].Thus the diffraction condition described by the Bragg law:

$$2d_{hkl}\sin\theta = n\lambda_x \tag{2.3}$$

can be used for determining the lattice spacing of a set of crystallographic planes, parallel to the film plane, we will usually call this distance the lattice parameter c. In Figure 2.4 (a) we can see a diffraction scan from a $La_{0.8}Sr_{0.2}CoO_3$ thin film grown on STO substrate where the diffraction peaks are labeled. In the case of multilayers the characteristic length scales are: the lattice spacing of the constituent material, and the modulation wavelength Λ defined as the thickness of the bilayer that is repeated to form the superlattice. This additional periodicity will cause new diffraction peaks to appear which can be indexed about the average lattice constant $\overline{d}$ following [4]

$$2\frac{\sin\theta}{\lambda_x} = \frac{1}{\overline{d}} \pm \frac{m}{\Lambda}, \tag{2.4}$$

where m is an integer that labels the order of the satellite around the main Bragg peak and $\overline{d} = \Lambda / (N_A + N_B)$, where N_A and N_B are the number of atomic planes of material A and B in one bilayer. In Figure 2.4 (b) we show the diffraction spectra of a $[LSCO_{14}/STO_5]_8$ superlattice were the superlattice Bragg peaks (labeled as 0) and the superlattice satellite peaks are labeled according to equation 2.4.

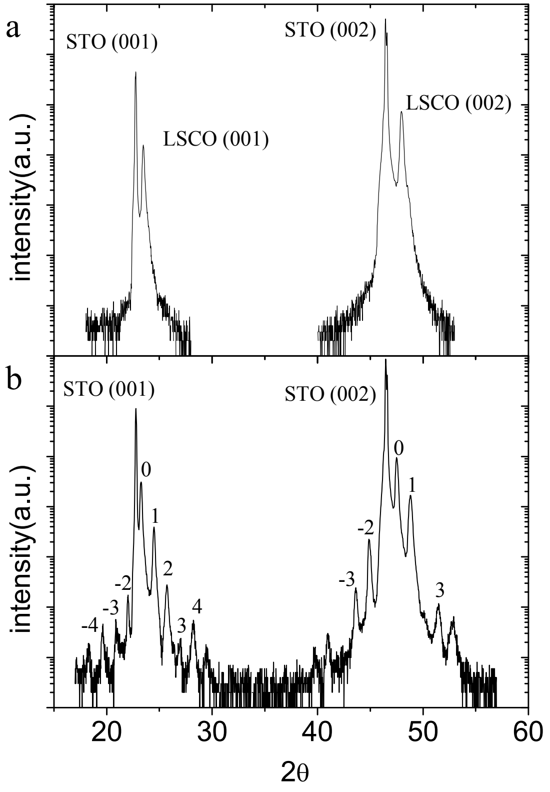

Figure 2.4. Diffraction spectra corresponding to (a) a 57 nm thick $La_{0.8}Sr_{0.2}CoO_3$ thin film and (b) a $[LSCO_{14}/STO_5]_8$ superlattice. Both samples are grown in STO (001 substrates).

3 Magnetotransport measurements

3.1 Resistance measurements

For our low temperature resistance measurements we used a closed-cycle Cryophysics helium refrigerator which works with the expansion of highly-pure He-gas compressed in a Gifford McMahon cycle. The expansion through the capillaries undergoes two steps at 50K and at 8.5K. The sample is mounted onto a cooled copper piece in contact with the second cooling step. The system is evacuated by a rotary pump capable of a pressure down to 10mTorr, measured with a Pirani vacuum sensor. A silicon diode thermometer is in contact with the sample holder calibrated for measuring between 10 and 325K. The system is also equipped with a heater controlled by a Lake Shore 330-11 temperature controller which permits to control the sample's temperature between room temperature and 9K with a 10-mK accuracy. The resistance was measured using the Van der Pauw four-point method [5] to eliminate any contribution given by the in-series contact resistance. Four electrical contacts were made on the surface of the sample by evaporation of silver and then connected to the low-noise wiring by indium. The instruments used were a Keithly 224 current source, capable of stabilizing a current supplied between 5nA and 100mA and a Keithly 2182 nanovoltmeter.

3.2 Magnetic measurements

3.2.1 SQUID magnetometry

The magnetometry data for this thesis have been taken using a Quantum Design Magnetic Property Measurement System (MPMS) SQUID magnetometer of the Magnetism and Transport Laboratory at ICMM (Madrid). The MPMS system comprises of two main sections: the Dewar, probe and SQUID assembly, and the electronic control system. The probe contains a high precision temperature control system, allowing measurements between 1.9K and 400Kwith an accuracy of 0.01K, and superconducting electromagnet, giving a field of up to 50kOe with an accuracy of up to 1Oe (Figure 2.5). The Dewar consists of an inner liquid helium reservoir and outer liquid nitrogen jacket, to reduce excessive liquid helium boil off. The liquid helium is used both for maintaining the electromagnet in a superconducting state and for cooling the sample space. Samples are mounted within a plastic straw and connected to one end of a sample rod which is inserted into the Dewar/probe. The other end is attached to a stepper motor which is used to position the sample within the center of the SQUID pickup coils. The measurement of the magnetic moment is done using the DC Josephson effect. In fact there are two Josephson junctions in parallel in a superconducting loop. To obtain DC measurements the sample is moved through the coils in discrete steps. The circulating current produced by a flux change is then detected by the use of a measuring current. The pickup coils are configured as highly balanced second-derivative coils, approximately 3cm long. The coils reject the applied field from the superconducting magnet to a resolution of 0.1%.

3.2.2 VSM magnetometry

We also performed magnetic measurements using a Vibrating Sample Magnetometer (VSM). The VSM measures the difference in magnetic induction between region of space with and without the specimen. It therefore gives a direct and absolute measure of the magnetization. The magnetic moment of the sample is measured according to Faraday's law. The sample oscillates sinusoidally inside a small pick-up coil with a frequency of about 40Hz. The induced voltage due to $E = - d\varphi/dt$ is detected with the lock-in technique and converted to magnetic moment with an instrument specific calibration factor. It allows for the rapid measurement of M vs. T and M vs. H data with a useful sensitivity of approx. 10^{-6} emu. The sample is mounted on a diamagnetic stick fixed to a carbon rod (see Figure 2.5). While SQUID magnetometry allows precise control of the magnetic field and high sensitivity measurements, VSM magnetometry provides very rapid measurements. The samples studied in this work showed quite high magnetic moment, allowing a comparable response from SQUID and VSM.

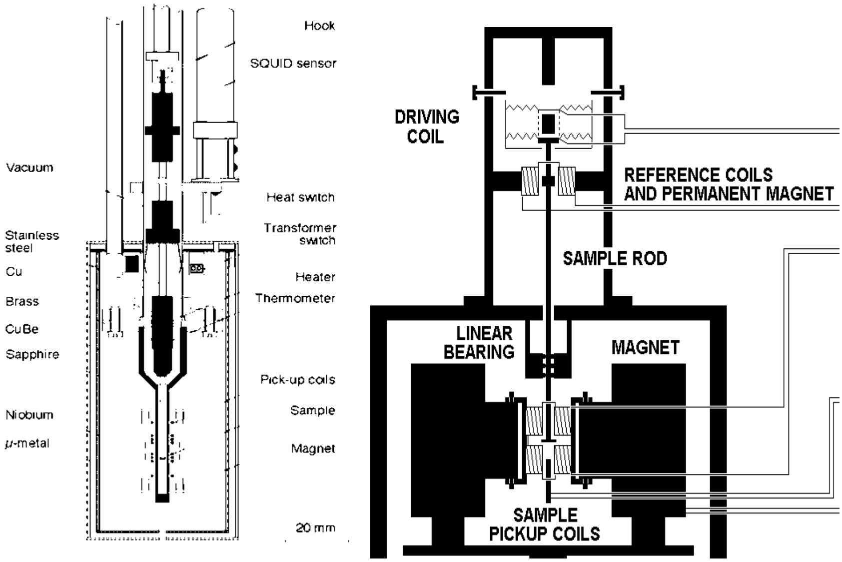

Figure 2.5. Diagrams of SQUID (left) and VSM (right) magnetometers.

3.2.3 Ferromagnetic Resonance (FMR)

Ferromagnetic resonance spectroscopy (FMR) can be used to measure the effective magnetic field within a sample, including the contributions of both magnetic anisotropy and magnetostatic interactions. If a magnetization vector is subject to a static field and a perpendicularly applied pump field, resonance will occur at a frequency more or less proportional to the strength of the static field. The microwave power absorbed by the magnetic sample as a function of frequency will typically be a Lorentzian centered at resonance. The FMR signal is measured by monitoring the microwave losses as a function of the applied dc-field. The data of this thesis have been taken using a 8.9 GHz JEOL ESR X-band electron spin resonance spectrometer, equipped with a liquid nitrogen cryostat, of the Dept. of Physics, University of Technology and Economics (Budapest). FMR is one of the best techniques to determine the magnetic anisotropy constants up to sixth order. Surface/interface and volume magnetic anisotropies in ultrathin films can be quantitatively determined with a resolution better than one μeV. One major advantage of this technique is the low excitation energy (microwave quanta) by which the magnetic ground state properties are probed. Also, the dynamic behavior i.e. the magnetic relaxation rate can be probed in a time window of typically few hundred picoseconds.

4 X-ray Magnetic Circular Dichroism (XMCD)

X-ray magnetic circular dichroism (XMCD) spectroscopy makes use of high energy X-rays to explore the structural and magnetic properties of matter. It was first suggested by Erskine and Stern [6] and pioneered by Schütz et al. [7]. It has several capabilities not afforded by traditional magnetic techniques. Its foremost strengths are the element-specific, quantitative determination of spin and orbital magnetic moments and their anisotropies. An XMCD experiment usually consists of illuminating the sample with intense circularly polarized X-rays produced in synchrotron sources and tuning the X-ray energy on the absorption edge of a specific element. The difference between left and right circularly polarized X-ray absorption cross section (the dichroism signal) of a ferromagnetic or a ferrimagnetic material is directly proportional to the mean value of the macroscopic magnetic moment.

4.1 X-ray absorption spectroscopy (XAS): chemical environment

X-ray absorption spectroscopy (XAS) studies the effect of photon absorption on the matter. It is not necessarily dependent on the incident photon spin. In X-ray absorption a photon is absorbed by an atom giving rise to a transition of an electron (a photoelectron) from a core state to an empty state above the Fermi level. The absorption cross-section depends on the energy and on the measured element. To excite an electron in a given core level, the photon energy has to be equal or higher than the energy of this core level which is characteristics of the element [8]. When this energy level is crossed, a sudden jump in the absorption intensity is observed (Figure 2.6). Excitation of photoelectrons gives rise to the creation of core holes. These vacancies present an unstable condition for the atom. As the atom returns to its stable condition, electrons from the outer shells are transferred to the inner shells giving off, during the process, a characteristic X-ray whose energy is the difference between the two binding energies of the corresponding shells. The emitted X-rays produced from this process can be detected in the fluorescence yield (FY) mode. The secondary X-ray excitations can promote additional electronic transitions; in fact when a vacancy is created in the L-shell by the excitation, an electron from the M or N shell “jumps in” to occupy the vacancy Figure 2.7.

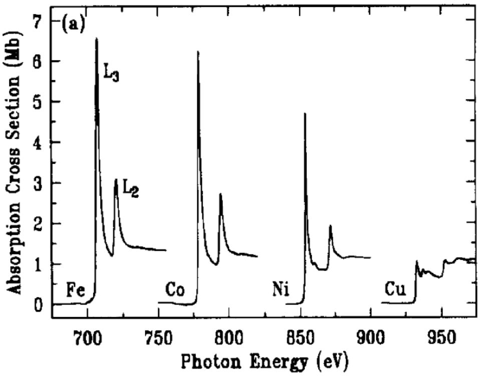

Figure 2.6. X-ray absorption spectra recorded by total electron yield detection near the L_2, and L_3 edges for Fe, Co, Ni, and Cu metal, showing the existence of white lines for Fe. Co, and Ni and its near-absence for Cu, due to its nearly filled d shell. Adapted from ref [9]

In this process, it emits X-rays and in turn, produces a vacancy in the M or N shell. In transition metals the *d*-orbitals are partially filled and close to the Fermi level. If an X-ray has just sufficient energy to excite a core level, then the resultant photoelectron will leap into unoccupied states above the Fermi level Figure 2.7(b). On the other hand when the excitation energy from the inner atom is transferred to one of the outer electrons, this (Auger) electron is ejected from the atom. The energy spectrum of the emitted electrons consists of well defined lines due to photoelectrons and Auger electrons on top of a background due to secondary electrons. These low-energy secondary electrons resulting from inelastic collisions of initially excited photoelectrons or Auger electrons, give rise to a major portion of the electron emission, and the sample can be regarded as an effective electron multiplier. Monitoring the total electron yield (TEY), i.e. all electrons emitted from the sample, offers the simplest mode for detecting the photo-absorption process. It is often easier to measure not the emitted electrons directly but their complement given by the sample drain current flowing into the sample. The transitions are usually labeled according to the position of the exited electron; transition from the $p_{1/2}$ level would lead to the L_2 line, while transition from $p_{3/2}$ would lead to the L_3 line.

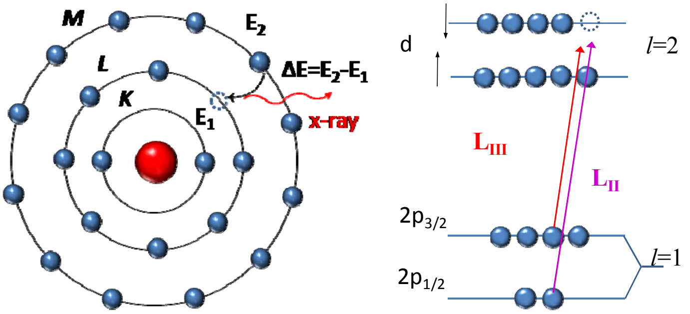

Figure 2.7. Schematic diagram of fluorescence process (left) and electronic transition (right).

Spectra taken from a single metal mainly show two broad peaks, reflecting the width of the empty *d*-bands (Figure 2.6). In general the oxide spectra are more complicated exhibiting multiplet structure due to the electrostatic interactions between 2p core-hole and 3d valence electrons and 2p core-hole spin-orbit interactions, as well as by the local crystal fields and the hybridization with the O 2*p* ligands [10, 11].

4.2 XMCD: magnetic information

Constraints on the transition are represented by the selection rules. Because of the $\Delta J=0,\pm 1$ dipole selection rule the 1/2→ 5/2 (or inverse) transition is forbidden (spin flips are forbidden in electric dipole transition), spin-up (spin-down) photoelectrons from the *p* core shell can only be excited into spin-up (spin-down) *d* hole states. Hence the spin-split valence shell acts as a detector for the spin of the excited photoelectron and the transition intensity is simply proportional to the number of empty *d*-states of a given spin [12]. The quantization axis of the valence shell "detector" is given by the magnetization direction. When circular polarization is applied to the photon beam, the electromagnetic field vector turns around the direction of the propagation vector. The difference between the transition probability for left and right circularly polarized light gives the circular magnetic dichroism. Since the dipole selection rule is different for right (RCP) and left (LCP) circularly polarized light, the respective components may be absorbed differently, depending on the nature of the two magnetic band states (see Figure 2.8). The emitted radiation will reflect this imbalance and will be elliptically polarized with the major polarization axis rotated relative to that of the incident light. The most common way of measuring XMCD in the soft x-ray region is total electron yield (TEY), because of the easy experimental setup and high signal-to-noise ratio compared to fluorescence yield.

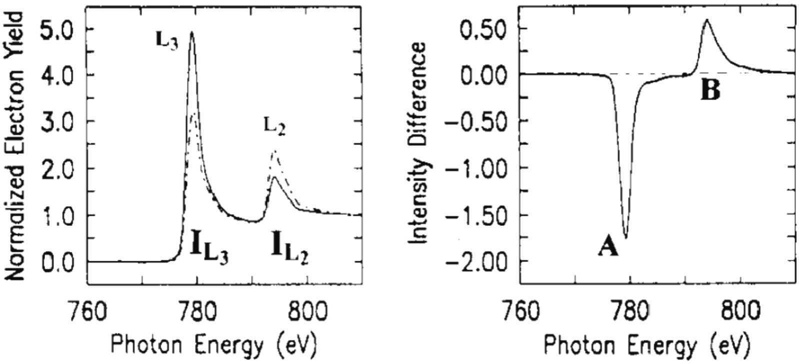

Figure. 2.8: (Left) Normalized X-ray magnetic circular dichroism spectra at the L_3 and L_2 edges for Co metal. The original spectra have white line intensities I_{L3} and I_{L2} which depend on the relative orientation of photon spin and magnetization direction, shown solid for parallel and dashed for antiparallel alignment. (Right) The difference spectrum gives dichroism intensities ,A < 0 and B > 0 at the L_{III} and L_{II} edges, respectively.

5 Scanning Transmission Electron Microscopy

A scanning transmission electron microscope (STEM) is a type of transmission electron microscope (TEM). All the STEM measurements in this thesis were done at the S.J. Pennycook group (STEM Group) of the Oak Ridge National Laboratory by Maria Varela and collaborators.

In the scanning-transmission electron microscope (see Figure 2.9), a field-emission source and strong electromagnetic lenses are used to form a small probe that can be raster-scanned across the specimen [13]. A dark-field image, representing transmitted electrons scattered through relatively large angles, is formed by feeding the signal from a ring-shaped (annular) detector to a display device scanned in synchronism with the probe scan. Electrons scattered through smaller angles enter a single prism spectrometer, which produces an energy-loss spectrum (EELS spectrum) for a given position of the probe on the specimen [14]. Inserting a slit in the spectrum plane then gives an energy-filtered image, obtained this time in serial mode. Alternatively, the whole spectrum is read out at each probe position (pixel), resulting in a large spectrum-image data set that can be processed off-line [15]. The image obtained in the annular detector is called annular dark-field (ADF) image. The contrast is directly related to the atomic number (Z-contrast images). The fact that the Z-contrast images are directly interpretable makes this technique very appealing. With modern microscopes it is possible to obtain an EELS spectrum in each atomic column, this makes this technique a powerful tool to investigate the chemical composition of interfaces. Moreover EELS is sensitive to the oxidation state of the atoms, thus is a powerful tool to investigate transition metal oxides where the physical properties of the system are directly related to the oxidation state.

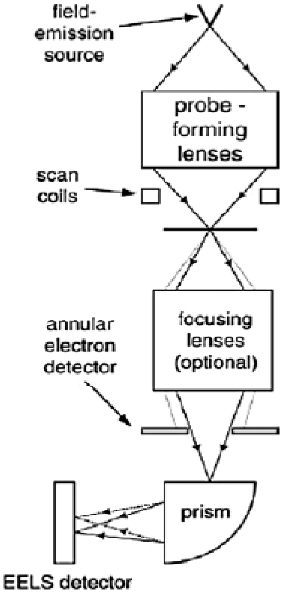

Figure 2.9. Schematic of a scanning-transmission electron microscopy system. From ref [13]

6 Atomic Force Microscopy

The Atomic Force Microscopy (AFM) images of chapter 3 of this thesis were obtained with a Veeco multimode Scanning Probe Microscope equipped with Veeco RTESP tip. This microscope is installed in the “Centro de Microscopía Electrónica Luis Bru” de la Universidad Complutense de Madrid. AFM resistance maps (CT-AFM) and topography images shown in chapter 5 were performed in a modified Nanoscope IV (Veeco) microscope modified to perform local intensity measurements. This microscope is installed at the “Unite mixte de physique CNRS/THALES”, Palaiseu (France).

7 References

[1] D. M. Kelly, E. E. Fullerton, J. Santamaria, and I. K. Schuller, Scripta Metall. Mater. **33**, 1603 (1995).

[2] O. Nakamura, E. E. Fullerton, J. Guimpel, and I. K. Schuller, Appl. Phys. Lett. **60**, 120 (1992).

[3] A. Guinier, *X-ray diffraction in crystals, imperfect crystals, and amorphous bodies* (Dover Publications, 1994).

[4] E. E. Fullerton, I. K. Schuller, H. Vanderstraeten, and Y. Bruynseraede, Phys. Rev. B **45**, 9292 (1992).

[5] L. Van der Pauw, Philips Technical Review **20**, 220 (1958).

[6] J. L. Erskine, and E. A. Stern, Phys. Rev. B **12**, 5016 (1975).

[7] K. H. Müller, K. Dörr, T. Walter, M. Sahana, K. Brand, and L. Schultz, J. Magn. Magn. Mater. **242-245**, 447 (2002).

[8] F. Groot, and J. Vogel, Neutron and X-ray Spectroscopy, 3 (2006).

[9] J. Stöhr, J. Electron. Spectrosc. Relat. Phenom. **75**, 253 (1995).

[10] B. Thole, P. Carra, F. Sette, and G. Van der Laan, Phys. Rev. Lett. **68**, 1943 (1992).

[11] T. Burnus, Z. Hu, H. H. Hsieh, V. L. J. Joly, P. A. Joy, M. W. Haverkort, H. Wu, A. Tanaka, H. J. Lin, C. T. Chen, and L. H. Tjeng, Phys. Rev. B **77**, 125124 (2008).

[12] C. Kao, J. B. Hastings, E. D. Johnson, D. P. Siddons, G. C. Smith, and G. A. Prinz, Phys. Rev. Lett. **65**, 373 (1990).

[13] R. Egerton, Rep. Prog. Phys. **72**, 016502 (2009).

[14] N. Browning, D. Wallis, P. Nellist, and S. Pennycook, Micron **28**, 333 (1997).

[15] C. Jeanguillaume, and C. Colliex, Ultramicroscopy **28**, 252 (1989).

3

Electron Doping at Epitaxial Interfaces

One of the key ideas behind the emerging properties of complex oxides interfaces is that the electronic reconstruction that takes place at the interface profoundly modifies the properties of the strongly correlated materials that form the interface. One of the clearest manifestations of this electronic reconstruction is the modification of the doping level of the materials near the interface as a consequence of the charge transfer process between them. [1-3]. It was recently proposed to use this charge transfer phenomena to obtain electronic doping in heterostructures without introducing the inevitably quenched disorder that accompanies the chemical doping. In particular it was proposed to obtain an electron doped high temperature superconductor (HTSC) at the interface between the Mott insulating parent compound of the HTSC and a suitable material that would act as the charge donor [4]. In this chapter we will study the possibility of obtaining n-type doped Sm_2CuO_4 at the interface formed with $LaFeO_3$ through charge transfer.

1 Introduction

While there are hundreds of copper oxide high-Tc compounds [5], they all share a layered structure made up of one or more copper oxygen planes. They all fit into a universal phase diagram shown in Figure 3.1(a). The so-called parent Mott insulator. In the copper-oxygen layer there is an odd number of electrons per unit cell. More specifically, the copper ion is doubly ionized and is in a d^9 configuration so that there is a single hole in the d shell per unit cell. According to band theory, the band is half-filled and should be metallic. Nevertheless, there is a strong repulsive energy cost when putting two electrons (or holes) on the same ion, and when this energy dominates over the hopping energy, the ground state is an insulator due to strong correlation effects. The parent compound can be doped by substituting some of the trivalent Nd by tetravalent Ce. The result is that x electrons are added to the Cu-O plane in $Nd_{2-x}Ce_xCuO_4$, which is called electron doping [6]. In the compound $La_{2-x}Sr_xCuO_4$, the reverse happens in that x holes are added to the Cu-O plane, which is called hole doping.

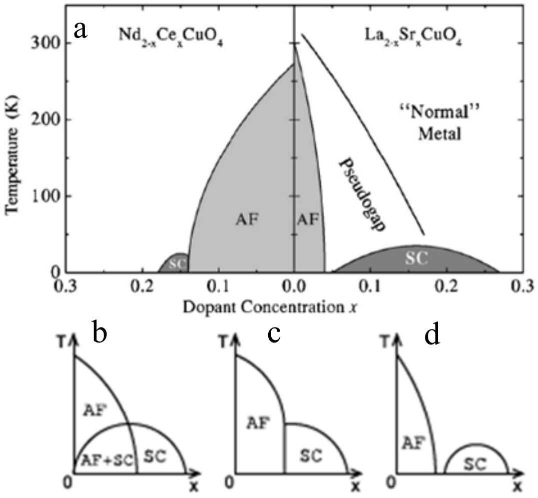

Figure 3.1: (a) Schematic phase diagram of high-Tc superconductors showing hole doping (right side) and electron doping (left side), from ref [7] (b), (c) Possible phase diagrams of the cuprates in the clean limit. C is the phase diagram of chemically doped LSCO, from ref [8].

In Figure 3.2(b) and (c) we can see the Nd_2CuO_4(T’) structure with square planar CuO_4 and K_2NiF_4(T) structure with octahedral CuO_6 coordination. Electron doped superconductors have the T’ structure while hole doped superconductors have the T structure. As we can see in Figure 3.1(a), on the hole-doping side the antiferromagnetic order is rapidly suppressed at 3–5 % hole concentration. Almost immediately after the suppression of the antiferromagnetic phase, superconductivity appears, ranging from x =6–25 %. The dome-shaped Tc is characteristic of all hole-doped cuprates, even though the maximum Tc varies from about 40 K in the $La_{2-x}Sr_xCuO_4$ (LSCO) family to 93 K and higher in other families such as $YBa_2Cu_3O_{6+y}$ (YBCO) and $Ba_2Sr_2CaCu_2O_{8+y}$ (Bi-2212). On the electron-doped side, the antiferromagnet is more robust and survives up to x=0.14, beyond which a region of superconductivity arises. [5].

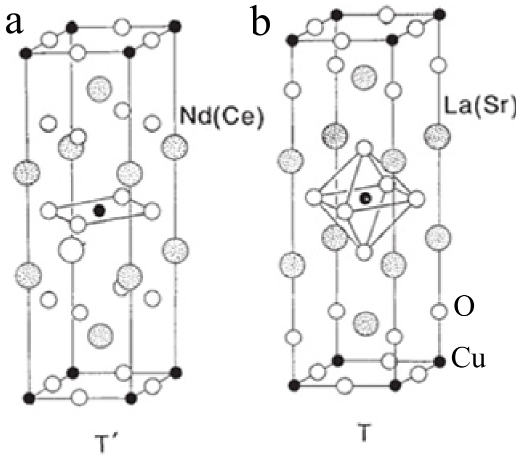

Figure 3.2. (a), (b) Nd_2CuO_4(T’) and K_2NiF_4(T) crystal structure.

The synthesis of high quality thin films of $(RE,Ce)_2CuO_4$ HTSC (RE=rare earth element) has probed to be challenging. Nevertheless recent reports claim that it is possible to obtain superconductivity in thin films of RE_2CuO_4 (RE=Pr, Nd, Sm), the parent compounds of the electron doped HTSC [9], without chemical doping. The authors of that work claim that complete removal of apical oxygen allows for superconductivity to appear in undoped samples. Nevertheless it is also possible that in the process of removing apical oxygen, the samples become electron doped by removal of the oxygen of the CuO_2 planes. This also brings up the important question of the role played by quenched disorder, which is implied by the chemical doping, in the phase diagram of cuprates. If the superconducting (SC) state is ever realized in clean interfaces, the phase diagram of cuprates in the absence of quenched disorder can be studied. Phenomenological calculations [8] suggest that antiferromagnetic (AF) and SC phases should be separated by either a region of local coexistence or a first order transition (Figure 3.1 (b)). A glassy state, as in the widely studied phase diagram of LSCO, was reproduced only incorporating quenched disorder. The generation of superconductivity at interfaces may reveal the true phase diagram of clean cuprates.

Encouraging to this objective is the fact that charge transfer in complex oxides interfaces was recently observed [1, 3] even at interfaces with hole doped HTSC [10, 11]. Moreover, doping with holes of La_2CuO_4, the parent compound of p-type HTSC, has yielded a record Tc=50K for the $La_{1-x}Sr_xCuO_4$ family [12]. Electron doping of a complex oxides yielding superconductivity was demonstrated in the $LaAlO_3/SrTiO_3$ interface, although the Tc was only 0.4K [13]. The realization of n type HTSC at heterointerfaces is still an open problem.

In this Chapter we will demonstrate that starting from SCO the Mott insulating parent compound of n-type HTSC it is possible to obtain a doped n-type material at the interface formed with LFO through charge transfer. Moreover we will show that the formed heterostructures, which are composed of two insulating materials, show metallic behavior in the temperature range 180-300K, however the superconducting state could not be achieved.

1.1 Choosing the right materials

The materials used in heterostructures will have in general different work functions creating a non-equilibrium situation. As a consequence charge will be transferred between these two materials to create an electrostatic potential that compensates this difference in work functions [4]. Thus if we want to transfer electrons to the cuprate we will have to choose a material which Fermi level remains above that of the first empty states of the undoped cuprate. In Figure 3.3 we observe the schematic band diagrams of La_2CuO_4(LCO), SCO, $SrTi_{1-x}Nb_xO_3$(Nb_x-STO), $YBa_2Cu_3O_y$(YBCO), and LSMO[4]. This schematic phase diagram is consistent with the experimental realization of charge transfer to cuprates observed in LCMO/YBCO [10] and $Nb_{0.01}$-STO/SCO [14] interfaces. In both cases the chemical potential of the cuprate is below the one corresponding to LCMO (this one is similar to the chemical potential of LSMO) and $Nb_{0.01}$-STO respectively.

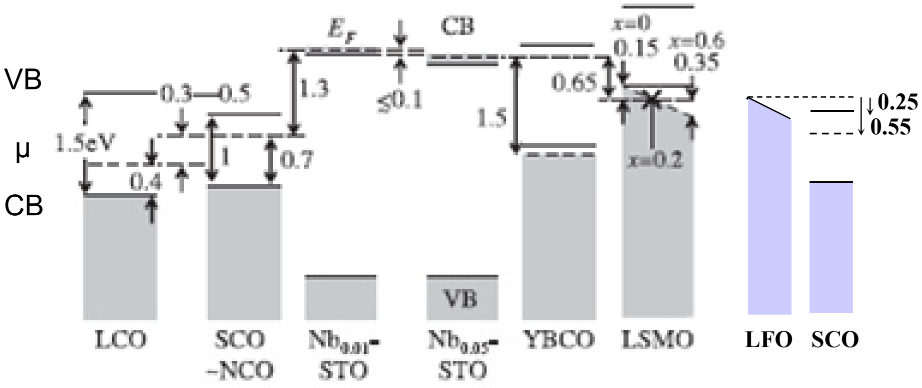

Figure 3.3: Schematic band diagrams of LCO, SCO, NCO, $Nb_{0,01}$-STO, $Nb_{0,05}$STO, YBCO and LFO were valence band (VB), conduction band (CB) and chemical potential (μ) is shown. Adapted from ref [4].

We have chosen LFO as the electron donor material and SCO as the cuprate that we want to dope. Using the measurements of the Fermi level of ref [15] we can add to the schematic [4] of Figure 3.3 the band structure of LFO. In the resulting band diagrams we observe that the chemical potential of LFO is 0.55eV above the chemical potential and 0.25eV above the conduction band of SCO. Consequently LFO is a good candidate to transfer electrons to the SCO. But also LFO has two important advantages: it is an antiferromagnetic material and if doped with holes up to x<0.7 it remains insulating at low temperatures. Being AF is important because the transfer of spin-polarized electrons is detrimental to SC. The fact that LFO is insulating, even if hole doped, is important because any metallic behavior observed would be originated at SCO.

1.1.1 $LaFeO_3$

$LaFeO_3$ (x=0 in $La_{1-x}Sr_xFeO_3$) is a charge-transfer type insulator with a charge gap of about 2 eV due to the strong on-site coulomb repulsion [16]. The valence of the Fe ion, or the nominal hole doping level, in this system can be varied from +3 ($3d^5$, x=0) to +4 ($3d^4$, x=1) by substitution of trivalent La ions with divalent Sr ions. The hole doping greatly reduces the value of resistivity, although the compound remains insulating at low temperatures, at least up to x=0.7. One of the origins of the insulating ground state of the moderately hole-doped compound is the charge order, which shows up most conspicuously around x=2/3 in $La_{1-x}Sr_xFeO_3$. The orthoferrite LFO has orthorhombic Pbnm structure and lattice parameters a=0.555, b=0.556 and c=0.787 nm. The antiferromagnetic axis of LFO is parallel to **a** as shown in Figure 3.4 (a) [17]. When LFO is grown on STO (001) substrates it grows with the c axis oriented parallel to the substrate. The epitaxial relationship between the film and the substrate can be expressed as follows: (110) LFO // (001) STO and [001] LFO // [100] STO. Crystallographic twins given by the 90º rotation of the c-axis around the substrate surface normal that corresponds to the [110] axis of LFO[18] are found in epitaxial LFO. (Figure 3.4).

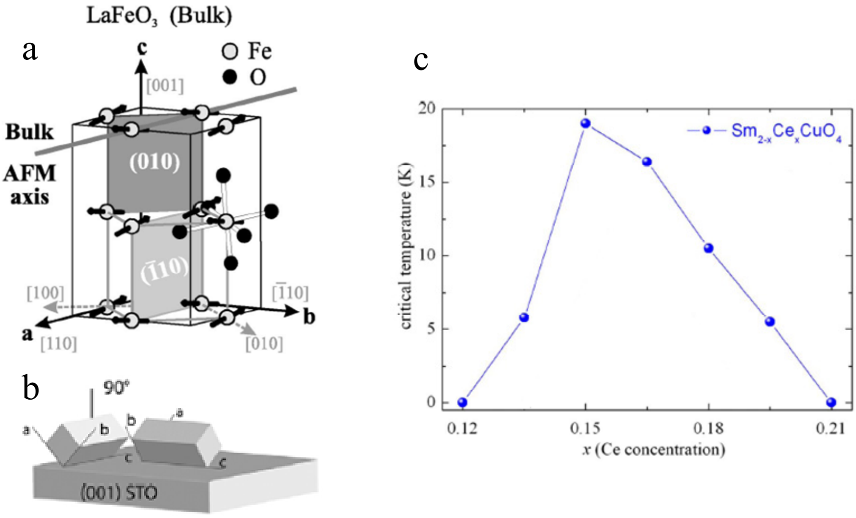

Figure 3.4: (a) Orthorhombic unit cell of $LaFeO_3$. The AFM axis is oriented along the crystallographic a axis. The cubic notation refers to the quasicubic sublattice [18] . (b) Schematic drawing of the twin configuration on (001) STO, the c-axis always lies on the substrate surface [19]. (c) Superconductivity phase diagram of $Sm_{2-x}Ce_xCuO_4$.

1.1.2 Sm_2CuO_4

The $Sm_{1-x}Ce_xCuO_4$ is an electron doped HTSC family that presents superconductivity for the doping range $0.12<x<0.21$ [20] with maximum Tc=20K for x=0.15 when grown in thin films (Figure 3.4(c)). The parent compound SCO is a Mott insulator that presents antiferromagnetism with a Neel temperature of 280K [21]. The SCO has T' structure with lattice constants a=0.3914 nm and c=1.1972 nm [22].

2 Sample Growth and Structural Characterization

The structural properties of thin films influence their physical properties. It is important to control and determine the defect structure, crystallinity and specially important the surface morphology if the final goal it is to grow superlattices and analyze interface properties. In the following we show the structural characterization and the optimization of the growth conditions for thin films of SCO and LFO. All the samples were grown on STO substrates with (001) orientation. This substrate has a close lattice matching (a_{STO}=0.391 nm) with LFO and SCO. The substrate imposes a compressive strain of 0.5% in the case of LFO and 0.1% in the case of SCO.

All the samples in this study have been grown by RF sputtering. The pressure during deposition of the thin films and heterostructures was fixed at 2.8 mbar of pure oxygen. After deposition the temperature is fixed at 750ºC and the growth chamber is filled with pure oxygen up to a pressure of 900 mbar. After an annealing step of 10 minutes the sample is cooled down at a rate of 20K/min to room temperature. The optimization of thin film growth was achieved by changing the deposition temperature.

2.1 Sm_2CuO_4 thin films

2.1.1 X-ray diffraction

We have used x-ray diffraction to determine the crystalline structure of SCO and to confirm the c-axis oriented growth of the thin films. In the case of SCO the growth temperature was found to be the most relevant parameter in determining its structural properties. We have grown SCO thin films varying the deposition temperature from 650ºC to 900 ºC.). In Figure 3.5 we show x ray reflectivity and diffraction spectra for the samples of Table 3.1. The thickness of the thin films is calculated from the finite size oscillations in the reflectivity spectra (Figure 3.5(a)). As we can see in the diffraction spectra all the films present a Bragg peak located at 2θ=29.8º, this peak corresponds to the (004) peak of the T' structure. Thus all the thin films have T' structure and preferential growth in the (001) direction. The presence of the peak at 2θ=29.8º allows us to calculate the c lattice parameter c=1.196 and confirms the T' structure. If the T structure were present or if a mixed T and T' film is obtained, the Bragg peak associated to this T structure would be found. Once we have confirmed the T' structure in our films, we have to concentrate in the optimization of the epitaxial and crystalline properties of the SCO thin film. Ideally we should detect only [001] diffraction peaks in the XRD spectra. As we can see in Figure 3.5(b) in thin films grown at 900ºC the identification of a peak at 2θ=32.8º denounces the presence of domains with (103) orientation. Lowering the deposition temperature to 800ºC allows for the growth of highly textured films with no misoriented domains. Moreover, the observed diffractograms for the sample grown at 800 ºC clearly exhibits finite size oscillations around the 004 Bragg peak, reflecting the smoothness of the surface. Although the growth of thin films at lower temperatures is detrimental for the crystalline properties of the films as can be deduced from the broad (004) peak in the thin film grown at 650ºC; it is still possible to grow the thin film at 650ºC and anneal the sample at 800ºC to recover the cristalinity (green spectrum in Figure 3.5(b)). We identified two optimum conditions to grow SCO: deposition at 800ºC, or deposition at 650ºC and a recrystallization step at 800ºC during 1 hour after growth.

Sample	Thickness		D. Temp.	Annealing
SCO – Thin film	9.6 nm	8 u.c.	900ºC	
SCO – Thin film	8.4 nm	7 u.c.	800ºC	
SCO – Thin film	18 nm	15 u.c.	650ºC	800ºC - 1 hour
SCO – Thin film	14.4 nm	12 u.c.	650ºC	

Table 3.1. SCO thin film sample summary and growth conditions

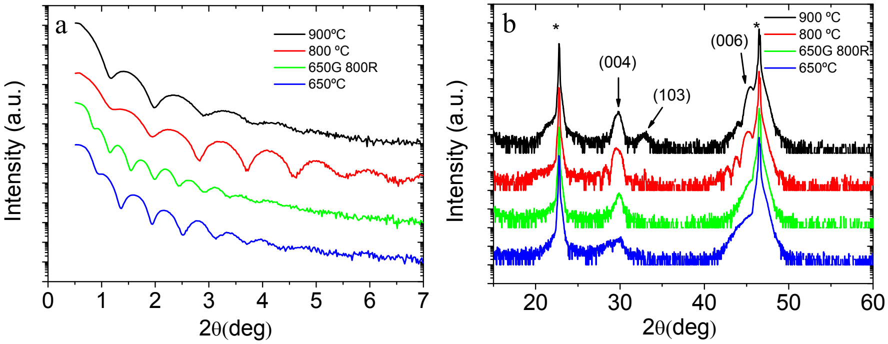

Figure 3.5: (a), (b) X-ray reflectivity and diffraction spectra of SCO thin films grown at different temperatures. (see Table 3.1).

2.1.2 AFM characterization

Using AFM we have analyzed the impact of growth temperature on the surface morphology of the films. It is known that one of the difficulties of the growth of HTSC thin films is that during thin film growth CuO islands and precipitates are formed. In our case it is essential to avoid this defects to obtain high quality interfaces. In Figure 3.6 we show surface morphology for thin films grown at different temperatures. In the film grown at 800ºC (Figure 3.6(a)) the surface morphology observed presents islands and precipitates with RMS roughness of 1.2 nm. Because we know from x-ray measurements that the film is highly (001) textured we conclude that high temperature growth yields SCO thin films with oriented and crystalline islands. On the contrary, the film grown at 600ºC (Figure 3.6(b)) has a smooth surface, but the crystalline quality is very poor. The conditions that produced the best results are the deposition of the film at 650ºC with an annealing step after the thin film is grown. This procedure gives a smooth surface with RMS roughness of 0.38nm (Figure 3.6(c)).

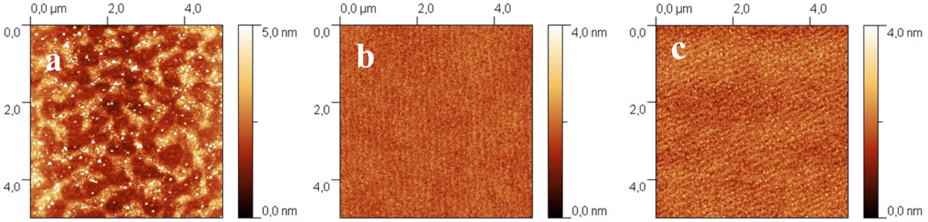

Figure 3.6: Atomic force microscopy topographic images of SCO thin films grown at: 800ºC (a), 650ºC (b) and (c). Sample shown in (c) has been annealed 1 hour at 800ºC after growth.

2.1.3 Summary

Using x-ray diffraction and AFM surface morphology experiments we have analyzed the effect of growth temperature on SCO thin films. While thin films deposited at 800ºC are highly textured in the (001) direction and have better cristallinity than films deposited at 650 ºC, the latter have a fairly smoother surface as proven by AFM. Consequently optimal growth conditions are the following; deposition at 650ºC and the recrystallization of the thin film at 800ºC during 1 hour.

2.2 $LaFeO_3$

2.2.1 X-rays

We have grown LFO thin films varying the deposition temperature from 700ºC to 900 ºC. In Figure 3.7 we show reflectivity and diffraction spectra for thin films grown at: 900, 800, and 700ºC. Because the lattice parameters of the LFO and STO are very close, it is difficult to observe the Bragg peaks of the LFO along de (00l) directions. Nevertheless the fact that we do not observe any other Bragg reflections probes that the there are no domains in the sample with and orientation different than (001). Although is not possible to observe the (001) diffraction peaks, the finite size fringes around these are clearly visible (Figure 3.7(b)), these fact implies that the (001) reflections are present below the substrate peaks. The fact that finite size oscillations in both x-ray reflectivity and diffraction are clearly visible for films grown at temperatures of: 900ºC, 800ºC and 700ºC implies that all of them are of high structural quality and have low roughness.

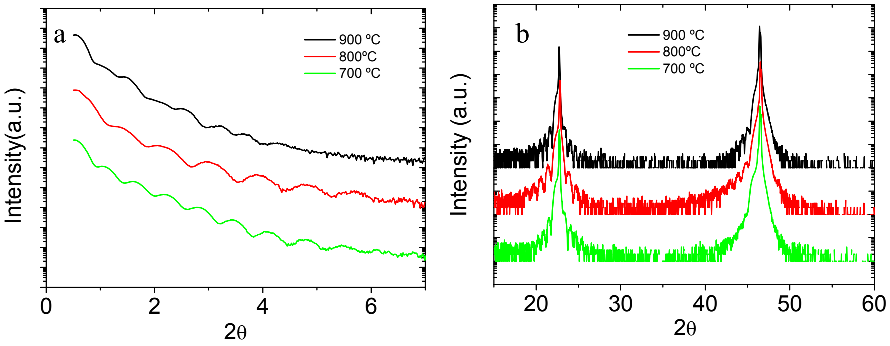

Figure 3.7: (a) and (b) X-ray reflectivity and diffraction spectra of LFO thin films grown at different temperatures: 900 (black), 800 (red) and 700ºC (green)

2.2.2 AFM characterization

Surface topography images obtained by AFM of LFO thin films deposited at 800ºC and 900ºC are shown in Figure 3.8 (a) and (b) respectively. The RMS roughness of both thin films is less than 1 u.c.. The step and terrace structure observed in both cases is imposed by the substrates. The fact that the terraces in the AFM image obtained at 800ºC are wider is a consequence of the lower miscut angle of the STO substrate.

2.2.3 Summary

In the temperature range studied there is no appreciable difference in the structural properties of LFO thin films. As a consequence it is possible to choose the LFO temperature growth in the range of 700-900ºC depending on the material that we want to combine it with.

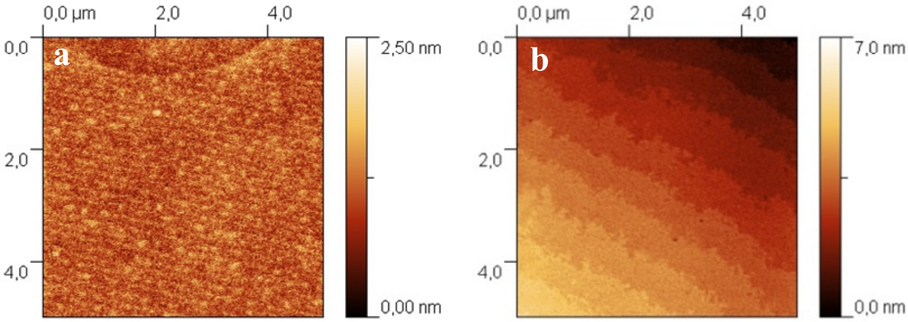

Figure 3.8: Atomic force microscopy topographic images of SCO thin films grown at: 800ºC (a), 900ºC (b).

2.3 $LaFeO_3/Sm_2CuO_4$ Heterostructures

We have grown $[LFO_{14}/SCO_N]_6$ superlattices consisting in six repetitions of a bilayer formed by 14 u.c. of LFO and N u.c. of SCO on STO (001) substrates, N was varied between 1 and 3 u.c.. We deposited the LFO films at 800ºC and the SCO films at 650ºC. The growth temperatures were chosen following the optimum conditions for deposition of thin films. Oxygen pressure during growth was P_{O2}=2.8 mbar, after the deposition samples were annealed during 10 min at 750ºC under an oxygen pressure of 900 mbar before cooling down at a rate of 20 ºC/min.

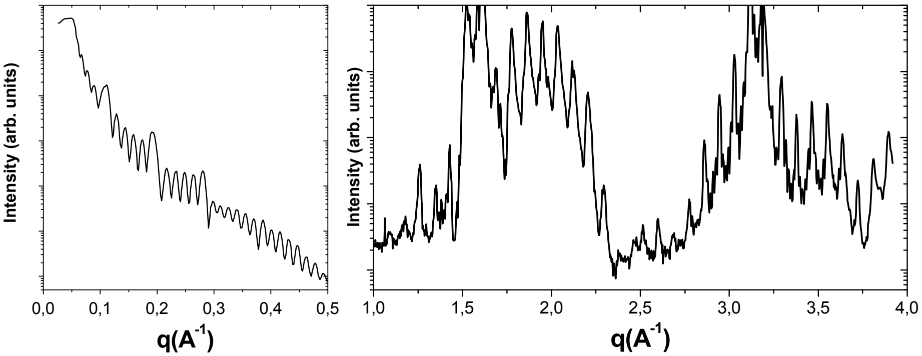

Figure 3.9: (a), (b) X-ray reflectivity and diffraction spectra of a $[LFO_{14}/SCO_{1}]_{6}$ superlattice measured with x-ray radiation of wavelength λ=0.08186 nm at BM25 (ESRF).

2.3.1 X-rays

Structural characterization using x-ray radiation of wavelength λ=0.08186 nm was done at BM25 (Spline) of the European Synchrotron Radiation Facility (ESRF). Figure 3.9(a) and (b) show x ray reflectivity and diffraction spectra respectively for a superlattice $[LFO_{14}/SCO_{1}]_{6}$. In the reflectivity spectrum clear superlattice peaks and finite size oscillations are observed. In the diffraction spectrum many narrow superlattice peaks are observed proving the high quality and low roughness of the interfaces between LFO and SCO. Because the SCO thickness in this superlattice is only 1 u.c. the broadening of the (004) Bragg peak as well as the overlapping superlattice Bragg peaks makes impossible to locate its position accurately enough to calculate the lattice parameters. Nevertheless, its presence confirms the T’ structure of the cuprate. To further investigate the structural characteristics of our heterostructures we measured X-ray reciprocal space maps. For simplicity we label points in the reciprocal space $Q=(q_x,q_y,q_z)$ with coordinates $(H,K,L)=(\ q_x\ a/2\pi,\ q_y\ a/2\pi,\ q_z\ a/2\pi)$ in reciprocal lattice units where a is the lattice parameter of the STO substrate. Because STO is cubic and the LFO is tetragonally distorted with almost the same lattice parameters of the STO, if we study the reciprocal space near the points where H,K, and L are integer numbers the signal coming from the substrate will not allow us to study the signal coming from LFO. Nevertheless because LFO is tetragonally distorted

[18] we are able to study (H,K,L) points in the reciprocal space with semi-integer values of H,K and L where no intensity from the substrate is detected. Following this strategy we measured reciprocal space maps around the point (0.5 0.5 1.5). In Figure 3.10(a) we can clearly observe two distinctive features: the maximum intensity region is located at (0.5 0.5 1.479) and the intensity profile is elongated along the L direction corresponding to the small thickness (5.4 nm) of the LFO layer, moreover superlattice peaks are clearly visible. Figure 3.10(b) shows the reciprocal space map associated with in plane lattice parameters, the fact that the maximum intensity is located at H=K=0.5 proves that the LFO is growing with the same lattice parameters of the STO substrate. Together with the information provided in Figure 3.10(a) we can calculate the lattice parameters of the LFO being a=(0.391+/-0.001)nm and c = (0.396+/-0.001) corresponding to a shortening of the in plane lattice parameters to match those of the substrate. To obtain lattice parameters of the SCO we studied the reciprocal space point (0 1 2.2) (Figure 3.10(c)). In this case the SCO has a bulk lattice parameter along the c axis of 1.197 nm as a consequence the points in the reciprocal space have different periodicity than the substrate. However, in the studied samples, the fact that the SCO is only 1 or 2 u.c. and the superlattice peaks are superimposed to this peak makes impossible to obtain the L coordinate of the maximum intensity, in fact this superlattice peaks are the same that can be observed in Figure 3.9(b). We can work out the in plane lattice parameters of the SCO from fFigure 3.10(d) obtaining a=b=(0.391+/-0.001) nm. Thus both LFO and SCO are fully strained and have the lattice parameters of the STO in the plane of the substrate.

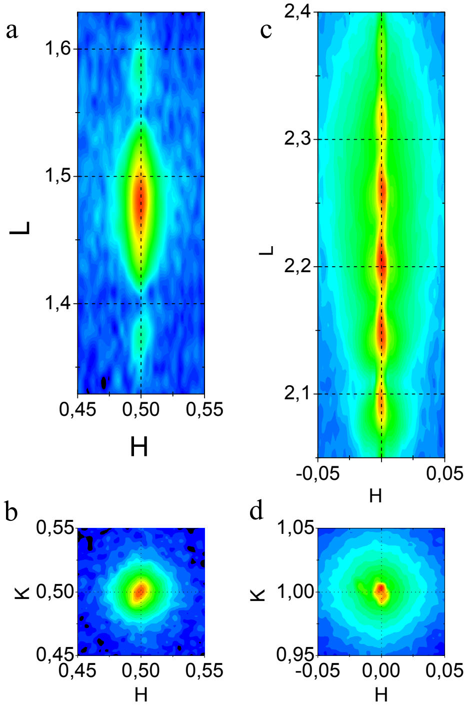

Figure 3.10: Reciprocal space of a ([$LFO_{14}/SCO_1]_6$ superlattice measured with x-ray radiation of wavelength λ=0.08186 nm at BM25 (ESRF). The reciprocal lattice units are referred to the cubic unit cell of STO.

2.3.2 AFM Characterization

In Figure 3.11 we show the topography of $[LFO_{14}/SCO_1]_6$ superlattice. The surface RMS roughness is 0.39 nm and the surface is free from precipitates.

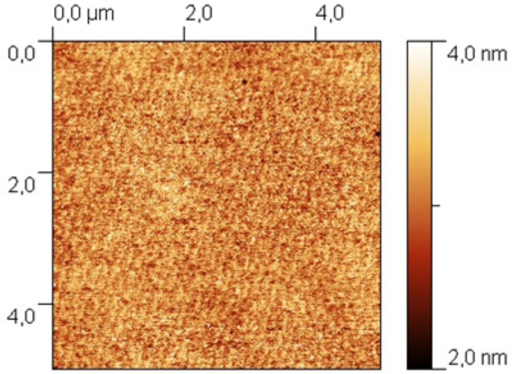

Figure 3.11: Atomic force microscopy topographic image of a (LFO 14 u.c. and SCO 1 u.c.)$_{x6}$ superlattice.

2.3.3 Structural characterization - STEM

Figure 3.12 displays high magnification Z-contrast image of a [LFO$_{14}$/SCO$_{1}$]$_{6}$ superlattice. In the ADF image (Figure 3.12(b)) perfect epitaxial properties are observed in the growth of LFO on the STO substrate as well as on the first interface of SCO on LFO. Nevertheless interfacial disorder appears in the form of steps when LFO is grown on top of SCO. Although is not clearly visible in the ADF image, the bright field image (Figure 3.11(a)) of the same zone clearly shows domains of LFO with different orientations. As discussed in the introduction orthorhombic LFO grows on (001) STO with twins due to the 90º rotation of the c-axis around the substrate surface normal. When successive LFO/SCO bilayers are deposited, disorder accumulates causing the interfaces near the top of the sample to be rougher.

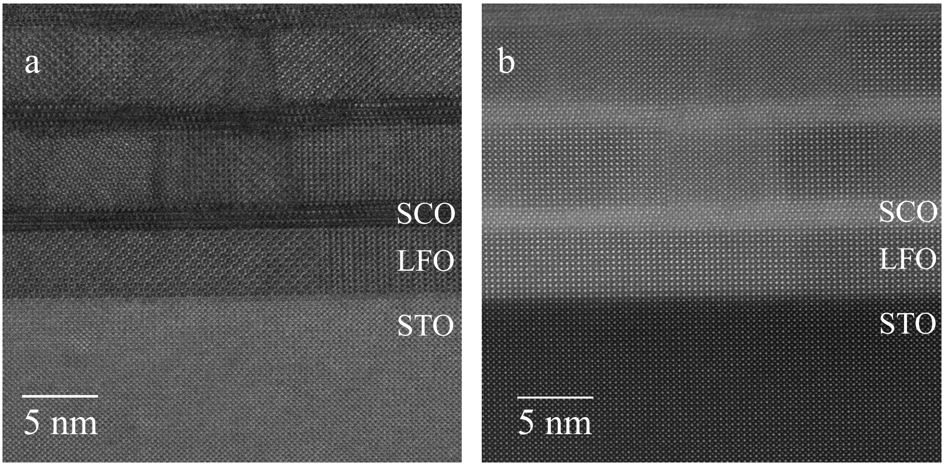

Figure 3.12: (a) Bright field and (b) annular dark field image of a (LFO 14 u.c. and SCO 2 u.c.)$_{x6}$ superlattice.

Figure 3.13 show an ADF image of [LFO$_{14}$/SCO$_3$]$_6$superlattice. Two dimensional elemental maps corresponding to La M$_{4,5}$ Fe L$_{2,3}$, Sm M$_{4,5}$ and O K edge are shown in Figure 3.13 (d-g) respectively, this maps correspond to the area marked as spectrum image in panel (a). The 2D elemental map obtained combining colored individual maps show that there is no interdiffussion at the SCO/LFO interface. The Sm elemental map (Figure 3.13(f)) show pairs of Sm planes and between them a darker area where the CuO$_2$ planes are located. The composed elemental map clearly shows the presence of a LaO plane, and the absence of Fe, at the interface with SCO. This is clear in Figure 3.13(c) were the interface is blue (Sm) and red (La). Because no individual Sm planes are observed at the SCO near the interface, we conclude that the interfacial structure consist of a sequence of LaO, CuO$_2$ and Sm planes. In panel (b) we have signaled the individual atomic planes with color bars (green=Fe, red=La, blue=Sm, yellow = Cu) according to the observed elemental maps.

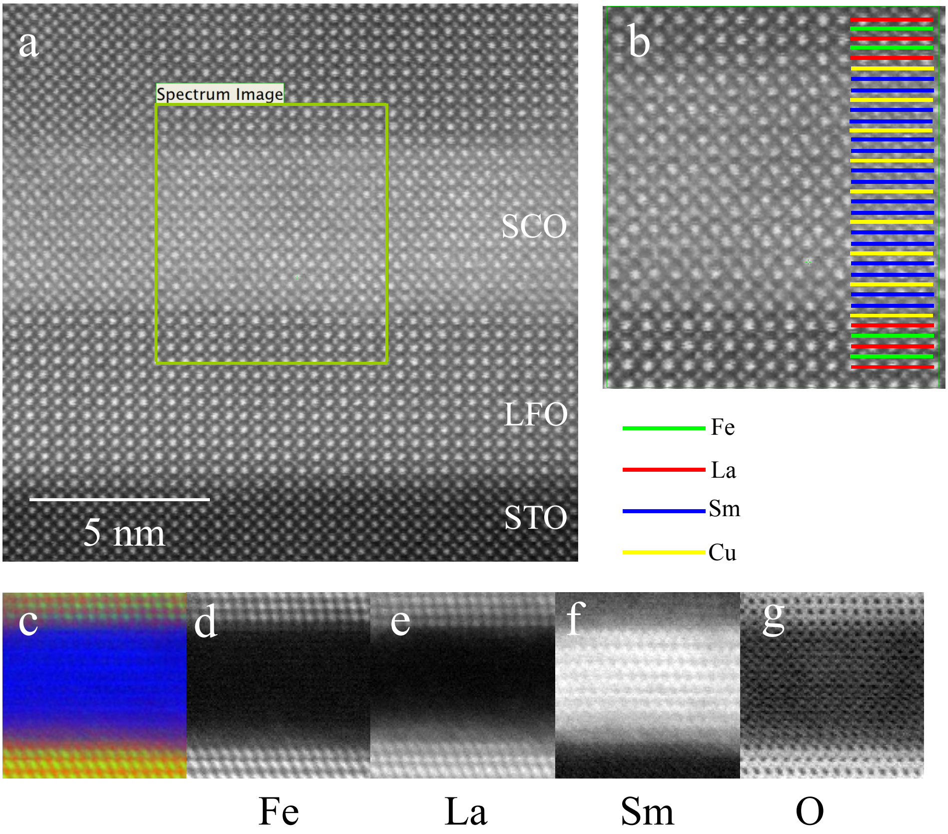

Figure 3.13: (a) High magnification ADF image of a $[LFO_{14}/SCO_3]_6$superlattice. (b) ADF image with atomic planes indicated with color bars. (c) Combined atomic elemental map, using the indicated color codes. (d-g) Atomic elemental maps obtained from Fe L $_{2,3}$, La M$_{4,5}$, Sm M$_{4,5}$, and O K edge.

3 Spectroscopy

In stoichiometric SCO the oxidation state of Cu is 2+. If electron transfer occurs then the oxidation state of Cu should change from Cu^{2+} to a mixed Cu^{2+}/Cu^{1+} state and this should be detected in spectroscopy experiments. We have performed X-ray absorption (XAS) and electron energy loss spectroscopy (EELS) experiments to study this effect. Although both techniques are element selective, there are important practical differences. The XAS is a synchrotron based technique; the great advantage is the intensity of the signal obtained. However, it is a non local technique in the sense that the incident photons penetrates ~ 5nm in the sample, consequently a thick layer is probed at the same time. STEM-EELS allows us to obtain the spectra with atomic resolution but the intensity of the obtained signal is small. It is possible to study the EELS spectra of some transition metals like Mn but it is extremely difficult to study the Cu spectrum because of the poor signal obtained. However because in cuprates the Cu atoms are coordinated with oxygen atoms and the oxygen spectrum depends on the oxidation state of the Cu, we will be able to study the oxidation state of Cu by looking in the absorption K edge of O atoms.

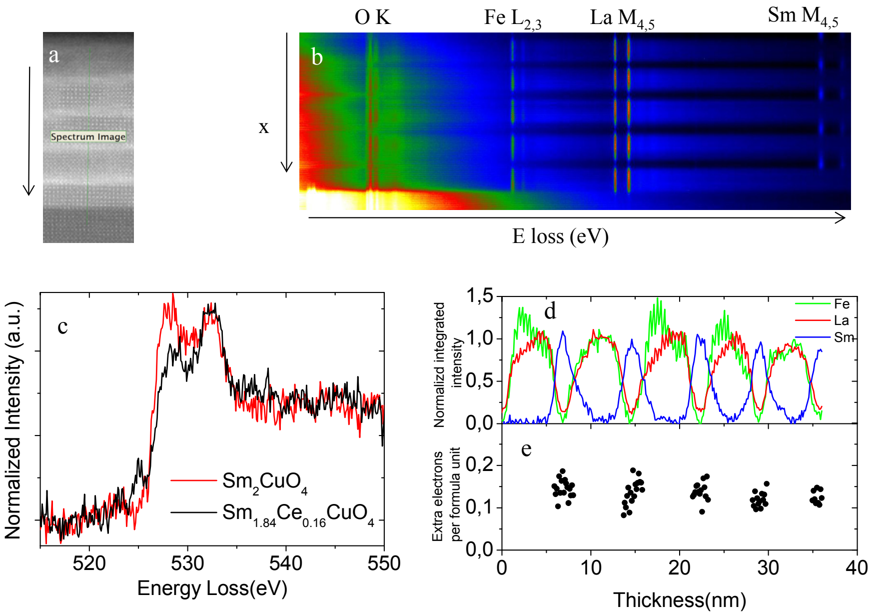

Figure 3.14: (a) ADF image of a [LFO$_{14}$/SCO$_3$]$_6$ superlattice. (b) EELS spectrum taken along the spectrum image marked in (a). (c) EELS spectra of reference SCO (red) and SCeO (black) samples. (d) Normalized integrated intensity for the Fe L $_{2,3}$ (green), La M $_{4,5}$ (red), and Sm M $_{4,5}$ (blue). (d) Extra electrons in the SCO layers obtained through MLLS fit to reference spectra.

3.1 EELS

In Figure 3.14(a) show and ADF image of a $[LFO_{14}/SCO_3]_6$ superlattice with the line scan marked in green. For each point in this line scan a complete energy loss spectrum is taken, this is shown in Figure 3.14(b). In this figure the superlattice structure is clearly identified with alternating regions where Sm is present and others where La and Fe are observed (the intensity of the Cu $L_{2,3}$ edge is too low to seen in this plot). Figure 3.14(d) shows elemental maps of Fe, La, and Sm obtained from this spectrum across the line shown in Figure 3.14(a). To obtain information on the oxidation state of Cu we have to study the O K edge and compare it to the EELS reference spectra corresponding to $Sm_{1.84}Ce_{0.16}CuO_4$ (SCeCO) and SCO, both shown in Figure 3.14(c). In the case of SCO the spectrum corresponds to 0 extra electrons per copper atom and in the case of SCeCO the spectrum corresponds to 0.16 extra electrons per copper atom. To study quantitatively how many extra electrons are in our superlattices we performed a multiple linear least square (MLLS) fit of the O K edge in the superlattice to the reference spectrum. The coefficients in the MLLS fit verify that $SCO_{superlattice}= C_N(SCO)+C_S(SCeO)$ and $C_N+ C_S=1$, where $SCO_{superlattice}$ is the spectrum of SCO obtained in the superlattice, SCO and SCeO are the reference spectra. With this approach we have a quantitavie measure of how similar the O K edge spectrum in the superlattice is to the O K edge in SCeO. If this were completely the same it will be verified that Cs=1 and Cn=0. In fact multiplying C_S by 0.16 we obtain the extra electrons in the superlattice, this is shown in Figure 3.14(d), and is equivalent to say that Cu in the superlattice is in a mixed Cu^{1+}/Cu^{2+} oxidation state. The overall excess electrons are 0.13+/-0.03, this electron doping of the SCO implies that we are in the doping range where superconductivity should be observed at low temperature[20]. To further illustrate this point we show in Figure 3.15(a) the same procedure applied to the $(LFO\ 14\ u.c./SCO\ 3\ u.c.)_{x6}$, here we show the MLLS coefficients and the extra electrons in the SCO layers of the heterostructures, the mean value of extra electrons is 0.09+/-0.01. If the extra electrons in SCO were originated in the LFO layers, we should then be able to detect extra holes in the LFO. We obtained the mean Fe $L_{2,3}$ spectrum in LFO interfacial region and in the center of the LFO layer and compare it with the LFO reference spectrum. We observe that the small peak at 703.6 eV in the superlattice is slightly more intense than in reference spectrum, comparing this with XAS data from the literature [23] (Figure 3.15(c)), we can conclude that LFO is slightly doped with holes, although no difference is observed between interfacial region and the middle of the layer.

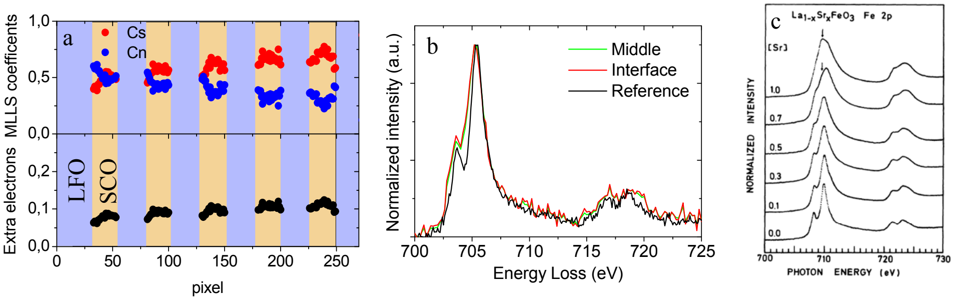

Figure 3.15: (a) MLLS coefficients and extra electrons in the SCO layers of a $[LFO_{14}/SCO_3]_6$. (b) Fe L $_{2,3}$ EELS spectra obtained from a reference $LaFeO_3$ sample (black), the averaged interface (red) and middle of layer (green) zone of LFO in the superlattice. (c) Fe L $_{2,3}$ XAS spectra of $La_{1-x}Sr_xFeO_3$ (from ref [23]).

3.2 XAS

X ray absorption experiments were performed at the beamline ID08 of the ESRF. In Figure 3.16(a) we observe the Cu $L_{2,3}$ absorption spectrum of a thin film 6 u.c. thick of SCO (red line) and a (LFO 14 u.c./SCO 1 u.c.)$_{x6}$ superlattice (black line). The two main peaks $L_3 \sim 932{,}8$ and $L_2 \sim 952{,}7$ eV observed in both spectra are associated with transitions in formally divalent copper states. More precisely, this transitions are from the Cu ground state $3d^9$ to the $\underline{2p}_{3/2,1/2}3d^{10}$ excited state, where $\underline{2p}_{3/2,1/2}$ denotes a $2p_{3/2}$ (L_3) or a $2p_{1/2}$ (L_2) hole [24]. The second common feature to both spectra is the broad peak at 938.4 eV, this is associated with a transition in Cu^{2+} to the excited state $2p_{3/2}3d^94s^1$ [25-27]. The main difference between both spectra is the presence of the 935.6 eV peak (see arrows in Figure 3.16) associated with the presence of Cu^{1+} [25-27].

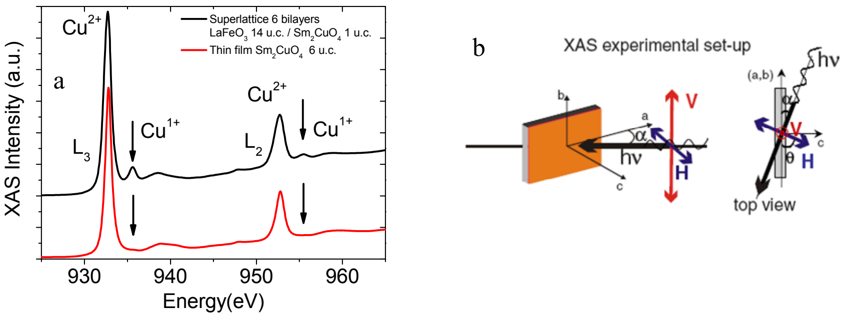

Figure 3.16: (a) XAS Cu L $_{2,3}$ spectra of a [LFO$_{14}$/SCO$_1$]$_6$ superlattice (red) and a SCO 6 u.c. thin film (red). The absorption peaks corresponding to Cu^{2+} and Cu $^{1+}$ are indicated by arrows. (b) Schematic of the XAS experimental setup when polarized vertical (V) or horizontal (H) light is used (from ref [28]).

Because cuprates are highly anisotropic materials we can gain more insight onto its electronic structure by performing the XAS experiments with polarized light. In Figure 3.16(b) we show schematics of the experimental setup to measure XAS spectra with photons with vertical (V) and horizontal (H) polarization. In the case of V-polarization the electric field is always parallel to the surface sample and consequently to the ab plane (CuO$_2$ planes). In the case of the H-polarization the electric field has a component perpendicular and another one parallel to the sample. Because the incidence angle of the photons is α=30º measured from the surface sample, in the case of H-polarization most of the E field intensity (cos^2(30)=0.75) will be parallel to **c** the surface normal.

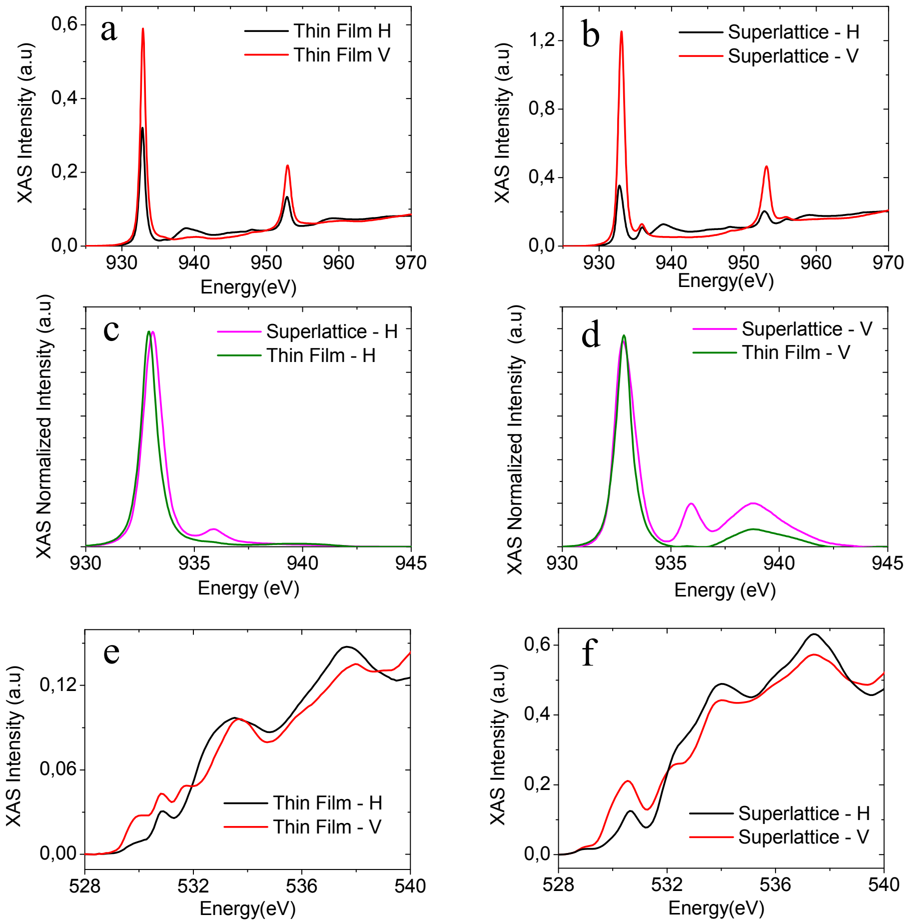

Figure 3.17 (a), (b) XAS Cu L $_{2,3}$ spectra of a SCO 6 u.c. thin film and $[LFO_{14}/SCO_1]_6$ superlattice respectively obtained with horizontal (black) and vertical (red) polarized light. (c), (d) The same spectra normalized to the L $_{2,3}$ edge jump obtained with horizontal and vertical polarized light respectively. (e), (f) XAS O K spectra of a SCO 6 u.c. thin film and $[LFO_{14}/SCO_1]_6$ superlattice respectively obtained with horizontal (black) and vertical (red) polarized light.

From the spectra in Figure 3.17 (a) and (b) we observe that in both cases the absorption for the $L_{2,3}$ edges is more pronounced for vertical polarization. This proved that the holes in the CuO_2 plane have mostly $3d_{x^2-y^2}$ character (see appendix A for an overview on d orbitals). Another interesting feature is that the transitions to excited states (E=938.4 eV) are only observed with H-polarization. Since out of plane Cu-d orbitals are fully occupied transitions to excited states are the possibility remaining when photons are polarized parallel to c. In Figure 3.17 (c) and (d) we show the L_3 absorption spectra normalized to the edge jump. The signature of Cu^{1+} is clearly visible for the superlattice with H and V polarized light. Nevertheless in the case of H polarization the associated peak is clearly more intense indicating the out of plane character of these states. These peaks are observed in the Cu 2p excitation spectra due to hybridization of the Cu^{1+} $3d3_{z^2-r^2}$ orbitals and apical O $2p_z$ orbitals [29, 30]. In the SCO there are no apical oxygens but in the case of the superlattice the Cu atoms in interfacial CuO_2 planes have apical oxygens, thus the intensity of this peak is a consequence of an orbital reconstruction at the interfacial plane. Finally in Figure 3.17 (g) and (h) we show the O-K edge XAS spectra. The analysis of the oxygen edge is extremely difficult because the observed signal is a combination of the oxygen signal coming from SCO, LFO and the STO substrate, consequently we will not perform here a further analysis. This illustrates the advantage of the STEM-EELS experiment where the analysis of the O K edge is possible because the spectra have spatial resolution.

3.3 - Discussion

The presence of an absorption peak associated to Cu^{1+} in the XAS spectra of the superlattice confirms the finding of the EELS experiment of the presence of extra electrons in the SCO in LFO-SCO heterostructures. It is worth to remark that the SCO thin film was grown at the same conditions than the superlattice so we can exclude an explanation of the extra electrons as being originated in, for example, an oxygen deficient sample. The presence of Cu^{1+} in the superlattice is clearly related to the existence of the interface with LFO and evidences the electron transfer from LFO to SCO. Furthermore we can conclude from the XAS experiments with polarized light that and orbital reconstruction evidenced by the hybridization of $3d_{3z2-r2}$ orbitals and apical O $2p_z$ orbitals exists at the SCO/LFO interface.

4 transport measurements

We have measured the transport properties of the aforementioned samples. The LFO and SCO resistance vs. temperature plots of Figure 3.18 clearly show that these materials are insulating (dR/dT<0) as expected, this is observed either in four-contacts configuration or in two-contacts configuration. Nevertheless SCO/LFO superlattices show metallic-like behavior (dR/dT>0) in the temperature range 300-150K. This metallic behavior is consistent with the reduced oxidation state in SCO as proved by EELS and XAS [20]. In all the measured superlattices it was impossible to measure the resistance in Van der Pauw configuration below 160 K because it was not possible to obtain a stable voltage reading. If measured in two terminals configuration, the samples display insulating behavior (dR/dT<0) in all the temperature range. This is caused by the large contact resistance. We interpret this as follows, while the charge transfer occurs at every interface of the superlattice, the structural quality of each SCO layer deteriorates with the number of bilayers grown. In this form the continuity of CuO_2 planes in the SCO layers close to the surface of the sample maybe broken. Consequently the only conducting SCO layers are those at the bottom of the samples. Because the contacts are made through evaporated Ag on top of the samples, the current has to go through a thick insulating layer before reaching the buried conducting SCO layer. This series resistance rapidly increases with temperature, making impossible to measure the resistance of the SCO buried layers at temperatures lower than 160K. Efforts have been made to contact the bottom conducting SCO layer through wire bonding but the resistance vs temperature measurements of wire-bonded samples were similar to the results obtained on samples with evaporated contacts.

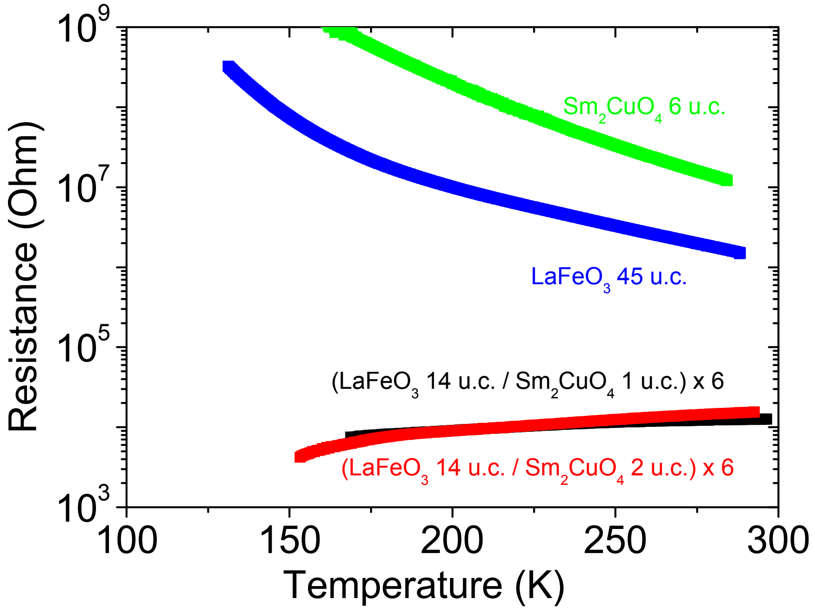

Figure 3.18 Resistance as a function of temperature of samples: $[LFO_{14}/SCO_1]_6$ (black) and $[LFO_{14}/SCO_2]_6$ (red), LFO 45 u.c. (blue) SCO 6 u.c. (green). Superlattices are measured in four contact (Van der Pauw) configuration, thin films are measured in 2 contact configuration.

It is known that the transport properties of cuprates depend strongly on the annealing conditions after the samples are grown. To obtain samples with superconducting properties is not only necessary to dope the samples with electrons but to remove excess apical oxygen and to repair Cu vacancies as recognized in the literature [31]. We believe that although we have achieved in our samples the electron doping level necessary to obtain superconductivity, further work is necessary to find the appropriate annealing process to remove excess apical oxygen with the final objective of obtaining superconductivity in these samples.

5 Conclusion and Perspectives

We have shown that we are able to grow superlattices of SCO/LFO with high quality interfaces. EELS measurements of the O-K edge have provided evidence for 0.13+/-0.03 electrons doping the SCO in LFO/SCO heterostructures. The case of transfer of electrons from LFO to SCO is further supported by the spectroscopic signature of Cu^{1+} is obtained in XAS measurements. This transfer of electrons from the LFO to the SCO is expected from the band alignment of the LFO and SCO. Moreover the transport measurements show metallic behavior ($dR/dT > 0$) in the LFO/SCO superlattices, consistent with the SCO being electron doped.

The electron doping of the parent compound of n-type HTSC realized in heterostructures is very encouraging to continue working in this direction. The fact that the metallic state was only measured in the 160-300K temperature should be the starting point to the optimization of the transport properties in this heterostructures. Since it is known that annealing conditions are critical to achieve superconductivity in electron doped cuprates, efforts should go in the direction of optimizing the annealing process of the samples to ensure that apical oxygen are completely removed. Another important direction should be working in the growth of bilayers and trilayers to find out the role played by each interface.

6 References

[1] A. Ohtomo, D. A. Muller, J. L. Grazul, and H. Y. Hwang, Nature (London) **419**, 378 (2002).

[2] S. Okamoto, and A. Millis, Nature (London) **428**, 630 (2004).

[3] J. Garcia-Barriocanal, F. Y. Bruno, A. Rivera-Calzada, Z. Sefrioui, N. M. Nemes, M. Garcia-Hernández, J. Rubio-Zuazo, G. R. Castro, M. Varela, S. J. Pennycook, C. Leon, and J. Santamaria, Adv. Mater. **22**, 627 (2010).

[4] S. Yunoki, A. Moreo, E. Dagotto, S. Okamoto, S. Kancharla, and A. Fujimori, Phys. Rev. B **76**, 64532 (2007).

[5] P. Lee, N. Nagaosa, and X. Wen, Rev. Mod. Phys. **78**, 17 (2006).

[6] N. P. Armitage, P. Fournier, and R. L. Greene, Rev. Mod. Phys. **82**, 2421 (2010).

[7] A. Damascelli, Z. Hussain, and Z.-X. Shen, Rev. Mod. Phys. **75**, 473 (2003).

[8] G. Alvarez, M. Mayr, A. Moreo, and E. Dagotto, Phys. Rev. B **71**, 014514 (2005).

[9] O. Matsumoto, A. Utsuki, A. Tsukada, H. Yamamoto, T. Manabe, and M. Naito, Phys. Rev. B **79**, 100508 (2009).

[10] M. Varela, A. Lupini, V. Pena, Z. Sefrioui, I. Arslan, N. Browning, J. Santamaria, and S. Pennycook, Arxiv preprint cond-mat/0508564 (2005).

[11] S. Smadici, J. Lee, S. Wang, P. Abbamonte, G. Logvenov, A. Gozar, C. Cavellin, and I. Bozovic, Phys. Rev. Lett. **102**, 107004 (2009).

[12] A. Gozar, G. Logvenov, L. F. Kourkoutis, A. Bollinger, L. Giannuzzi, D. Muller, and I. Bozovic, Nature **455**, 782 (2008).

[13] N. Reyren, S. Thiel, A. Caviglia, L. Kourkoutis, G. Hammerl, C. Richter, C. Schneider, T. Kopp, A. Ruetschi, and D. Jaccard, Science **317**, 1196 (2007).

[14] M. Nakamura, A. Sawa, H. Sato, H. Akoh, M. Kawasaki, and Y. Tokura, Phys. Rev. B **75**, 155103 (2007).

[15] A. Sawa, A. Yamamoto, H. Yamada, T. Fujii, M. Kawasaki, J. Matsuno, and Y. Tokura, Appl. Phys. Lett **90**, 252102 (2007).

[16] T. Arima, Y. Tokura, and J. B. Torrance, Phys. Rev. B **48**, 17006 (1993).

[17] R. White, J. Appl. Phys. **40**, 1061 (2009).

[18] J. Seo, E. Fullerton, F. Nolting, A. Scholl, J. Fompeyrine, and J. Locquet, J. Phys.: Condens. Matter **20**, 264014 (2008).

[19] J. Luning, F. Nolting, A. Scholl, H. Ohldag, J. W. Seo, J. Fompeyrine, J. P. Locquet, and J. Stohr, Phys. Rev. B **67**, 214433 (2003).

[20] Y. Krockenberger, J. Kurian, A. Winkler, A. Tsukada, M. Naito, and L. Alff, Phys. Rev. B **77**, 060505 (2008).

[21] I. Sumarlin, S. Skanthakumar, J. Lynn, J. Peng, Z. Li, W. Jiang, and R. Greene, Phys. Rev. Lett. **68**, 2228 (1992).

[22] T. Uzumaki, N. Kamehara, and K. Niwa, Jpn. J. Appl. Phys. Part 2 - Lett. **30**, L981 (1991).

[23] M. Abbate, F. M. F. de Groot, J. C. Fuggle, A. Fujimori, O. Strebel, F. Lopez, M. Domke, G. Kaindl, G. A. Sawatzky, M. Takano, Y. Takeda, H. Eisaki, and S. Uchida, Phys. Rev. B **46**, 4511 (1992).

[24] J. Fink, N. Nücker, E. Pellegrin, H. Romberg, M. Alexander, and M. Knupfer, J. Electron. Spectrosc. Relat. Phenom. **66**, 395 (1994).

[25] C. F. J. Flipse, G. van der Laan, A. L. Johnson, and K. Kadowaki, Phys. Rev. B **42**, 1997 (1990).

[26] M. Karppinen, M. Kotiranta, H. Yamauchi, P. Nachimuthu, R. S. Liu, and J. M. Chen, Phys. Rev. B **63**, 184507 (2001).

[27] Y. Tanaka, M. Karppinen, J. M. Chen, R. S. Liu, and H. Yamauchi, J. Solid State Chem. **182**, 1217 (2009).

[28] A. Tebano, C. Aruta, S. Sanna, P. G. Medaglia, G. Balestrino, A. A. Sidorenko, R. D. Renzi, G. Ghiringhelli, L. Braicovich, V. Bisogni, and N. B. Brookes, Phys. Rev. Lett. **100**, 137401 (2008).

[29] N. Nucker, E. Pellegrin, P. Schweiss, J. Fink, S. L. Molodtsov, C. T. Simmons, G. Kaindl, W. Frentrup, A. Erb, and G. Muller-Vogt, Phys. Rev. B **51**, 8529 (1995).

[30] P. Marksteiner, P. Blaha, and K. Schwarz, Zeitschrift für Physik B Condensed Matter **64**, 119 (1986).

[31] H. Kang, P. Dai, B. Campbell, P. Chupas, S. Rosenkranz, P. Lee, Q. Huang, S. Li, S. Komiya, and Y. Ando, Nature Mater. **6**, 224 (2007).

4

Electronic and Spin Reconstruction at the LSMO/STO Interface

Among correlated electron systems, $La_{0.7}Sr_{0.3}MnO_3$ (LSMO) has been extensively studied as a possible source of spin polarized electrons at room temperature [1]. The large values of tunneling magnetoresistance (TMR) reported for LSMO/$SrTiO_3$ (STO) /LSMO tunnel junctions at low temperature start to drop way below the Curie temperature of the magnetic electrodes, suggesting that a depolarization of the injected current may occur at the interface [2, 3]. This effect has been attributed to deteriorated magnetic properties of the manganite layer at the interface, a so called “dead layer”, whose origin is still not well understood [4-9]. Modified electronic and orbital structures at the interface [10, 11] could be at the origin of the dead layer problem. In this chapter we examine the possibility of manipulating the spin structure of the “dead layer” through the orbital reconstruction at the interface[12].

1 Introduction

The origin of novel electronic states at the interface has been discussed in terms of the combined effect of epitaxial strain and the electronic and orbital reconstruction resulting from symmetry breaking [13-15]. Since in these correlated oxides spin ordering is largely determined by the orbital structure through Goodenough-Kanamori rules [16, 17], the modified bonding at the interface determines its magnetic structure. This is the case for the ferromagnetic state reported to occur at the interface between non-ferromagnetic $LaFeO_3$ and $LaCrO_3$ [18] and is also at the origin of a ferromagnetic moment found in Cu at cuprate/manganite heterostructures [19, 20], in Fe at $BiFeO_3$/LSMO interfaces [21] and very recently at the interface between the Mott insulator $LaMnO_3$ and the band insulator STO [22]. In this chapter we show that manganite layers are magnetically coupled in LSMO/STO superlattices when the STO layer is thinner than 1 nm. This gives rise to very significant changes of magnetic and conducting properties. We have examined the electronic and magnetic structure of the LSMO/STO interface and found a magnetic moment induced at the Ti, resulting from the orbital reconstruction. This Ti moment is at the origin of the magnetic coupling between the LSMO layers. This finding constitutes direct evidence on how macroscopic properties of a heterostructure may be controlled by the interface orbital and spin reconstruction.

1.1 $La_{0.7}Sr_{0.3}MnO_3$

In the renaissance of the study of manganites during the 1990s, considerable emphasis was given to the analysis of $La_{1-x}Sr_xMnO_3$. Its Curie temperature as a function of doping level is above room temperature, increasing its chances for practical applications. The phase diagram and resistivity vs. temperature for this compound at several densities are shown in Figure 4.1 (a) and (b) respectively [23]. In this chapter we have used $La_{0.7}Sr_{0.3}MnO_{3.}$ With this doping level the bulk Curie temperature is $T_C = 369K$, the saturation magnetization is $M_S = 3.7\mu B/at_{Mn}$ and the low temperature resistivity is $\rho = 8 \times 10^{-5}\ \Omega$ cm. Another important property of LSMO is that it is a half-metallic ferromagnet as demonstrated by spin resolved photoemission experiments [1]. The half metallic character of LSMO means that the minority spin conduction band is empty, so the material has 100% spin polarization at low temperature. This property is also related to the saturation magnetization of LSMO at low temperatures as it matches well the spin only value expected form all 3d electrons present in manganese ions: $M_S = 0.7 \times Mn^{3+} (S=4/2) + 0.3 \times Mn^{4+} (S=3/2) = 0.7 \times 4\mu_B + 0.3 \times 3\mu_B = 3.7\ \mu_B$ [24].

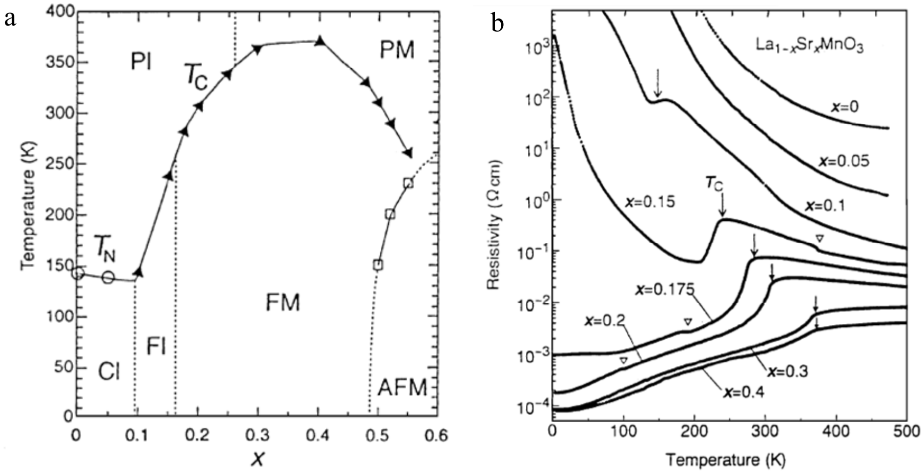

Figure 4.1. (a) Phase diagram of $La_{1-x}Sr_xMnO_3$ prepared with data from [23] and [25]. The AFM phase at large x is an A-type AF metal with uniform orbital order. PM, PI, FM, FI, and CI denote paramagnetic metal, paramagnetic insulator, FM metal, FM insulator, and spin-canted insulator states, respectively. T_C is the Curie temperature and T_N is the Neel temperature. (b) Temperature dependence of resistivity for various single crystals of $La_{1-x}Sr_xMnO_3$. Arrows indicate the Curie temperature. The open triangles indicate anomalies due to structural transitions. For more details see [23]. Adapted from ref [6].

A structural study of a LSMO crystal as a function of temperature shows it to be a rhombohedral perovskite above and below T_C with a=0.3876 nm and $\alpha = 90.46^{\circ}$ at room temperature [26]. When LSMO is grown as a thin film on a cubic substrate the unit cell is distorted and it adopts a pseudocubic structure. However upon distorting the unit cell, the ratio between the in-plane (a) and out-of-plane (c) lattice parameters becomes important for the magnetic properties of the manganite. In Figure 4.2 the effect of epitaxial strain (c/a ratio) on the orbital order and consequently on the magnetotransport properties of LSMO thin films of different compositions is shown. In these orbital phase diagram the F region (orbital-disordered) is ferromagnetic and metallic, the C ($3z^2$-r^2 ordered) and A region (x^2-y^2 ordered) are insulating[13, 27].

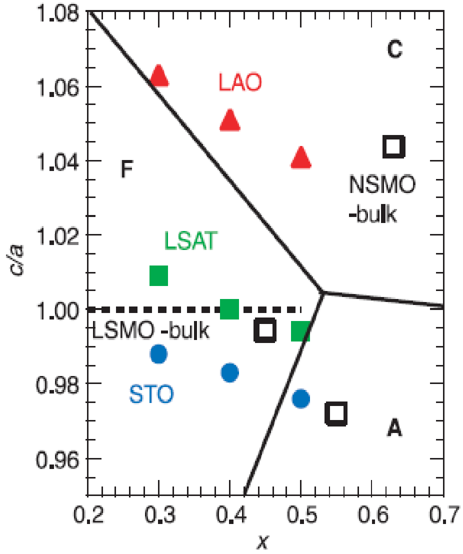

Figure 4.2. The schematic phase diagram in the plane of lattice strain c/a and doping level x. The data labeled LAO, LSAT, and STO represent the results for the coherently strained epitaxial thin films of $La_{1-x}Sr_xMnO_3$ grown on the perovskite single-crystal substrates of LaAlO3, (La, Sr)(Al, Ta)O_3, and $SrTiO_3$, respectively. LSMO-bulk and NSMO-bulk stand for the results for the bulk single crystals of $La_{1-x}Sr_xMnO_3$ and $Nd_{1-x}Sr_xMnO_3$, respectively. Adapted from [13].

Another relevant issue related to LSMO thin film growth is the existence of so-called “dead layer” or critical thickness that can be defined as the thinnest layer for which metallic as well as ferromagnetic behaviors are observed. In different studies this dead-layer thickness for thin films was estimated to be 3-4 nm depending on the substrate chosen. For thin films grown on STO the LSMO dead layer thickness is estimated to be 8 u.c. [28]. The mechanism behind the dead layer problem is still controversial. The phase-separation phenomenon at the LSMO/STO interface where ferromagnetic insulating and metallic phases separate at a scale of a few nanometers is one of the possible explanations [6]. Scanning tunneling spectroscopy [7] and ferromagnetic resonance [9, 29] supports this scenario. Another possible origin of the dead layer is the orbital reconstruction at the LSMO/STO interface. Strain induced distortion of the MnO_6 octahedra leads to crystal-field splitting of the e_g levels and lowers the $d_{3z^2-r^2}$ orbital over the $d_{x^2-y^2}$ orbital resulting in a local C-type antiferromagnetic structure at the interface [30].

1.2 $SrTiO_3$

Strontium titanate is probably the most frequently used substrate in the oxide community. It presents a cubic perovskite structure with lattice parameter a=0.3905 nm that is close to a variety of interesting oxides like LSMO. In pure form STO is a diamagnetic band insulator with a band gap of ~3.2 eV. However this material can easily be doped and turned into a semiconductor, a metal or even a superconductor [31]. The most usual ways to dope STO are [32]: Ti^{4+} substitution by Nb^{5+}, Sr^{2+} substitution by La^{3+} and oxygen reduction. Any of these three methods produces n-type doped STO.

2 Sample Growth and Structural Characterization

All samples in this study were grown by RF sputtering. The pressure during deposition of the thin films and heterostructures was fixed at 2.8 mbar of pure oxygen. The substrate temperature during deposition was 900ºC After deposition the temperature was fixed at 800ºC and the growth chamber filled with pure oxygen up to P=900 mbar. Following the annealing step of 60 minutes the sample is cooled down at a rate of 5K/min to room temperature. The temperature deposition and annealing times and temperature were chosen with two objectives: to obtain good structural properties and to obtain bulk-like Curie temperature and saturation magnetization. This is particularly difficult in manganites where a small amount of oxygen vacancies has a great impact on T_C and M_S.

The notation used in this chapter for superlattices is the following: $[LSMO_M/STO_N]_P$ denotes a superlattice of P repetitions of a bilayer with thickness M u.c. of LSMO and N u.c. STO.

2.1 X-ray diffraction

Selected samples were characterized using synchrotron radiation of wavelength λ=0.08186 nm at the beamline BM25B of the European Radiation Synchrotron Facility (Grenoble). The X-ray reflectivity and diffraction spectra of a $[LSMO_6/STO_2]_8$ and $[LSMO_8/STO_{10}]_8$ superlattice obtained at ESRF are shown in Figure 4.3. In view of the ultra thin STO layer thickness, the clear superlattice Bragg peaks displayed by both XRD and XRR spectra in $[LSMO_6/STO_2]_8$ sample indicate flat LSMO/STO interfaces. Superlattice Bragg peaks around the substrate (002) Bragg peak in the XRD spectra are clearly seen in both samples as well as finite size oscillations around each satellite. This provides evidence of coherent heteroepitaxial growth with sharp interfaces.

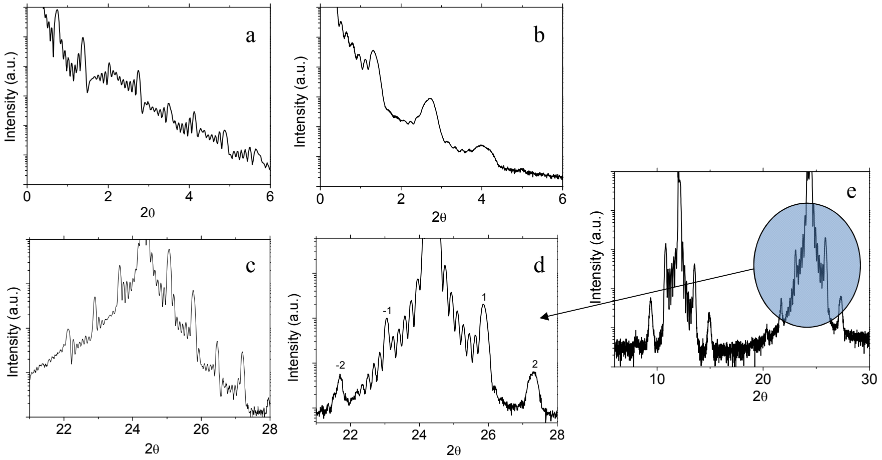

Figure 4.3. (a), (c) X-ray reflectivity and diffraction spectra of [$LSMO_8/STO_{10}]_8$ superlattice. (b), (d) X-ray reflectivity and diffraction spectra of [$LSMO_6/STO_2]_8$, (e) X- ray diffraction spectra of the same sample, the shaded area is zoomed in (d). All of the spectra are measured with λ=0.08186 nm at the beamline BM25B of the European Radiation Synchrotron Facility (Grenoble).

Because strain relaxation was found to have an important impact in the charge leakage process in other manganite/titanate heterostructures [33] we studied reciprocal space maps of the heterostructures to obtain the lattice parameters in plane and out of plane. Figure 4.4 show reciprocal maps around the (h k l)=(0.5 0.5 1.5) site of the same superlattice. The reciprocal space units are referred to the cubic lattice of the STO with lattice parameter a=0.3905 nm. This means that no STO should be observed in the reciprocal space point (0.5 0.5 1.5). Thus, the intensity observed in this point comes from the LSMO. LSMO has a perovskite structure with a rhombohedral distortion. In the pseudocubic description the lattice parameter is 0.3876 nm [34]. The lattice parameters of the LSMO extracted from the reciprocal space maps are $a_{LSMO}=b_{LSMO}=0.390\pm0.001$ nm in plane and $c_{LSMO}=0.386\pm0.001$ nm out of plane, showing that LSMO distorts into a tetragonal form when grown epitaxially on STO. All the superlattices showed tetragonal structure with in plane lattice parameters matching those of the STO substrate independently of the STO and LSMO layer thickness.

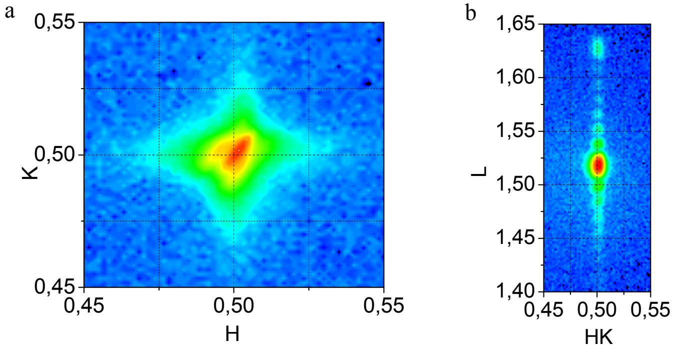

Figure 4.4. Reciprocal space maps of a of [$LSMO_6/STO_2]_8$ superlattice measured at the point (0.5 0.5 1.5). The reciprocal lattice units are referred to the cubic unit cell of STO.

2.2 Scanning transmission electron microscopy

Figure 4.5 (a) and (b) displays high and low magnification Z-contrast images of [$LSMO_6/STO_{18}]_8$ superlattice. The high magnification image shows high quality epitaxial interfaces free of defects. The low magnification image shows that layers are flat and continuous over long lateral distances and that the samples are free of precipitates. In Figure 4.5(c) we show a high magnification image of a [$LSMO_6/STO_2]_8$ superlattice. It is remarkable than even layers as thin as 2 u.c. of STO are continuous and present good structural quality.

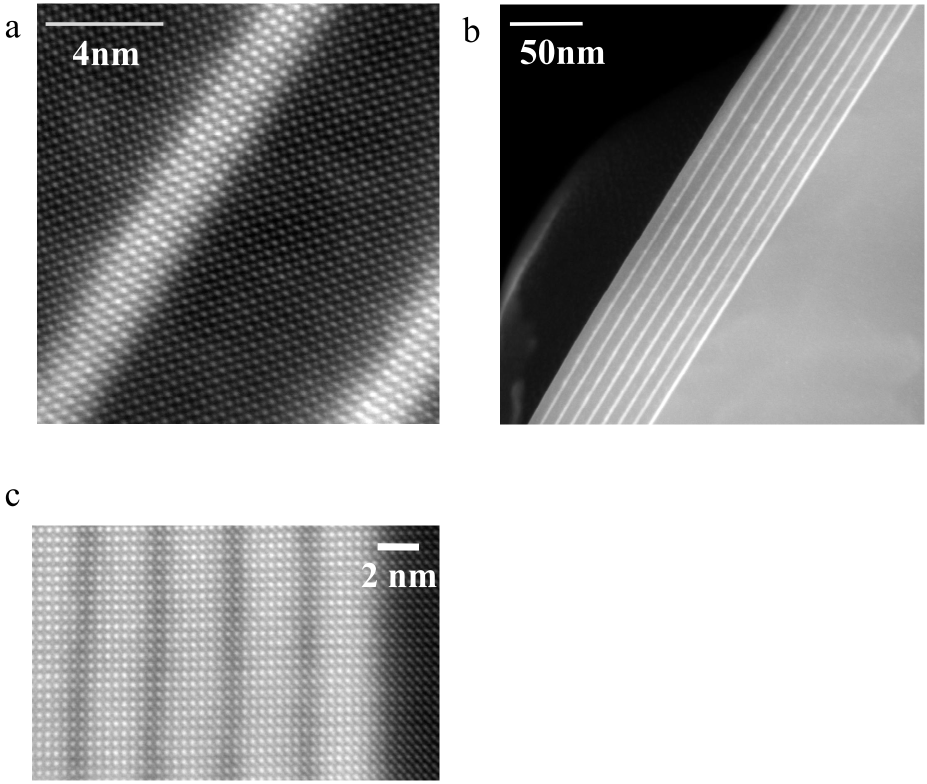

Figure 4.5. (a), (b) High and low magnification annular dark field scanning transmission electron microscopy image of a $[LSMO_6/STO_{18}]_8$ superlattice. (c) High magnification annular dark field scanning transmission electron microscopy image of a $[LSMO_6/STO_2]_8$ superlattice.

2.3 Summary

We have shown that we are able to grow superlattices with STO layers as thin as two unit cells with high quality interfaces. We have calculated the lattice parameters of LSMO and demonstrated that the samples are always fully strained; the in plane lattice parameter of the LSMO is always that of the substrate.

3 $La_{0.7}Sr_{0.3}MnO_3$ Thin Films and Critical Thickness

We studied the critical thickness for thin films grown in our laboratory. We did this because the extent to which the growth method affects the dead layer in the LSMO/STO interface is not clear. With this objective in mind we have grown thin films with thickness: 40, 20, 10, 7 and 5 u.c. In Figure 4.6 (a) we show the resistivity vs. temperature plot for the thin films. All the thin films, except for the one 5 u.c. thick, show metallic behavior at low temperatures. The low temperature resistivity in our samples is $\rho(T=10K) = 8 \times 10^{-5}\Omega$ cm similar to the one obtained by Huijben *et al.* in samples grown by pulsed laser deposition and similar to bulk LSMO values [23]. From these measurements we can determine that the critical thickness in our system is no higher than 7 u.c. In Figure 4.6 (b) and (c) we show magnetic hysteresis loops and magnetization versus temperature data. The 20 u.c. thick sample has a Curie temperature of 350 K and saturation magnetization of 3.66 μ_B/at_{Mn}. The saturation magnetization is the same as in bulk LSMO and the Curie temperature is slightly lower than the 369K of bulk manganite. To put this into perspective, however, we are not aware of reports with even as high a Curie-temperature in ultra-thin films.

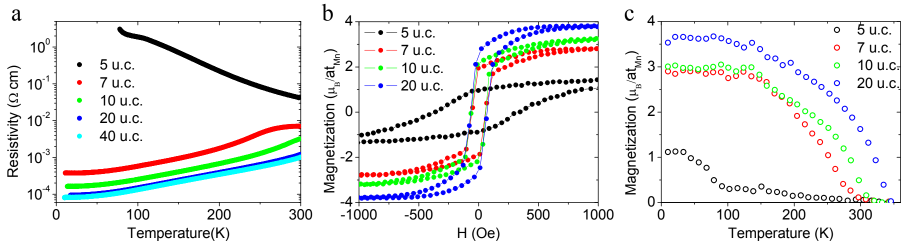

Figure 4.6. (a) Resistivity as a function of temperature for $La_{0.7}Sr_{0.3}MnO_3$ thin films N u.c. thick. (b) Magnetization as a function of field measured at T = 10 K. (c) Magnetization as a function of temperature measured with 1 kOe applied field for $La_{0.7}Sr_{0.3}MnO_3$ thin films N u.c. thick after cooling the samples in 10kOe field.

4 Magnetism and Electronic Transport

We have measured the magnetic and transport properties of a series of LSMO/STO heterostructures. The thickness of the LSMO layer was chosen as thin as possible to study the magnetic properties of the LSMO/STO interface. Nevertheless the LSMO cannot be made too thin if we want to maintain metallic and magnetic heterostructure as discussed in the preceding section. Therefore we fixed the LSMO thickness in 6 u.c. and measured magnetic and transport properties of $[LSMO_6/STO_N]_8$ heterostructures with increasingly thick STO spacers, where N = 1, 2, 5, 6, 12, 18, and 24 u.c.. A LSMO thin film of 48 u.c. was also grown in a multilayer protocol, equivalent to N=0. Notice that all these samples have the same LSMO volume and the only change between samples is the thickness of the insulating spacer

4.1 Magnetic properties

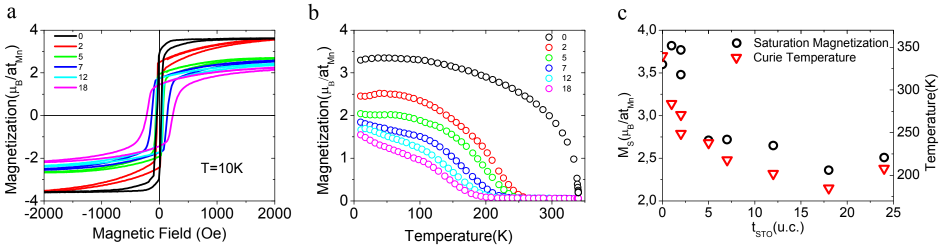

Figure 4.7. (a), (b) magnetization as a function of field (measured at T = 10K) and temperature (measured with 100 Oe) for $[LSMO_6/STO_N]_8$ superlattices measured after cooling the samples with a 10 kOe magnetic field. (c) Curie temperature and saturation magnetization at T = 10K for $[LSMO_6/STO_N]_8$.

In Figure 4.7 (a) and (b) we show the magnetization as a function of field (at 10K) and temperature for $[LSMO_6/STO_N]_8$ superlattices. The superlattice with N=0 is the 48 u.c. thick manganite thin film. As the STO spacer thickness is increased the saturation magnetization of the samples is gradually reduced. Note that for the $[LSMO_6/STO_2]_8$ superlattice M_S is equal to the thin film at 3.7 μ_B/at_{Mn}. The coercive field (H_c) of the samples decreases with decreasing STO spacer thickness from $H_c \approx 250$ Oe for $[LSMO_6/STO_{24}]_8$ to $H_c \approx 30$ Oe for the 48 u.c. thin film. The small coercive field in the 48 u.c. thin film is another indication of the high quality of the samples. This increase in coercive fields is similar to that observed in a single isolated LSMO 6 u.c. thick thin film grown on STO with a coercive field of 350 Oe (Figure 4.8). For samples with thick STO we obtain T_C=200K while in the case of the $[LSMO_6/STO_2]_8$ sample the T_C increases up to 280K accompanying the increased magnetization shown in Figure 4.7(c). For a 6 u.c. thick thin film the obtained values of saturation magnetization and Curie temperature are $M_S^{TF}=1.5\mu_B/at_{Mn}$ and T_C^{TF}=150K, similar to those of the heterostructures with STO thicker than 5 u.c. Thus multilayers with thick STO behave like the sum of isolated LSMO layers whereas with thin STO the whole heterostructure determines the properties showing that there exists some kind of coupling between the layers. To verify this hypothesis we performed magnetic measurements on four samples: two thin films 6 and 12 u.c. thick, and $[STO_2/LSMO_6/STO_2]$ trilayer and a $[LSMO_6/STO_2]_2$ superlattice (with only two repetitions). Figure 4.8 shows sketches of the samples: all of them are composed with two sorts of building blocks, a 6 u.c. LSMO thin film and a 2 u.c. STO thin film. The 6 u.c. LSMO thin film and $[STO_2/LSMO_6/STO_2]$ trilayer have a similar hysteresis loop proving that the top and bottom STO layers have no effect on the magnetization of the LSMO layer. However the 12 u.c. thick film and the $[LSMO_6/STO_2]_2$ have the same M_S values. This shows that even though the STO 2 u.c. layer has no effect on the magnetization of the LSMO, it does have an important effect when separating two LSMO layers. The LSMO layers can "communicate" with each other through this ultrathin STO.

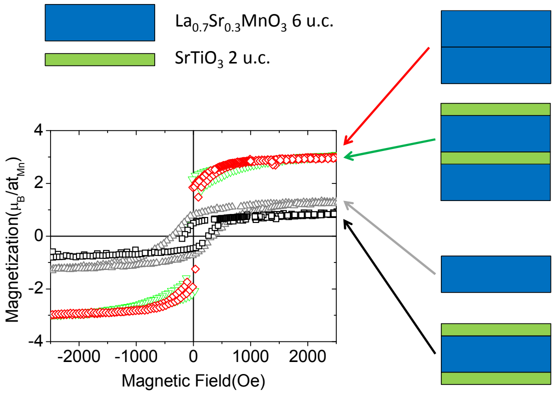

Figure 4.8. Magnetic hysteresis loops measured at T = 10K of $La_{0.7}Sr_{0.3}MnO_3$ thin films 6 u.c. (grey), 12 u.c. (red), $[LSMO_6/STO_2]_2$ (green) and $[STO_2/LSMO_6/STO_2]$ (black).

4.2 Transport properties

The resistivity (measured in Van der Pauw geometry) vs. temperature with an applied magnetic field of 140 kOe in the plane of the sample (open symbols) and with no applied field (solid symbols) for a thin film and three superlattices with STO thickness N = 2, 7 and 18 u.c. is shown in Figure 4.9 (a). The resistivity measurements are normalized to the LSMO thickness, the same for all samples. We find a strong increase of the metallic state resistivity when the STO thickness is increased. This increase is of at least 2 orders of magnitude when comparing samples with 2 u.c. STO and 18 u.c. STO at 50K. In Figure 4.9 (b) we observe a plot of the conductivity (green triangles) vs. STO thickness where this trend is clear. While above 5 u.c. of STO the conductivity is almost thickness independent, below this thickness it increases dramatically. Moreover in the same figure we compare the insulator to metal transition temperature (peak temperature) which shows a similar trend. It is important to remark that since the layers are uniformly strained, changes observed in magnetic and transport properties cannot be explained in terms of a change in strain state. The application of a 140 kOe field has a pronounced effect in reducing the low temperature resistance of samples with STO thicker than 5 u.c., the magnetoresistance at 10 K is shown in Figure 4.9 (c). This evidences that the degraded magnetic and transport properties of the samples with thick STO are related to a disordered spin structure in the LSMO which may be in fact the origin of the widely reported "dead layer" observed when its thickness is reduced.

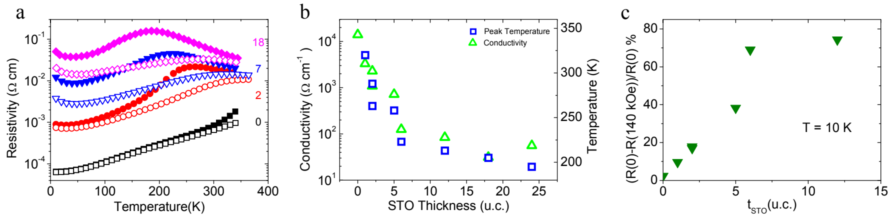

Figure 4.9. (a) Resistivity as a function of temperature with 140 kOe applied magnetic field (open symbols) and with zero field (closed symbols) of $[LSMO_6/STO_N]_8$ superlattices. (b) Conductivity at T = 50 K (green triangles) and insulator to metal transition temperature (blue squares) of $[LSMO_6/STO_N]_8$ superlattices. (c) Magnetoresistance measured at T = 10 K of $[LSMO_6/STO_N]_8$ superlattices.

4.3 Magnetism and Transport properties related

Electronic transport and magnetic properties at low temperature in manganites are linked by the double exchange mechanism where the hopping amplitude of electrons between neighboring Mn atoms is proportional to $\cos(\theta_{ij}/2)$ where θ_{ij} is the angle between the localized t_{2g} spins. Hence a fully magnetized sample with all the spins aligned (in 140 kOe) ought not to present a change in resistivity. Nevertheless, if the spins in Mn sites are misoriented, then the application of a magnetic field should align them with a concomitant decrease in resistivity. The magnetoresistance of the 48 u.c. LSMO thin film at 10K is only 2% and in the case of the $[LSMO_6/STO_2]_8$ superlattice it reaches 10% (Figure 4.9 (a) and (c)) these low values of magnetoresistance are consistent with ordered (parallel) spin states. This can also be deduced from the fact that the saturation magnetization (M_S) of these samples is 3.7 μ_B/at_{Mn} the full theoretical spin only moment. However, the superlattices with thick STO have much larger magnetoresistance at 10K, 70% for $[LSMO_6/STO_7]_8$ and $[LSMO_6/STO_{18}]_8$, evidencing a disordered spin state in these samples consistent with the values of M_S=2.5 μ_B/at_{Mn} observed in Figure 4.7 (a).

5 Electron Energy Loss Spectroscopy

We have performed electron energy loss spectroscopy (EELS) to study the oxidation state of Ti and Mn in the superlattices. In stoichiometric samples these should be Ti^{4+} and $Mn^{3.3+}$. Because the magnetic coupling between LSMO layers occurs in samples with STO layers of 2 u.c. we first investigated a $[LSMO_6/STO_2]_8$ sample. In Figure 4.10 (a) we observe a high magnification Z-contrast image of the sample with an area marked “spectrum image” were the corresponding EELS spectra is obtained. In Figure 4.10 (b) and (c) we show the raw EELS spectra and the data after applying principal component analysis (PCA) [35]. Applying the multiple linear least square (MLLS) fit (described in chapter 3 section 3.1) to the reference spectra of the O K edge shown in Figure 4.10 (e-g) for O surrounding Ti and Mn we were able to obtain the oxidation state in these atoms. The obtained oxidation states are Ti = 3.75+/- 0.05 and Mn = 3.25 +/- 0.05 as observed in Figure 4.10 (d). The fact that the oxidation state of Ti is 3.75 is rather important, because STO with this doping level is no longer an insulating material but a metal. If ultrathin STO becomes electron doped when sandwiched between LSMO this may have something to do with the observed magnetic coupling of LSMO.

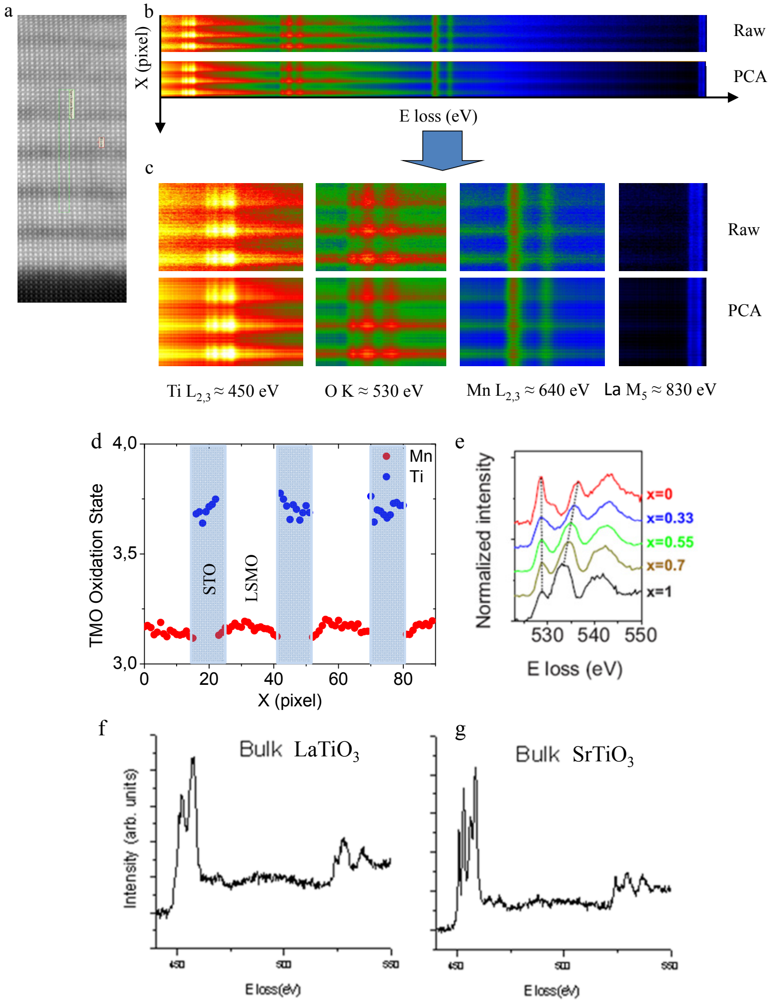

Figure 4.10. (a) High magnification annular dark field scanning transmission electron microscopy image of a [LSMO$_6$/STO$_2$]$_8$ superlattice. (b), (c) Electron energy loss spectroscopy (EELS) spectra of the same sample. The raw and after principal component analysis (PCA) data is shown. (d) Mn (red) and Ti (blue) oxidation state in a [LSMO$_6$/STO$_2$]$_8$ superlattice. (e), (f), (g) O K edge spectra of La$_{1-x}$Sr$_x$MnO$_3$ [36], LaTiO$_3$, and SrTiO$_3$ respectively.

Considering the importance of this finding we performed another EELS experiment this time on a $[LSMO_6/STO_N]_{10}$ superlattice where N varies between 2 u.c. and 8 u.c. along the stack and there are two bilayers for each STO thickness. This allows us to study in the same image the oxidation state of Ti when the STO layer thickness increases. Figure 4.11 (a) shows high magnification Z-contrast STEM image of this superlattice. In simultaneous EELS experiments, the Ti-$L_{2,3}$, Mn-$L_{2,3}$, La-$M_{4,5}$ and Sr $L_{2,3}$ edges were recorded to produce the relative concentration profile of Figure 4.11 (b) and elemental maps from the first two STO layers shown in figure (c-f). The LSMO (STO) layer looks chemically wider in the La(Ti) image than in the Mn (Sr) map indicating that both interfaces are TiO_2 terminated [37], with an extra $La_{0.7}Sr_{0.3}O$ layer at the interface. In the thicker region, interface roughness develops and the termination appears to alternate between the top and bottom interfaces. EELS elemental maps yield insights into the oxidation state of the different species through the dependence of the shape of these absorption edges on band filling. Figure 4.11 (b) shows the oxidation state of the transition metal oxide (TMO), obtained from the O K edge fine structure, through the energy separating the pre-peak and the main peak [33, 36]. This method implies some averaging of both LSMO and STO signals at the interfaces due to electron beam broadening, not taken into account by the error bars. Nevertheless, the general trend is clear; Figure 4.11 (b) shows how the Ti oxidation state evolves from $Ti^{3.7+}$ when the STO is 2 u.c. thick to stoichiometric Ti^{4+} when the STO is 8 u.c. thick. The Mn oxidation state remains constant and around 3.2+, less than the 3.3+ nominal stoichiometry. The reduced Ti oxidation state in ultrathin STO layers is consistent with an electronic reconstruction at the manganite-titanate interface. The extra $La_{0.7}Sr_{0.3}O$ layer at the interface would provide a nominal extra 1/3 e- per interfacial TiO_2 plane reducing the Ti oxidation state [33]. La-Sr intermixing could also cause the reduced oxidation state of Ti. However, this can be excluded for at least two reasons: in Figure 4.11(b) negligible La signal is detected in the STO layer, and furthermore, electron doping of STO caused by La enrichment implies a hole enrichment of the LSMO near the interface, which is not observed. The reduced Mn oxidation state (3.2+ vs. the nominal 3.3+) possibly indicates a small density (2%) of O vacancy doping.

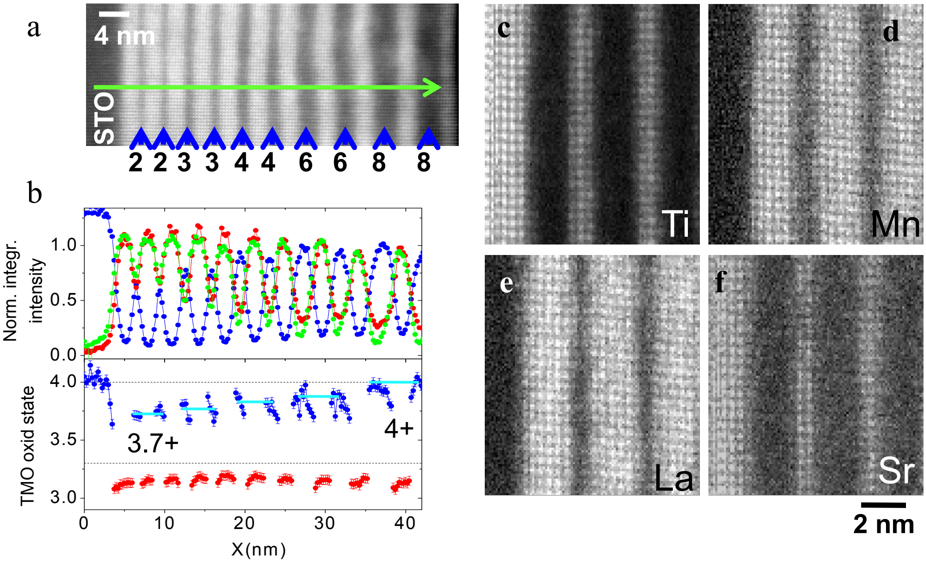

Figure 4.11. (a) High magnification Z-contrast image of a [LMSO$_6$/STO$_N$] superlattice where the STO layer thickness is varied between 2 and 8 u.c., thickness is indicated in the figure. (b) Top: normalized integrated intensity of Ti-L$_{2,3}$(blue), Mn-L$_{2,3}$(red), La M$_{4,5}$(green) along the direction marked with a green arrow on (a). Bottom: Mn (red) and Ti (blue) oxidation states. The blue lines are guides to the eye. (c-f) Atomic elemental maps corresponding to the (c) Ti L$_{2,3}$, (d) Mn L$_{2,3}$, (e) La M$_{4,5}$, (f) Sr L$_{2,3}$ signals, after fitting the background to a power law and integrating 30 eV wide windows under the remaining edges, except for (f) where a 300 eV wide window was used due to the poor signal. Datasets in (a), (b) obtained in a VG Microscopes HB501UX, while datasets in (c-f) were obtained in the Nion UltraSTEM, both operated at 100 kV and equipped with aberration correctors and Gatan Enfina spectrometers.

6 X-Ray Magnetic Circular Dichroism

X-Ray absorption measurements with polarization analysis were performed at ID08 beamline of the European Synchrotron Radiation Facility. The X–Ray magnetic circular dichroism (XMCD) measurements were carried out using a Total Electron Yield (TEY) detection method. To obtain the XMCD signal we have subtracted the absorption spectra obtained with positive and negative circularly polarized light with a 1o kOe magnetic field applied parallel to the X-ray beam direction. The XMCD signal was then divided by the corresponding absorption edge jump to take into account that we are probing different amounts of material in each sample. To illustrate this process we first show the X-ray absorption spectra (XAS) obtained at 5K of $[LSMO_{14}/STO_2]_8$ in Figure 4.12 (a) and (b) corresponding to Mn $L_{2,3}$ and Ti $L_{2,3}$ edge respectively. In Figure 4.12 (c) and d the XAS spectra obtained with circularly polarized light with positive (red) and negative polarizations (black) are shown.

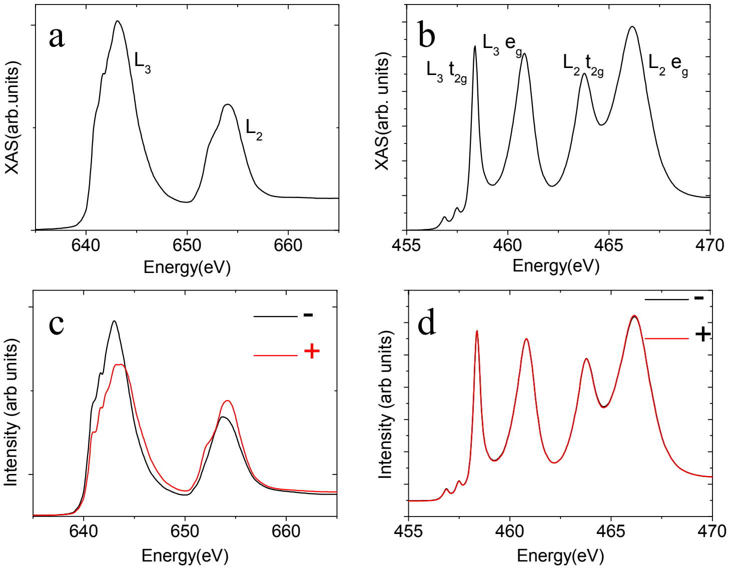

Figure 4.12. (a) Mn and (b) Ti isotropic X-ray absorption spectra of a [$LMSO_{14}/STO_2$] superlattice. (c) Mn and (d) Ti X-ray absorption spectra of a [$LMSO_{14}/STO_2$] superlattice obtained with positive (red) and negative (black) circular polarized light. All the spectra are measured at T = 5 K and with 10 kOe applied magnetic field.

6.1 Magnetic Ti at the LSMO/STO interface

Although in the case of Mn the difference in the spectra obtained with different polarizations is clear, in the case of Ti a closer inspection is needed. In Figure 4.13 we show the XMCD signal for this sample and a STO substrate. It is clear that the dichroic signal in Ti albeit small is still present in the case of the superlattice and is not present in the case of the STO substrate. This rules out any experimental error as the origin of the Ti dichroic signal.

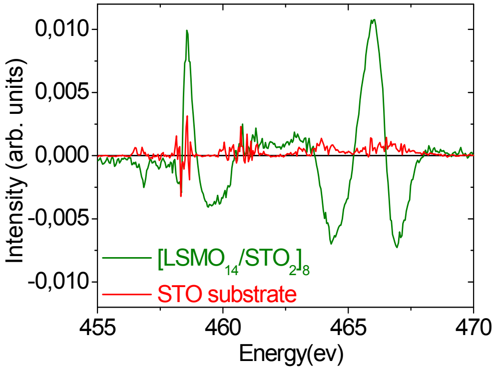

Figure 4.13. X-ray magnetic circular dichroism Ti signal of a [LMSO$_{14}$/STO$_2$] superlattice (green) and a SrTiO3 substrate (red). All the spectra are measured at T = 5 K and with 10 kOe applied magnetic field.

In Figure 4.14 we show x-ray absorption (XAS) and XMCD measured in a [LSMO$_6$/STO$_2$]$_8$ heterostructure. Figure 4.14 (a) and (b) display XAS spectra (black line) and the integrated XAS intensity (red line) for Mn and Ti respectively. In Figure 4.14 (c) and (d) we show XMCD spectra (black line) and the integrated XMCD intensity (red line) for Mn and Ti respectively. Although we know that the 2p spin-orbit splitting of the light transition metal ions is not large enough to obtain accurate spin moment (s_z) values from the sum rules, we use them anyway to obtain a rough estimate and to determine the spin moment orientation [38, 39]. We can obtain from Figure 4.14 the values of integrals of the XAS spectra (r), the XMCD spectra (q), and the XMCD signal of the L_3 edge (p). Sum rules for spin and orbital moment are [38] :

$$s_Z = -\frac{(3p-2q)}{r} n_h \qquad (6.1)$$

$$l_Z = -\frac{2q}{3r} n_h$$

where n_h is the number of holes in d shells (9 and 6 for Ti and Mn respectively). The obtained values for the [LSMO$_6$/STO$_2$]$_8$ sample are s_z=1.2 μ_B/at$_{Mn}$ and l_z=0. From the bulk magnetism measurements we know that the magnetic moment is 3.7μ_B/at$_{Mn}$, so sum rules are underestimating the spin magnetic moment. The orbital moment is 0 because orbital moment is quenched in manganites. The XMCD signal of Ti is far weaker but we can still apply sum rules and obtain s_z=-0.04μ_B/at_{Ti}, here the negative value indicates that the orientation of the spin magnetic moment is contrary to the applied magnetic field and to the Mn magnetic moment. To calculate the magnetic moment we have taken into account that only Ti in 3+ oxidation state is contributing to the magnetic signal (Ti^{4+} has no electrons in the d band) and because Ti oxidation state in this sample is 3.7+ (30 % of Ti is 3+ oxidation state and 70% is in 4+ oxidation state) we have multiplied the obtained s_z by 10/3.

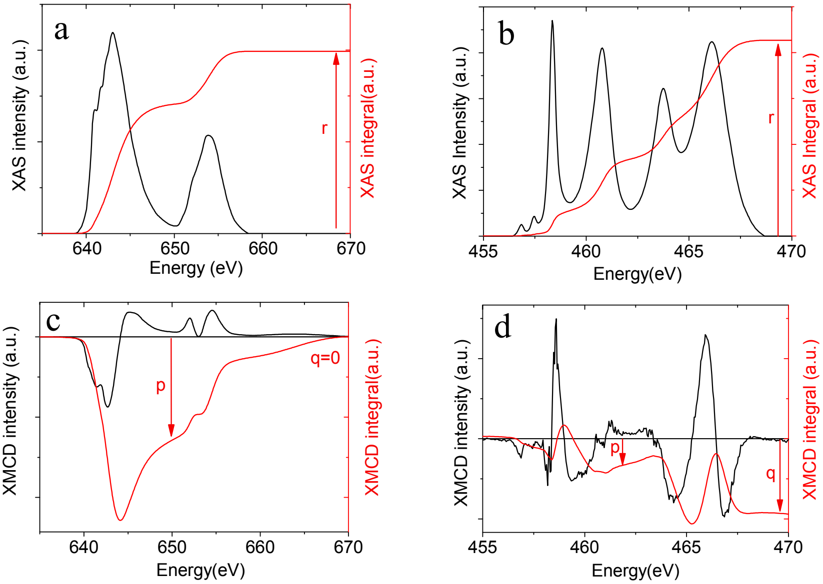

Figure 4.14. (a), (b) Iisotropic X-ray absorption (black) spectra of a [$LMSO_{14}$/STO_2] superlattice corresponding to Mn and Ti, the integrated signal r (red) is indicated. (c), (d) X-ray magnetic circular dichroism Mn and Ti signal of a [$LMSO_{14}$/STO_2] superlattice respectively. The integrated X-ray magnetic circular dichroism signal (q) is indicated as well as the L_3 edge integrated signal (p). All the spectra are measured at T = 5 K and with 10 kOe applied magnetic field.

6.2 XMCD – Thickness dependence

In Figure 4.15 (a) and (c) we represent the Mn and Ti XMCD signal respectively for a series of superlattices with constant STO thickness of 2 u.c. and LSMO thickness of 4 u.c. (red), 6 u.c.(green) and 14 u.c.(black). The Mn

XMCD signal intensity for samples with 6 and 14 u.c. of LSMO is essentially of the same magnitude while for the sample with 4 u.c. LSMO is reduced because of critical thickness. Interestingly the ratio between Mn and Ti signal taken at 642.8 eV and 466 eV respectively (the maximum intensity points) is approximately 30 in the three cases. In Figure 4.15 (b) and (d) we show Mn and Ti XMCD spectra for 2 superlattices, respectively with STO thickness of 2 u.c. and 6 u.c., and with constant LSMO thickness 6 u.c. Because the magnetic interaction between Mn and Ti only occurs at the interfacial STO, in the case of 6 u.c. STO we multiply the XMCD signal by 3 the ratio between interfacial STO (2 u.c.) and the total thickness of the layer.

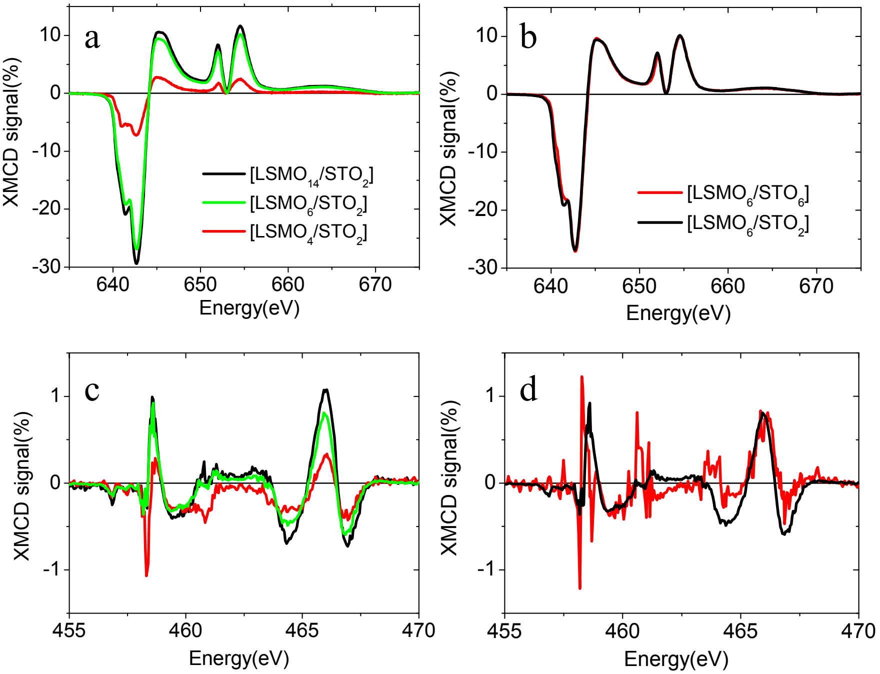

Figure 4.15. (a), (b) Mn, (c), (d) Ti X-ray magnetic circular dichroism signal of a [LMSO$_M$/STO$_N$]$_8$ superlattice. Superlattice thickness is indicated in the figure. All the spectra are measured at T = 5 K and with 10 kOe applied magnetic field.

6.3 XMCD – Temperature dependence

If we study the temperature dependence of the dichroic signal in Ti we obtain more clues about its origin. In Figure 4.16 we show temperature dependent XMCD spectra for [LSMO$_6$/STO$_2$]$_8$ sample. It is clear that both the Mn and Ti signal decreases with increasing temperature.

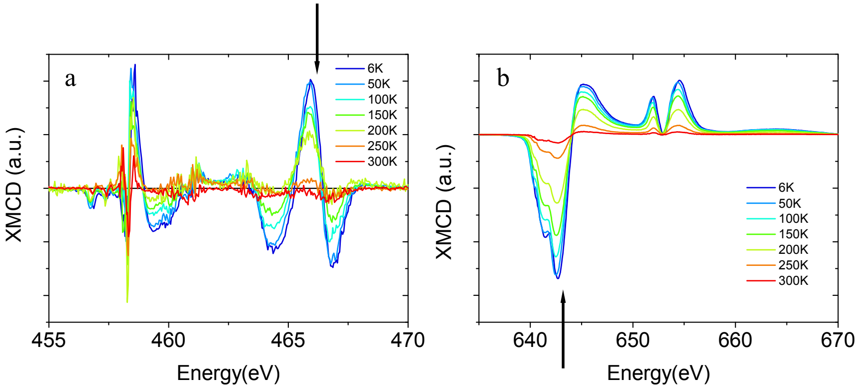

Figure 4.16. (a), (b) Ti and Mn X-ray magnetic circular dichroism signal of a [LMSO$_6$/STO$_2$]$_8$ superlattice. The spectra are measured as a function of temperature, indicated in the figure, and with 10 kOe applied magnetic field.

To better understand the meaning of this temperature dependence we now plot the Mn and Ti XMCD signal at the energy where they reach a maximum (642.8 eV for Mn and 466 eV for Ti) as a function of temperature normalized to the intensity at 5K. Moreover we also plot in Figure 4.17 the normalized magnetization of the same sample measured in the VSM. From the figure it is clear that the magnetic moment in Ti follows the temperature dependence of the magnetic moment in Mn and, as a consequence, the magnetization of the sample.

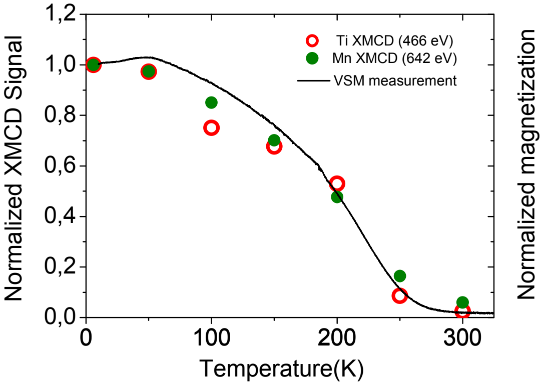

Figure 4.17. Ti (red) and Mn (green) X-ray magnetic circular dichroism signal of a $[LMSO_6/STO_2]_8$ superlattice. Ti signal is measured at 466 eV and Mn signal is measured at 642 eV. Magnetization vs. temperature data of the same sample measured in vibrating sample magnetometer. All the signals are normalized to the value at T = 5 K.

6.4 Summary

We have proven the presence of magnetic Ti atoms in $[LSMO_N/STO_M]_8$ superlattices. We have investigated the origin of this magnetic moment with different experiments. We have shown that the temperature dependence of the XMCD signal in Ti follows the one in Mn. We have shown that for samples with constant STO thickness where the Mn XMCD signal is varied by reducing the LSMO thickness, the ratio of the Mn to Ti is approximately constant. Moreover in samples with constant LSMO thickness but with different STO thicknesses, the Mn to Ti signal ratio is constant only when the Ti signal is normalized to interfacial Ti. From the first two observations we can conclude that magnetic moment in Ti is originated by interaction with Mn because it follows its temperature and magnitude dependence. From the third observation we can conclude that only Ti at the interface is magnetic, this is not strange if we take into account that only Ti at the interface is interacting with Mn. The nature of this interaction will be discussed below.

7 Molecular Orbitals

In this section we analyze the magnetic interaction at the LSMO/STO interface derived from the hybridization of Mn and Ti orbitals [40]. Orbitals with a component (z) directed towards the interface will be hybridized, hence the interfacial hybridization between $d_{3z^2-r^2}$ and $d_{xz,yz}$ orbitals will be much larger than that between d_{xy} and $d_{x^2-y^2}$. In Figure 4.18 we show the level diagram of titanate/manganite interface including e_g and t_{2g} orbitals. For simplicity, only bonding (B) orbitals are presented. The highest occupied molecular orbital could be either B up $d_{3z^2-r^2}$ or $d_{x^2-y^2}$ orbital (Figure 4.18 (b)) or B down $d_{xz,yz}$ orbital (Figure 4.18(c)). In the first case an induced magnetic moment in the Ti region will be tiny but parallel to the moment in the manganite region while in the second case depending on the relative up and down electron density in the B $d_{xz,yz}$ orbital the induced moment will be parallel or antiparallel. Because the induced moment in STO is found to be antiparallel we conclude that this last case is the one realized in our LSMO/STO interface. When the number of t_{2g} electrons is increased, such as doped titanates, electrons tend to enter the down B $d_{xz,yz}$ orbitals. In our case although the STO is nominally undoped, due to the presence of an extra $La_{0.7}Sr_{0.3}O$ plane at the interface, STO becomes electron doped as discussed above in section 5. The molecular orbital picture gives a qualitative explanation about the origin of the magnetic moment of Ti atoms and about the fact that charge transfer from LSMO to STO occurs at this interface.

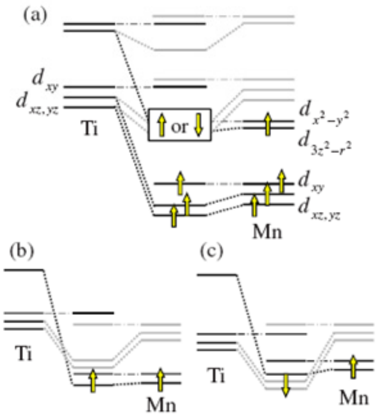

Figure 4.18. (a) Molecular orbitals formed by 3d orbitals on Mn and Ti, originally d0. Here, only bonding orbitals are shown. Full level diagram including both e_g and t_{2g}. Black (light) lines indicate the level of majority (minority) spins. The highest occupied molecular orbitals and the magnetic alignment depend sensitively on the detail of the interface as shown in (b) and (c). (b)[(c)] The up B orbital of $d_{3z^2-r^2}$ orbital is lower (higher) in energy than the down B orbitals of $d_{xz,yz}$. In (b), induced magnetic moment in Ti is parallel to Mn, i.e., $(d_{3z^2-r^2})^0$ configuration while in (c), it depends on the relative occupancy of Ti $d_{xz,yz}$ orbitals in the up and down B orbitals. When the occupancy of the Ti down $d_{xz,yz}$ orbitals is larger than the up $d_{xz,yz}$ orbitals, net moment induced in Ti site becomes antiparallel to the Mn moment. Taken from [40].

8 Magnetic Coupling Mediated by Ti

We now discuss the enhanced magnetization and transport of the samples with ultrathin spacers [$LSMO_6/STO_2]_8$ in terms of a magnetic coupling mechanism mediated by the Ti induced magnetism. A sketch of the magnetic coupling is shown in Figure 4.19. Ti atoms at the interface (Cyan STO) are antiferromagnetically aligned to Mn moments in the LSMO probably as a consequence of the hybridization process of Ti $d_{xz,\ yz}$ orbitals. These electrons residing in $d_{xz,\ yz}$ orbitals at the interface provide a mechanism for the magnetic coupling of the manganite layers if the STO layer is thin enough. The effect of coupling is to order the interface spins and so to increase the saturation magnetization and Curie temperature and to reduce the low temperature magnetoresistance. The physical mechanism of the coupling could be through direct exchange by free carriers of the STO spreading into 1-2 unit cells [41] or by a ferromagnetic superexchange mechanism between t_{2g} electrons that may be allowed by Goodenough-Kanamori rules in single occupied orbitally degenerate t_{2g} orbitals. Although we also detect a magnetic moment at interfacial Ti in samples with thicker STO layers, this magnetism is confined to the interface as in this case there are no electrons in the d band of Ti in the bulk (blue STO in figure Figure 4.19) of the STO layers. This suppresses magnetic coupling for thick STO.

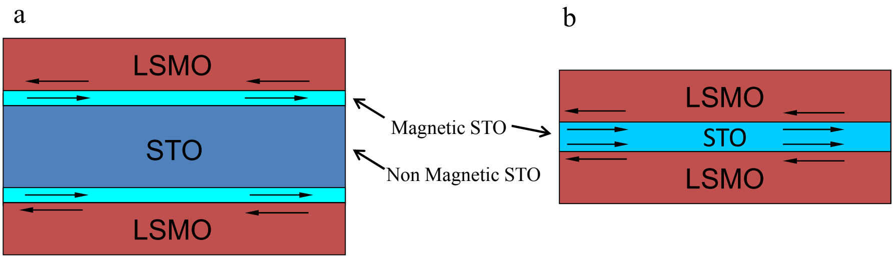

Figure 4.19. Schematic of the layer coupling scenario.(a) When STO is thick LSMO layers (red) are not coupled, non magnetic STO (blue) prevents the coupling. (b) When STO is thin LSMO layers are coupled through magnetic STO (cyan).

9 Summary and Conclusions

In summary we have found a magnetic coupling between LSMO layers through (nominally insulating and diamagnetic) STO spacers. This interaction originates at the electronic reconstruction occurring at the interface between LSMO and STO. Charge is transferred to the empty conduction band of the titanate and as a consequence the oxidation state of the Ti is reduced as shown by EELS measurements. An XMCD experiment evidences that the Mn-O-Ti superexchange interaction at the interface induces a magnetic moment in Ti. This provides the channel for the magnetic interaction between LSMO layers when the STO is thinner than 1 nm resulting in the magnetic coupling of the manganite layers and a suppression of the magnetic dead layer. The bulk magnetic and transport properties are then determined by this interfacial spin reconstruction.

These results provide evidence that the loss of magnetic correlations along the growth direction (z) at the interface is one of the fundamental factors originating the “dead layer”. When STO is made ultrathin in the superlattices, the magnetic correlations at the interfacial plane are recovered in the form of Mn-O-Ti exchange interactions. Hence MnO_2 planes will interact through the STO layer and the formation of the dead layer will be avoided.

10 References

[1] J. Park, E. Vescovo, H. Kim, C. Kwon, R. Ramesh, and T. Venkatesan, Nature (London) **392**, 794 (1998).

[2] V. Garcia, M. Bibes, A. Barthélémy, M. Bowen, E. Jacquet, J. P. Contour, and A. Fert, Phys. Rev. B **69**, 052403 (2004).

[3] M. Bowen, M. Bibes, A. Barthelemy, J.-P. Contour, A. Anane, Y. Lemaitre, and A. Fert, Appl. Phys. Lett. **82**, 233 (2003).

[4] H. Yamada, Y. Ogawa, Y. Ishii, H. Sato, M. Kawasaki, H. Akoh, and Y. Tokura, Science **305**, 646 (2004).

[5] M. Izumi, Y. Ogimoto, Y. Okimoto, T. Manako, P. Ahmet, K. Nakajima, T. Chikyow, M. Kawasaki, and Y. Tokura, Phys. Rev. B **64**, 064429 (2001).

[6] E. Dagotto, T. Hotta, and A. Moreo, Phys. Rep. **344**, 1 (2001).

[7] T. Becker, C. Streng, Y. Luo, V. Moshnyaga, B. Damaschke, N. Shannon, and K. Samwer, Phys. Rev. Lett. **89**, 237203 (2002).

[8] M. Bibes, L. Balcells, S. Valencia, J. Fontcuberta, M. Wojcik, E. Jedryka, and S. Nadolski, Phys. Rev. Lett. **87**, 67210 (2001).

[9] M. Bibes, S. Valencia, L. Balcells, Mart, iacute, B. nez, J. Fontcuberta, M. Wojcik, S. Nadolski, and E. Jedryka, Phys. Rev. B **66**, 134416 (2002).

[10] H. Yamada, M. Kawasaki, T. Lottermoser, T. Arima, and Y. Tokura, Appl. Phys. Lett. **89**, 052506 (2006).

[11] A. Tebano, C. Aruta, S. Sanna, P. G. Medaglia, G. Balestrino, A. A. Sidorenko, R. De Renzi, G. Ghiringhelli, L. Braicovich, V. Bisogni, and N. B. Brookes, Phys. Rev. Lett. **100**, 137401 (2008).

[12] F. Y. Bruno, J. Garcia-Barriocanal, M. Varela, N. M. Nemes, P. Thakur, J. C. Cezar, N. B. Brookes, A. Rivera-Calzada, M. Garcia-Hernandez, C. Leon, S. Okamoto, S. J. Pennycook, and J. Santamaria, Phys. Rev. Lett. **106**, 147205 (2011).

[13] Y. Tokura, and N. Nagaosa, Science **288**, 462 (2000).

[14] S. Okamoto, and A. Millis, Nature (London) **428**, 630 (2004).

[15] J. Mannhart, and D. Schlom, Science **327**, 1607 (2010).

[16] J. B. Goodenough, Phys. Rev. **100**, 564 (1955).

[17] J. Kanamori, J. Phys. Chem. Solids **10**, 87 (1959).

[18] K. Ueda, H. Tabata, and T. Kawai, Science **280**, 1064 (1998).

[19] J. Chakhalian, J. Freeland, G. Srajer, J. Strempfer, G. Khaliullin, J. Cezar, T. Charlton, R. Dalgliesh, C. Bernhard, and G. Cristiani, Nature Phys. **2**, 244 (2006).

[20] J. Chakhalian, J. Freeland, H. Habermeier, G. Cristiani, G. Khaliullin, M. van Veenendaal, and B. Keimer, Science **318**, 1114 (2007).

[21] P. Yu, J. S. Lee, S. Okamoto, M. D. Rossell, M. Huijben, C. H. Yang, Q. He, J. X. Zhang, S. Y. Yang, M. J. Lee, Q. M. Ramasse, R. Erni, Y. H. Chu, D. A. Arena, C. C. Kao, L. W. Martin, and R. Ramesh, Phys. Rev. Lett. **105**, 027201 (2010).

[22] J. Garcia-Barriocanal, J. C. Cezar, F. Y. Bruno, P. Thakur, N. B. Brookes, C. Utfeld, A. Rivera-Calzada, S. R. Giblin, J. W. Taylor, J. A. Duffy, S. B. Dugdale, T. Nakamura, K. Kodama, C. Leon, S. Okamoto, and J. Santamaria, Nat. Comm. **1**, 82 (2010).

[23] A. Urushibara, Y. Moritomo, T. Arima, A. Asamitsu, G. Kido, and Y. Tokura, Phys. Rev. B **51**, 14103 (1995).

[24] M. B. Salamon, and M. Jaime, Rev. Mod. Phys. **73**, 583 (2001).

[25] H. Fujishiro, M. Ikebe, and Y. Konno, J. Phys. Soc. Jpn. **67**, 1799 (1998).

[26] J. M. D. Coey, M. Viret, and S. von Molnar, Adv. Phys. **48**, 167 (1999).

[27] Y. Konishi, Z. Fang, M. Izumi, T. Manako, M. Kasai, H. Kuwahara, M. Kawasaki, K. Terakura, and Y. Tokura, J. Phys. Soc. Jpn. **68**, 3790 (1999).

[28] M. Huijben, L. W. Martin, Y.-H. Chu, M. B. Holcomb, P. Yu, G. Rijnders, D. H. A. Blank, and R. Ramesh, Phys. Rev. B **78**, 094413 (2008).

[29] M. Bibes, L. Balcells, S. Valencia, J. Fontcuberta, M. Wojcik, E. Jedryka, and S. Nadolski, Phys. Rev. Lett. **87**, 067210 (2001).

[30] A. Tebano, C. Aruta, S. Sanna, P. G. Medaglia, G. Balestrino, A. A. Sidorenko, R. D. Renzi, G. Ghiringhelli, L. Braicovich, V. Bisogni, and N. B. Brookes, Phys. Rev. Lett. **100**, 137401 (2008).

[31] J. F. Schooley, W. R. Hosler, E. Ambler, J. H. Becker, M. L. Cohen, and C. S. Koonce, Phys. Rev. Lett. **14**, 305 (1965).

[32] O. N. Tufte, and P. W. Chapman, Phys. Rev. **155**, 796 (1967).

[33] J. Garcia-Barriocanal, F. Y. Bruno, A. Rivera-Calzada, Z. Sefrioui, N. M. Nemes, M. Garcia-Hernández, J. Rubio-Zuazo, G. R. Castro, M. Varela, S. J. Pennycook, C. Leon, and J. Santamaria, Adv. Mater. **22**, 627 (2010).

[34] P. G. Radaelli, G. Iannone, M. Marezio, H. Y. Hwang, S. W. Cheong, J. D. Jorgensen, and D. N. Argyriou, Phys. Rev. B **56**, 8265 (1997).

[35] M. Bosman, M. Watanabe, D. T. L. Alexander, and V. J. Keast, Ultramicroscopy **106**, 1024.

[36] M. Varela, M. P. Oxley, W. Luo, J. Tao, M. Watanabe, A. R. Lupini, S. T. Pantelides, and S. J. Pennycook, Phys. Rev. B **79**, 085117 (2009).

[37] J. Maurice, D. Imhoff, J. Contour, and C. Colliex, Philos. Mag. **86**, 2127 (2006).

[38] C. Chen, Y. Idzerda, H. Lin, N. Smith, G. Meigs, E. Chaban, G. Ho, E. Pellegrin, and F. Sette, Phys. Rev. Lett. **75**, 152 (1995).

[39] C. Piamonteze, P. Miedema, and F. M. F. de Groot, Phys. Rev. B **80**, 184410 (2009).

[40] S. Okamoto, Phys. Rev. B **82**, 024427 (2010).

[41] G. Herranz, R. Ranchal, M. Bibes, H. Jaffrès, E. Jacquet, J. L. Maurice, K. Bouzehouane, F. Wyczisk, E. Tafra, M. Basletic, A. Hamzic, C. Colliex, J. P. Contour, A. Barthélémy, and A. Fert, Phys. Rev. Lett. **96**, 027207 (2006).

5

$La_{0.7}Sr_{0.3}MnO_3$-$LaFeO_3$-$La_{0.7}Sr_{0.3}MnO_3$ Magnetic Tunnel Junctions

The earliest fully epitaxial magnetic tunnel junctions (MTJs) based on oxide materials used half-metallic mixed-valence manganites [1] as electrodes and $SrTiO_3$ (STO) film as tunnel barrier [2]. STO is a dielectric and diamagnetic compound, isostructural to many other simple functional and multifunctional perovskites such as ferroelectric $BaTiO_3$ or multiferroic $BiFeO_3$. Replacing STO by such functional compounds in tunnel junctions brings novel device possibilities, not achievable with the materials used in current metal oxide semiconductor (CMOS) technology. In this chapter we will analyze the possibility of using $LaFeO_3$ an antiferromagnetic material as tunnel barrier. We will first describe the properties of manganite based MTJs [3, 4]. Then we will describe our work on structural and magnetic properties of $La_{0.7}Sr_{0.3}MnO_3$/LFO (LSMO/LFO) superlattices, and finally we will discuss our results on LSMO/LFO/LSMO MTJ´s.

1 Introduction

The half-metallic character of manganites was demonstrated for the first time by spin-resolved photoemission experiments [5], through which a positive spin polarization in excess of 90% was determined. Manganite-based MTJs with large TMR values were fabricated and measured some time before that [6], [7], [8], but it was only some years after Park *et al.*'s publication [5] that TMR measurements corresponding to spin polarizations exceeding 90% were measured [9]. The following are the most remarkable properties of manganite based MTJ´s [3, 4]:

1) TMR: The first TMR measurement on MTJs with manganite electrodes was reported in 1996 by Lu *et al.* [6] and Sun *et al.* [7]. The best results were obtained on junctions using optimal-doped LSMO electrodes and STO barriers with a thickness in the range of 3–6 nm. A maximum TMR of 83% was found [6] (at 4.2 K), which, according to Jullière formula [10], corresponds to a spin polarization (P) of 54% for the LSMO electrodes. The disappearance of TMR at much lower temperatures that the Curie temperature of the ferromagnetic electrodes, and the deviation from the parabolic behavior in the conductance (G) at low bias was reported by Lu *et al.*'s pioneering paper. Later, other authors reported increased TMR. Sun *et al.* reported a TMR of ~ 400%, corresponding to P ~ 81% [11]. This was soon followed by Viret *et al.*'s paper, which independently reported a 450% TMR at 4.2 K in LSMO/STO/LSMO junctions [8]. Subsequent publications by Sun *et al.* and others reported increasingly large TMR values, up to a TMR of 1850% in an LSMO/STO/LSMO MTJ, as found by Bowen et al. in 2003 [9]. This record TMR corresponds to a spin polarization of 95%, i.e., a virtually half metallic character for LSMO.

2) Temperature Dependence of the TMR: In early manganite tunnel junctions, the TMR decreased rather rapidly with temperature and disappeared at a critical temperature T^* (typically 200 K in early reports) that is well below the Curie temperature of the electrodes (up to 360 K in LSMO). This problem motivated both theoretical [12] and experimental research on manganite-based junctions and also stimulated the search for other half-metallic ferromagnets with higher T_C. Several explanations have been invoked to explain the difference between T^* and T_C: defects in the tunnel barrier causing spin flips [13, 14] and non-optimal magnetic properties at manganite/barrier interfaces (either due to oxygen deficiency [8], phase separation [15], etc.). In fact it was noticed that the electrode/barrier interface is not only important for the temperature dependence of the TMR but also in determining the spin polarization of electrons tunneling from or into the ferromagnetic electrode [16]. We note that the properties of

manganite interfaces have been explored extensively through the study of manganite surfaces [17] and manganite/insulator interfaces in thin films [18, 19] and heterostructures [20, 21] (see also chapter 4 of this thesis).

3) Bias Dependence of the TMR: In addition to its temperature dependence, the bias dependence of the TMR in manganite MTJs has also received some attention. One of the main features of the TMR (V) in manganite-based junctions is the rapid decrease of the TMR with bias voltage, at least in the low (≤ 0.2 V) bias range [11, 22, 23]. We note that this behavior is accompanied by a specific zero-bias anomaly (ZBA) in the conductance curves. In MTJs, a ZBA is usually observed and ascribed to the absorption/generation of spin waves by tunneling electrons. The ZBA in manganite junctions has been studied theoretically by Gu *et al.* [24], who proposed that, due to the double-exchange interaction, the low-bias conductance is proportional to $|V|^{3/2}$, which is in agreement with the experimental results [6, 9]. Such magnon excitations depolarize the spin of the carriers, hence decreasing the effective spin polarization and, thus, the TMR.

2 Growth and Structural Characterization

We grew LSMO/LFO heterostructures on a high pressure pure oxygen sputtering system. The samples were grown on commercial (001) STO substrates. During deposition the substrate is kept at 800ºC and the oxygen pressure at 2.8 mbar. After deposition temperature is lowered to 750ºC, at this temperature the chamber is filled with 900 mbar pure oxygen and the samples are annealed during 60 minutes to ensure proper oxygen stoichiometry. After this annealing step, samples are cooled down to room temperature at 5K/min. In section 8 we show a summary of all samples studied in this chapter. We have grown different kinds of samples depending on the targeted experiment. Superlattices consisting of 6 bilayers of LFO/LSMO were grown for structural and magnetic characterization. Bilayers and a LSMO thin film were grown for conductive tip atomic force microscopy (CTAFM) characterization of the barrier. Trilayer heterostructures were grown to optically define magnetic tunnel junctions and perform magnetotransport measurements in current perpendicular to plane geometry.

2.1 X-Ray diffraction

In Figure 5.1 we show x-ray reflectivity and diffraction for a series of superlattices were the LFO thickness of 7 u.c. is constant and the LSMO thickness is: 7 (blue), 9(green), 12(red) and 15 u.c. (black). The observed reflectivity spectra clearly exhibit a finite size effect, reflecting the smoothness of the surface. Superlattice Bragg peaks are observed also in reflectivity (see arrows in Figure 5.1) and diffraction spectra proving that interfaces are flat and sharp. As the superlattice period increases, the superlattice peaks are further separated, as observed in the diffraction spectra. Size effects allow us to determine the thickness of the superlattices (see chapter 2).

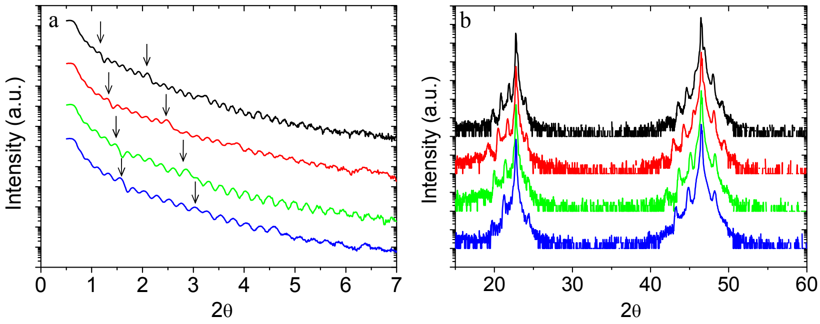

Figure 5.1. (a),(b) X-ray reflectivity and diffraction spectra of $[LFO_7/LSMO_N]_6$ superlattices. LSMO thickness (N) is: 7 (blue), 9(green), 12(red) and 15 u.c. (black).

2.2 Scanning transmission electron microscopy

Figure 5.2 displays a high-magnification Z-contrast scanning transmission electron microscopy (STEM) image of a $[LSMO_{15}/LFO_7]_{x6}$ superlattice. The layers show good epitaxial properties and coherent growth, which is in agreement with the X-ray results.

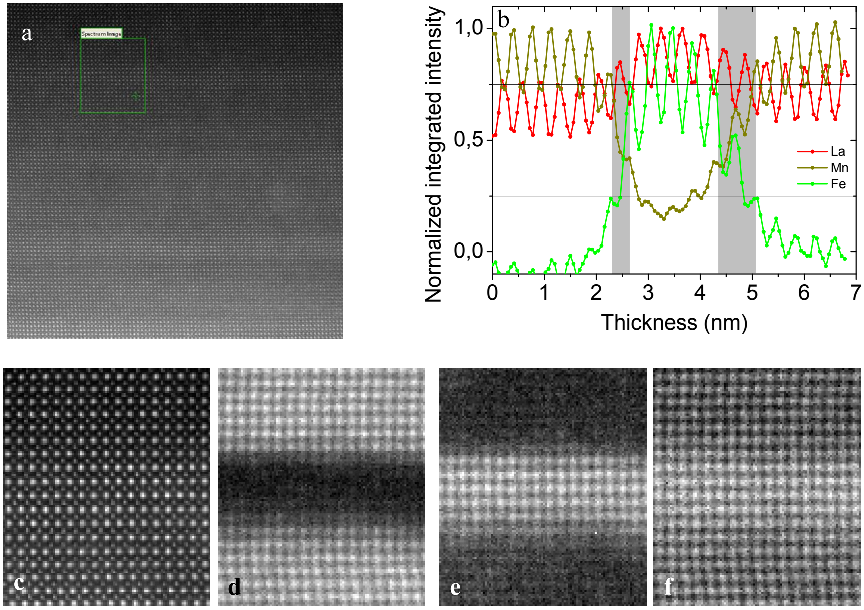

Figure 5.2. (a) high magnification annular dark field scanning transmission electron microscopy image of a $[LFO_7/LSMO_{15}]_8$ (b) Normalized integrated intensity of Fe-$L_{2,3}$(green), Mn-$L_{2,3}$(brown), La $M_{4,5}$(red) in the area marked with a green box on (a) (c-f) Atomic elemental maps corresponding to the (c) total integrated signal, (d) Mn $L_{2,3}$, (e) Fe $L_{2,3}$, (f) La $M_{4,5}$ signals.

To further explore the chemical structure of the interface two dimensional elemental maps were acquired from the area marked (spectrum image) in Figure 5.2(a). The annular dark field image of this area is shown in Figure 5.2(c). The structural quality of this interface is remarkably good. In Figure 5.2(d-f) two dimensional elemental maps corresponding to Mn $L_{2,3}$, Fe $L_{2,3}$ and La $M_{4,5}$ edge are shown. Interestingly, in the Fe map only 5 atomic planes are observed where 7 are expected according to the calculated thickness from x-rays. This betrays the presence of chemical or structural disorder that makes the LFO layer thinner than expected. In order to quantify this effect we integrated the total intensity in the elemental maps and plotted the result in Figure 5.2(b). In this plot we show the normalized integrated intensity of the elemental maps as a function of thickness. The grey shaded areas are the interfacial regions, defined as the region where the intensity of Fe signal varies from 0.75 to 0.25. In a sharp interface this interfacial region is 1 u.c. (0.39 nm) [25], in this sample we observe that the LFO on LSMO interface is 2 u.c. thick while the LSMO on LFO interface is 1 u.c. thick. There are two possibilities to explain this wider interface: the first possibility is that Fe and Mn atoms intermix forming a 2 u.c. interface with composition $La_zSr_{1-z}Mn_xFe_{1-x}O_3$ and the second possibility is that short scale interface roughness exists, in this case the microscopy measurements average through the sample, resulting in a wider interface. Asymmetric interfaces have been reported to occur in other complex oxides heterostructures, too [26].

3 Magnetic Properties of $LaFeO_3/La_{0.7}Sr_{0.3}MnO_3$ Heterostructures

3.1 Superlattices.

We have studied the magnetic properties of $[LSMO_N/LFO_7]_{x6}$ superlattices with N between 7 and 15 u.c. and LFO thickness fixed at 7 u.c., similar thickness as used for tunnel barriers in MTJ´s.

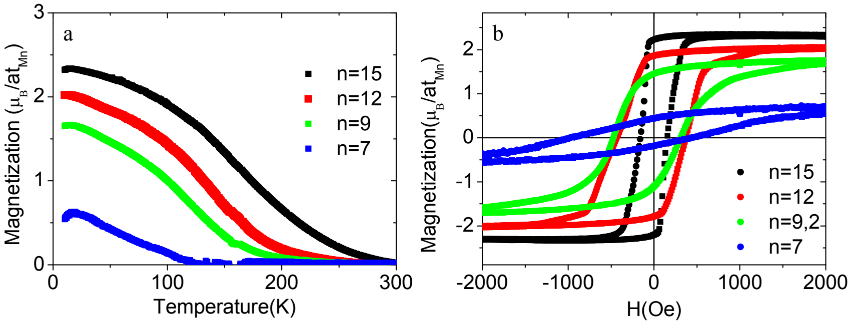

Figure 5.3. (a) Magnetization as a function of temperature, (b) and field (measured at T = 10K) respectively, for $[LFO_7/LSMO_N]_6$ superlattices (N is indicated in the graph) measured after cooling the samples in a 10 kOe magnetic field.

In Figure 5.3(a) we observe the magnetization versus temperature measurements for samples with N = 7 (blue), 9 (green), 12 (red) and 15u.c. (black), taken during warming up in a 1 kOe applied field after cooling in 10kOe magnetic field. Figure 5.3(b) shows magnetic hysteresis loops measured at 10K after cooling the samples in 10kOe magnetic field. From these measurements we can extract the saturation magnetization (M_S) and Curie temperature (T_c) of the samples. These values are smaller than those of LSMO thin films. The reduced thickness of the manganite and the presence of an interface may cause this effect, as extensively discussed in chapter 4. However, the added effect of the antiferromagnetism in the LFO layers, absent in the case of diamagnetic STO, may play an important role. The main question here is the result of these two competing orders, ferromagnetism vs. antiferromagnetism [27], at the interface. In fact it is known that when the interface between and AF and a F material is cooled through the Neel temperature of the AF (with the Curie temperature of the FM larger than T_N) an anisotropy, “exchange bias”, is induced in the FM [28]. In the present case T_N is higher than $T_{C.}$ However it is still possible under these circumstances to observe exchange bias. The fact that and exchange bias field (H_e) reaching values of H_e=170 Oe and H_e= 60 Oe is observed in samples with 7 and 9 u.c. of LSMO proves that in the case of thin LSMO AF is present in the LFO. In the case of LSMO 15 u.c. no exchange bias is observed, although we cannot conclude from this that AF is not present on LFO because the exchange bias decreases exponentially with the ferromagnetic thickness. From the present measurements we can conclude that LSMO magnetic properties close to LSMO/LFO interface are depressed, this fact shows up as lower M_s and T_c than in bulk. These findings may be explained based on either charge transfer [29], or spin canting [30] at the interface, although we do not have enough data to support any of these.

3.2 Bilayers and trilayers.

In Figure 5.4 we show measurements of the magnetic properties of the following samples: [$LSMO_{90}/LFO_9/LSMO_{20}$] (green), [$LSMO_{90}/LFO_9$] (black) and [$LFO_9/LSMO_{90}$] (red). These samples have the same structure as each part of MTJs. The first sample has the same structure as the one used to fabricate MTJs, the second sample has the thickness of bottom electrode and barrier and the third sample of the barrier and top electrode. Although magnetic properties may change during the patterning process, nevertheless it is worthwhile to have information on the Curie temperature, coercive fields and anisotropy of the different magnetic layers. In Figure 5.4 (a) and (b) we show the magnetic hysteresis loop measured at 10K and 305K after cooling the samples with 10 kOe applied field. The samples are still magnetic at room temperature, with Curie temperature of ~ 350K Figure 5.4(c). However the coercive fields of the top and bottom electrode are similar and this will makes it hard to achieve antiparallel alignment of the layers. No exchange bias is observed, not surprisingly considering that LSMO layers are relatively thick.

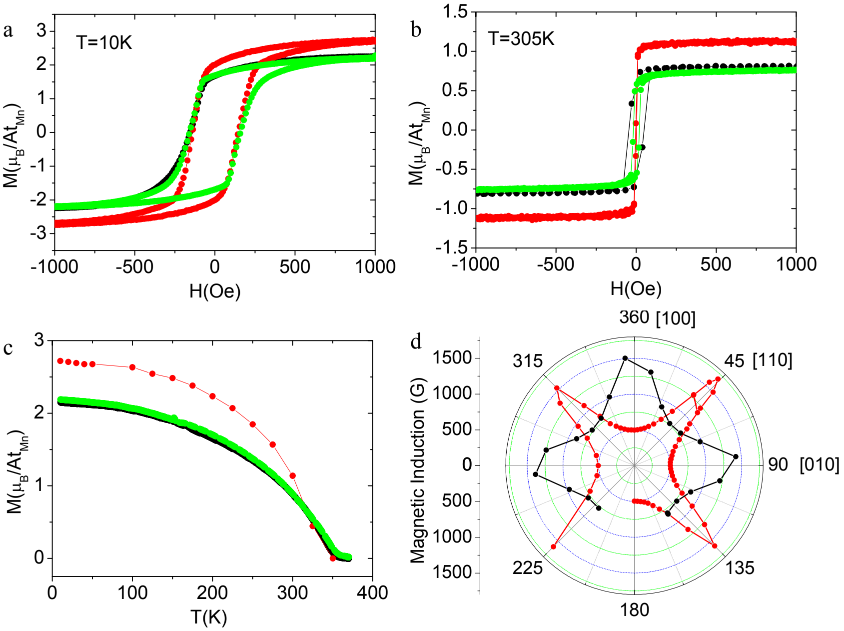

Figure 5.4. (a), (b) Magnetization as a function field measured at T = 10 K and 305K respectively. (c) Magnetization as a function of temperature measured in 1 kOe applied field after cooling the sample with 10 kOe. (d) FMR positions show in polar plot. Samples are [$LSMO_{90}/LFO_9$] (black), [$LSMO_{90}/LFO_9/LSMO_{20}$] (green) and [$LFO_9/LSMO_{20}$] (red)

In order to obtain high values of TMR it is important to realize a state in the MTJ where the top and bottom electrode are AF aligned [4]. If an angle other than 180° exists between the magnetization of top and bottom electrode then depressed TMR is observed. To obtain a perfect antiparallel alignment it is important then that the LSMO layers have the same easy magnetization axis. We performed ferromagnetic resonance (FMR) measurements at 77K in two different samples: [$LSMO_{90}/LFO_9$] (black), [$LFO_9/LSMO_{20}$] (red). As mentioned above, these samples mimic the behavior of the top and bottom electrode respectively. Figure 5.4 (d) shows the FMR field (indicated radially) extracted from the spectra on a polar plot, with the polar angle corresponding to the actual orientation of the samples in the spectrometer ([100] direction of the substrate corresponds to the 0º in the polar plot). In [$LSMO_{90}/LFO_9$] (black), the in-plane easy axes are the [110] and [1–10] while in the [$LFO_9/LSMO_{20}$] (red) the easy axes are the [100] and [010], indicated by the minimum values of the FMR field. The case of [$LSMO_{90}/LFO_9$] with biaxial anisotropy and easy axis along the [110] and [1–10] directions of the substrate is similar to that obtained in LSMO single films [31]. Surprisingly in the case of [$LFO_9/LSMO_{20}$] the magnetization easy axes is rotated 45º. Rotation of the easy axes produced by the reduced thickness of the films was observed in LCMO thin films by Nemes *et al* [32], although the thin film in that case was only 10 u.c. thick. Another possible origin of the rotation of the magnetization easy axis maybe the interaction with the LFO layer, although the LFO layer is present in both samples, the LSMO/LFO interface is very different in both cases as mentioned in section 2.

3.3 Magnetic properties summary

We have observed that close to the LSMO/LFO interface the magnetic properties of the manganite are depressed. We have found the signature of the AF state of LFO by observing exchange bias in LSMO/LFO superlattices. So we can conclude that LFO preserves its AF character even in films as thin as 7 u.c. We have shown that both top and bottom layers in [$LSMO_{90}/LFO_9/LSMO_{90}$] heterostructures are ferromagnetic at room temperature. We have also observed that the magnetization easy axes of [$LSMO_{90}/LFO_9$] and [$LFO_9/LSMO_{90}$] bilayers are rotated 45º . This fact leads us to think that the top and bottom layer in [$LSMO_{90}/LFO_9/LSMO_{90}$] heterostructures will have their respective easy axes also rotated 45º one respect to the other.

4 Electrical Resistance of $LaFeO_3$ Tunnel Barriers

In order to probe the properties of LFO thin films as tunnel barriers we performed conductive tip atomic force microscopy (CTAFM) measurements [33] on a series of [$LSMO_{31}/LFO_N$] bilayers. Samples with LFO thickness ranging from 3 u.c. up to 11 u.c. were measured. Electrical resistance maps were measured in contact mode applying a DC-bias of 2V to the LSMO layer with the tip grounded. To avoid spurious resistance values caused by tip deterioration, resistance maps on a LSMO thin film were measured before and after completing the electrical resistance maps on this set of samples verifying that the resistance obtained for LSMO thin film did not change within experimental error.

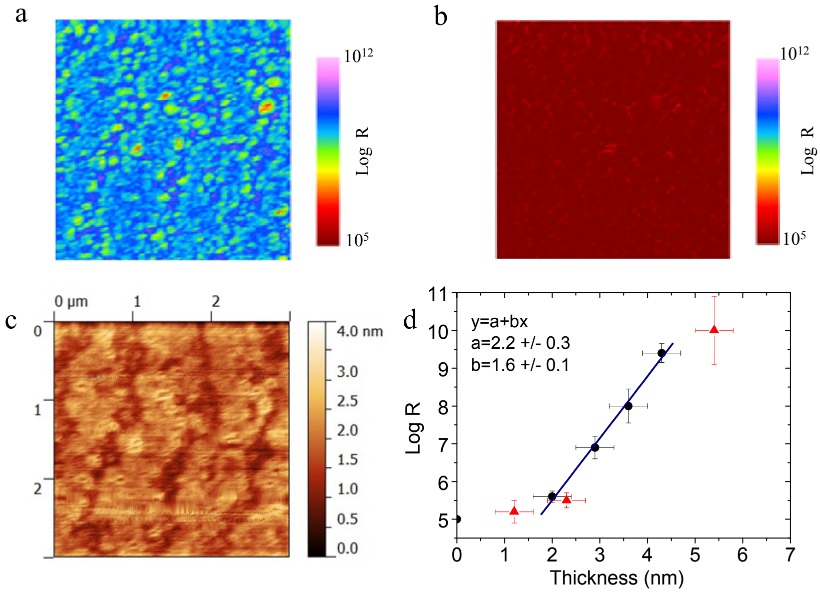

Figure 5.5. (a), (b) Resistance map simultaneously (tip sample bias is 2V) acquired over an area of 3 x 3 µm^2 of a [LSMO$_{31}$/LFO$_{11}$] and [LSMO$_{31}$] measured with a CT-AFM. (c) Topography of [LSMO$_{31}$/LFO$_{11}$] simultaneously acquired with the resistance map in contact mode. (d) Resistance as a function of LFO layer thickness on samples [LSMO$_{31}$/LFO$_{M}$], the resistance is the mean value over an area of 3 x 3 µm^2, the black line is a linear fit to the four black dots which are samples grown consecutively. The parameters of the linear fit are indicated in the graph.

In Figure 5.5 (a) and (c) we show simultaneously acquired resistance and topography taken on a 3 x 3 um^2 area of a [LSMO$_{31}$/LFO$_{11}$] bilayer. The topography of the sample shows two dimensional islands with an RMS roughness of 0.5 nm. In the resistance map of the LSMO layer (Figure 5.5(b)) we observe a homogenous resistance distribution, while in the case of the bilayer we observe that in some areas the resistance drops by one or even two orders of magnitude but it never reaches the LSMO resistance. From this we can conclude that no holes are observed in the LFO thin film but it is clear that some areas present significantly lower resistance values. When LFO layers with these properties are used as tunnel barriers the current will be channeled through this low resistance areas. In Figure 5.5(c) we show the most probable resistance values obtained from resistance histograms as a function of LFO layer thickness. The resistance of the barrier increases exponentially with the barrier thickness which is a signature of the tunneling mechanism in the electrical transport. It should be noted here that because a large bias voltage is applied, tunneling in the Fowler-Nordheim regime is expected. Nevertheless, it appears from Figure 5.5(c) that the resistance starts to increase exponentially with thickness only when LFO is thicker than 1.5 nm, this is in sharp contrast with other tunnel barriers like STO where an increase in the resistance from the first u.c. is observed [34]. We mentioned in section 2.2 that Mn-Fe intermixing or roughness may be present in the LFO on LSMO interface. The fact that n homogenous conducting layer is measured when LFO thickness is below 1.5 nm is consistent with the former scenario. If a very thin layer of $La_{0.7}Sr_{0.3}Mn_xFe_{1-x}O_3$ is formed at the interface this layer will be conducting [35].

5 Magnetic Tunnel Junctions

We have patterned three [$LSMO_{90}$ (35nm)/LFO_N (n nm)/$LSMO_{20}$ (8nm)] trilayers with LFO thicknesses N(n)= 3(1.2), 9(3.5) and 15u.c.(5.8 nm) into MTJs and measured their magnetotransport properties. These processes as well as the CTAFM measurements of section 4 were performed during a four month stay at the Functional Oxides group of the *Unite Mixte the Physique CNRS/THALES* (Palaiseau-France).

5.1 Patterning

The patterning process was carried out by standard UV photolithography techniques [36] using chromium masks that define 96 MTJs ranging in size from 6 to 128 μm^2 , some of the junctions have square shape and others rectangular shape. In the first step, pillars were defined by photolithography and ion-beam etching. The etching process was monitored with an *in situ* secondary ion mass spectroscopy apparatus to stop the etching when entering the bottom LSMO layer. In the second step, 8 200-μm-wide bottom electrodes were created using the same combination of photolithography and neutralized ion beam etching. To passivate the sample, a 250 nm-thick layer of Si_3N_4 was deposited by dc sputtering and selectively removed by reactive ion etching to define electrical access points. Finally, Ti/Au tracks were deposited as electrical contacts for transport measurements.

5.2 Magnetotransport measurements

Magnetotransport measurements of MTJs were done in a liquid helium cryostat in 3 contacts configuration sourcing voltage (see Figure 5.6(a)). In this configuration the applied voltage is measured at the junction to take into account the voltage drop on the electrode. Measurements of the bottom electrode were done in 2 contacts configuration. Although many junctions were measured we will show only the most representative data on *"working junctions"*; this represents approximately a 25% of the patterned junctions.

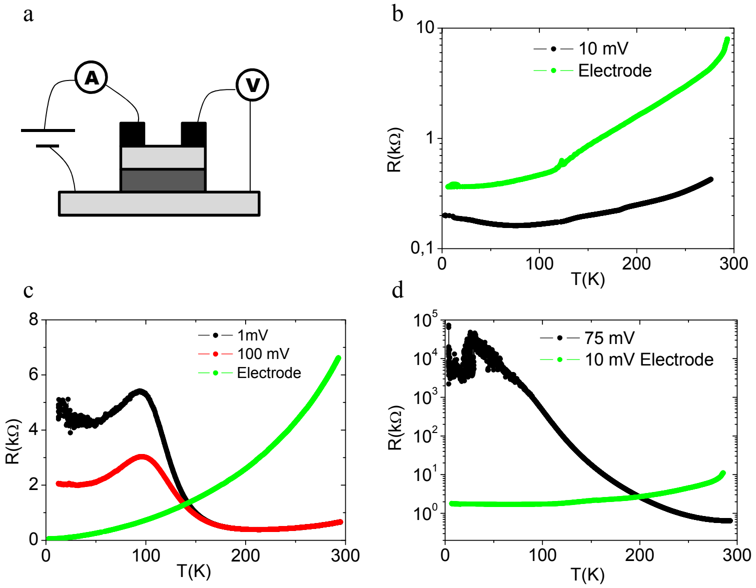

Figure 5.6. (a) Schematic of the measurement setup. (b-d) Resistance as a function of temperature for [$LSMO_{90}/LFO_M/LSMO_{20}$] magnetic tunnel junctions where the barrier thickness is M = 3, 9 and 15 u.c. respectively (black and red), the applied bias during the measurement is displayed in the figures. The resistance of the bottom electrode is also shown (green).

5.2.1 Resistance vs. temperature

In Figure 5.6 we show resistance vs. temperature measurements for the bottom electrode (green) and junction (red and black) for the three samples. Junction area and the applied bias during measurements are indicated in the figure. We observe that the bottom electrode resistance shows metallic behavior (dR/dT > 0) typical of a manganite in this temperature range. The electrode resistance decreases from ~ 10kΩ at room temperature to ~1 kΩ at 2K; this indicates that the bottom electrode was not damaged during the patterning process. We now turn to the junction resistance. When measuring the junction the bottom electrode, tunnel barrier and top electrode are being probed in series. In the case of the junctions with 3 u.c. barrier (Figure 5.6(b)) we observe that the behavior is that of a metal (dR/dT > 0), the resistance decreases when decreasing temperature over the full temperature range. In fact current vs. voltage measurements in this junctions show a linear dependence (ohmic behavior) at low temperatures revealing that in this sample there is no tunnel barrier (see section 5.2.2). This can be explained in terms of the measurements of section 5, in which we have observed that 3 u.c. LFO grown on top of LSMO are almost as conducting as LSMO. In the case of the junction with 9 u.c. barrier (Figure 5.6(c)) we observe that between 300K and 180 K the resistance decreases with temperature, between 180K and 100K the resistance increases while lowering temperature reaching a maximum at 100 K and then starts to decrease again. The resistance of a tunnel barrier should slightly increase when decreasing temperature, this resistance plus the series resistance of the electrodes explains the R vs. T measurement up to the maximum in 100K. This maximum indicates that there is some part in the MTJ that has an insulator to metal transition at this temperature. Probably this insulator to metal transition happens at the LSMO/LFO (bottom) interface. As mentioned in section 2 this interface is more disordered than the top one and may present Mn-Fe intermixing, if this where the case this interfacial region may well have an insulator to metal transition around 100 K [35]. Another interesting feature in these measurements is that the resistance measured at 2 different voltages has different values, implying a non linear I-V characteristic, at temperatures below 150K. In the case of the tunnel barrier of 15 u.c. (Figure 5.6(d)) we observe that junction resistance increases when lowering temperature showing and insulating behavior. The fact that resistance increases by 4 orders of magnitude when lowering the temperature is indicating that the transport in this junction is probably assisted by defects.

5.2.2 Current vs. voltage

Ideally, the I-V characteristic of a tunnel junction has a cubic dependence on voltage at low bias [37]. Usually, instead of the I-V characteristic, the conductance is plotted, in this case the dependence is parabolic (see appendix B). In Figure 5.7 we show I-V measurements at a temperature of 3K for the 3 samples. In the sample with a 3 u.c. barrier (Figure 5.7(a)) the I-V characteristic is linear, this reveals that there is no tunnel barrier in this case. The junction resistance is low (~ 200Ω), this is consistent with the R vs T measurements in this sample (see above). The samples with 9 and 15 u.c. barrier (Figure 5.7 (b) and (c)) showed a non linear behavior. Nevertheless the very high values of resistance in the sample with 15 u.c. at low temperature compared to room temperature point to a transport mechanism different than the tunneling regime. So, from this point on we center our analysis only in the sample with 9 u.c. barrier.

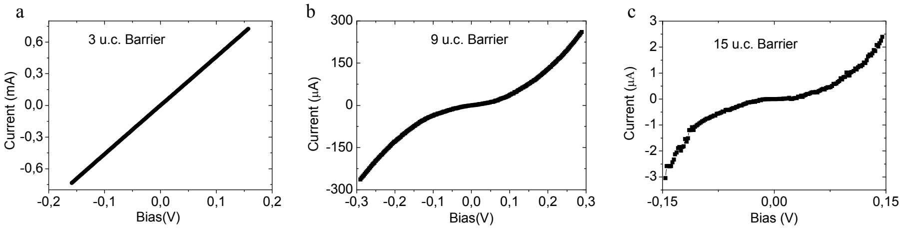

Figure 5.7. (a-c) Current – Voltage characteristics of [$LSMO_{90}$/LFO_M/$LSMO_{20}$] magnetic tunnel junctions where the barrier thickness is M = 3, 9 and 15 u.c. respectively. All the measurements are done at T = 3K.

In Figure 5.8 (a) we show conductance (obtained as the numerical derivative of current density vs. voltage) as a function of temperature of a junction with an area of $24\mu m^2$. We observe the characteristic parabolic dependence of the conductance of a tunnel junction. In Figure 5.8(b) we show the conductivity of the junction at 100K and the parabolic fits. We want to stress two characteristics of these curves: first there is no zero bias anomaly [23, 24], and second the conductance curves are symmetric at all temperatures. We have used the Simmons model [38] (see also appendix B) to extract the barrier thickness and height. We fitted the conductance curves in two different ranges. We did a first fit considering measurements were the applied voltage was below 50 mV and a second fit considering voltages below 150 mV; a summary of the results is shown in Table 5.1. The barrier thickness obtained from the fit is between 2.5 and 3 nm in good agreement with what it is expected. The obtained values of the barrier height, between 0.12eV-0.20 eV, are smaller than the 0.2-0.4 eV found in for example STO/$La_{0.7}Ca_{0.3}MnO_3$[34].

Temperature	V_{max}	Barrier thickness	Barrier height
100 K	150 mV	3.1 nm	0.17
100 K	50 mV	3.5 nm	0.15
70 K	150 mV	3.0 nm	0.18
70 K	50 mV	3.5 nm	0.13
50 K	150 mV	2.9 nm	0.19
50 K	50 mV	3.6 nm	0.11
30 K	150 mV	2.7 nm	0.2
30 K	50 mV	3.4 nm	0.13

Table 5.1. Obtained values for the barrier thickness and barrier height from fitting the current voltage characteristic of a [$LSMO_{90}$/LFO_9/$LSMO_{20}$] magnetic tunnel junction at different temperatures. The fitting was performed taking voltage values up to 150 mV and 50 mV as indicated.

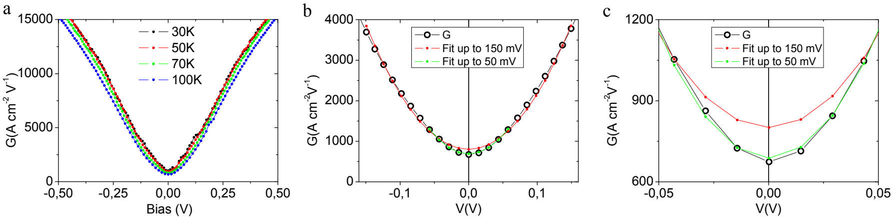

Figure 5.8. (a) Conductance as a function of applied bias of a [$LSMO_{90}/LFO_{9}/LSMO_{20}$] magnetic tunnel junction measured at four different temperatures (shown in the figure). (b),(c) The conductance of the figure (a) measured at T = 100 K (black dots) and parabolic fits. The fits were made considering data up to 50 mV (green), and 150 mV (red).

5.2.3 Magnetoresistance

We have measured the resistance versus magnetic field sweeps in MTJs patterned in the [$LSMO_{90}$ (35nm)/LFO_{9} (3.5 nm)/$LSMO_{20}$ (8nm)]. In these measurements the field was set to 5kOe at the beginning to saturate the magnetization of both electrodes (parallel alignment) and then the magnetic field was swept following the sequence 5000→ -5000 → 5000 Oe. Several junctions were measured at different temperatures.

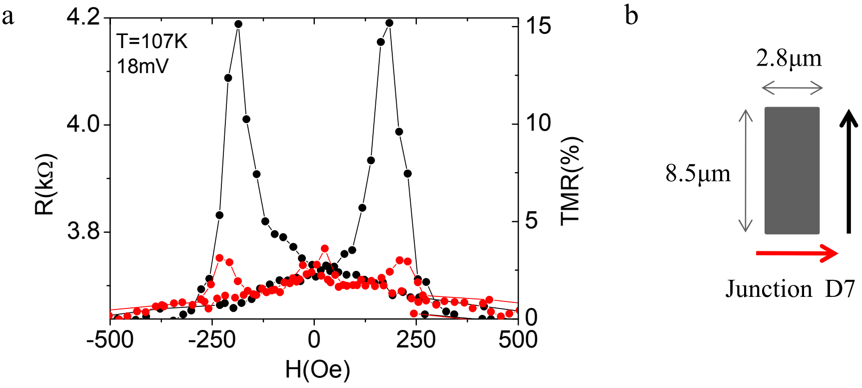

Figure 5.9. (a) Magnetoresistance loop of a [$LSMO_{90}/LFO_{9}/LSMO_{20}$] magnetic tunnel junction measured at T = 107 K with the applied magnetic field along the long side of the rectangular junction (black) and the short side of the rectangular junction (red) as indicated in the schematic of the top view of the junction (b).

It was found that only rectangular shaped junctions present appreciable (more than 5%) magnetoresistance (MR). Moreover, the alignment of the junction and the field was found to be critical. The fact that only rectangular shaped junctions display MR is a consequence of the magnetic anisotropy of the layers. As mentioned in section 3.2 the easy axis of magnetization of both layers is displaced 45º consequently is difficult to achieve an antiparallel alignment between the layers. In rectangular shaped junctions the shape anisotropy in top and bottom electrode contributes to align the magnetization of the sample along the long axis of the junction. Thus if MR is measured with the applied magnetic field parallel to the long side of the rectangular junction we obtain high values of TMR (Figure 5.9 – black dots). On the other hand, in the case of measuring with the field perpendicular to the long axis of the junction very small values of TMR are obtained (Figure 5.9 – red dots). In Figure 5.9 we show the TMR measured at 110K and 1 mV bias with the magnetic field aligned with the long axis of the junction (cyan) and with different angles between the field and this optimal orientation: 5º (red), 15º (black) and 20 º(dark yellow). The alignment of the magnetic field and the easy magnetization axis is so critical that a deviation of 15º reduces the MR from 25% to 10% as observed in Figure 5.9. All the measurements shown below were done taking care of proper alignment of the sample and magnetic field.

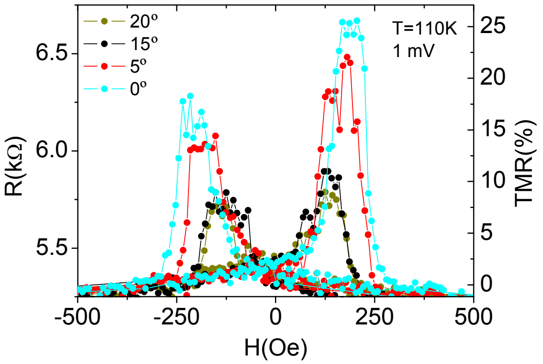

Figure 5.10. Magnetoresistance loop of a [$LSMO_{90}/LFO_{9}/LSMO_{20}$] magnetic tunnel junction measured at T = 110 K. The magnetic field is applied with different angles measured from the long side of the rectangular junction (0º) as indicated in the figure.

In Figure 5.11 we show MR loops measured with an applied bias of 1 mV and at different temperatures (indicated in the figure). We studied the evolution of the MR with temperature and we show in Figure 5.12(a) the results. It is remarkable that MR shows a maximum at 100K, this is the same temperature at which this junction displays a maximum in resistance. As described in the introduction manganite based junctions usually display a TMR that increase monotonically while decreasing temperature. In this sense the behavior observed between 150K and 100K is the expected. This would imply that T^* (the temperature at which TMR vanishes) for this junction is 150K. This sets a lower bound for the Curie temperature of the top electrode. The decrease in TMR when lowering temperature further than 100K is unexpected, and anomalous. The fact that the maximum in TMR occurs at the same temperature as the maximum of resistance of this junction suggests that there may exist some relation between TMR and resistance. It is possible that a phase transition at the barrier occurs at this temperature and affects the TMR values, but we need further experiments to elucidate this point. As far as we know this behavior in manganite based junctions has been previously observed in $La_{0.7}Ca_{0.3}MnO_3/PrBa_2Cu_3O_7/La_{0.7}Ca_{0.3}MnO_3$ junctions only (Sefrioui *et al.*, private communication). Although $PrBa_2Cu_3O_7$ and LFO are very different materials they share some common features: both materials present an AF phase and both are charge transfer type insulators.

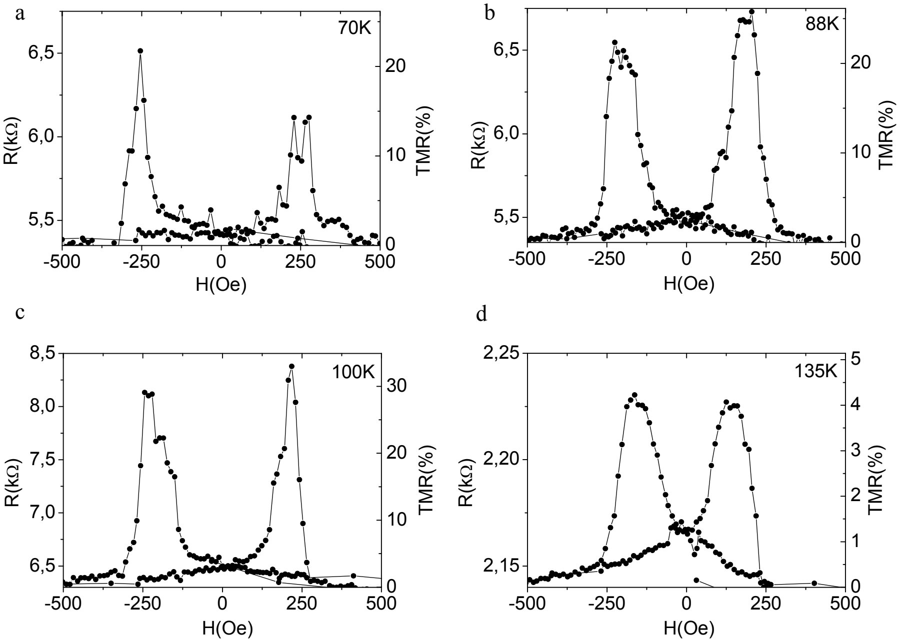

Figure 5.11. (a-d) Magnetoresistance loop of a [$LSMO_{90}/LFO_{9}/LSMO_{20}$] magnetic tunnel junction measured at T = 70, 88, 100 and 135 K.

We analyzed the TMR dependence on the applied bias. At 100K the TMR decreases with increasing bias, the black curve in Figure 5.12 (a) is calculated measuring I-V characteristics in parallel and antiparallel configuration of the electrodes, the red dots are TMR values obtained from MR loops to confirm the validity of the above mentioned procedure. This analysis was performed at different temperatures (Figure 5.12(b)). At 100 K the bias dependence of the TMR is the expected for a manganite based MTJ. When lowering the temperature the measurements became noisier and an apparent decrease in TMR at low bias is observed.

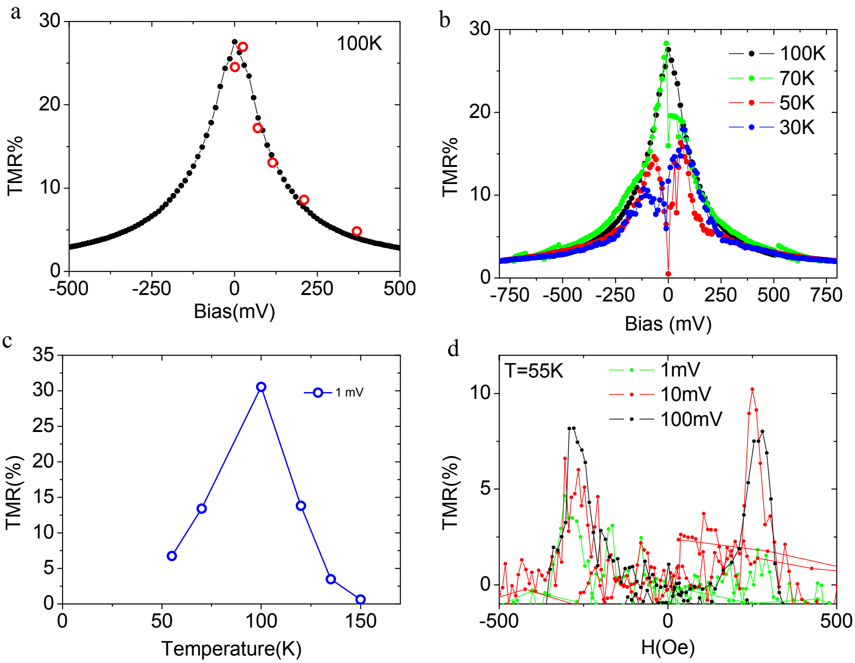

Figure 5.12. (a) Tunneling magnetoresistance of a [LSMO$_{90}$/LFO$_9$/LSMO$_{20}$] magnetic tunnel junction measured as a function of the applied bias at T =100 K. The values are obtained from magnetoresistance loops (red dots) and from current voltage characteristics measured in parallel and antiparallel configuration (black dots). (b) TMR of the same junction at different temperatures as indicated in the figure. (c) TMR as a function of temperature of the same junction. (d) Magnetoresistance loops measured at T = 55 K and at different bias (indicated in the figure).

To further study this behavior we measured MR loops at 55K at 1, 10 and 100 mV. We show in Figure 5.12(d) TMR vs. H instead of R vs H plot to be able to show the measurements at different bias in the same scale. It is clear that TMR at 1 mV is only 2-3 % and is lower than the MR at 10 and 100 mV, this confirms the general trend seen in Figure 5.12(b) that at very low bias (< 5mV) the TMR is small. Nevertheless the figure also illustrates the difficulty in determining a unique TMR value at higher biases ~ 10mV, in this case TMR varies from 10% measured at H=250 Oe to 5% at -250 Oe. Not only that, but the TMR at 100 mV can be higher (H=-250 Oe) or lower (H=250 Oe) than that at 10 mV. There is no doubt that the fact that a good AP alignment is not realized has influence on the these observations but is not the only cause because at higher bias well defined MR peaks are observed. This suggests that this anomalous lowering of the TMR at low temperatures can be influenced by the electric field (bias), although the mechanism of this interaction is not clear. The bias dependence of the TMR observed at low temperatures is similar to the one observed in spin filtering devices [39]. To further explore this possibility we performed measurements on LSMO/LFO/Au junctions.

6 LSMO/LFO/Au Heterostructures

As mentioned in section 5, a magnetic tunnel junction consists of two ferromagnetic electrodes and an insulating barrier. In that situation TMR is observed depending on the orientation of top and bottom electrode. This effect is demonstrated in section 5.2.3. A different phenomenon called spin-filter tunneling occurs in devices with a FM electrode/FM barrier/normal metal [39]. In these devices the exchange splitting of the conduction band creates two different tunnel barrier heights. Because the tunnel current density depends exponentially on the corresponding barrier heights, even with a modest difference in barrier heights, the tunnel probability for spin-up and spin-down electrons will be very different thus producing big MR effects. To explore the possibility of spin filtering effect we replaced one of the magnetic electrodes in the MTJ by Au. If the LFO behaves as an insulating non ferromagnetic barrier, then no MR should be observed. However, if MR is observed this would indicate the presence of a ferromagnetic barrier or at least of an induced magnetic moment in the barrier.

6.1 Magnetotransport

We performed magnetotransport measurements on junctions fabricated by nanoindentation lithography [40] on [LSMO (35nm)/ LFO (2.7nm)/ Au]. The junctions defined by this process have an area of ~100 nm^2, although it is not possible to exactly assess this value.

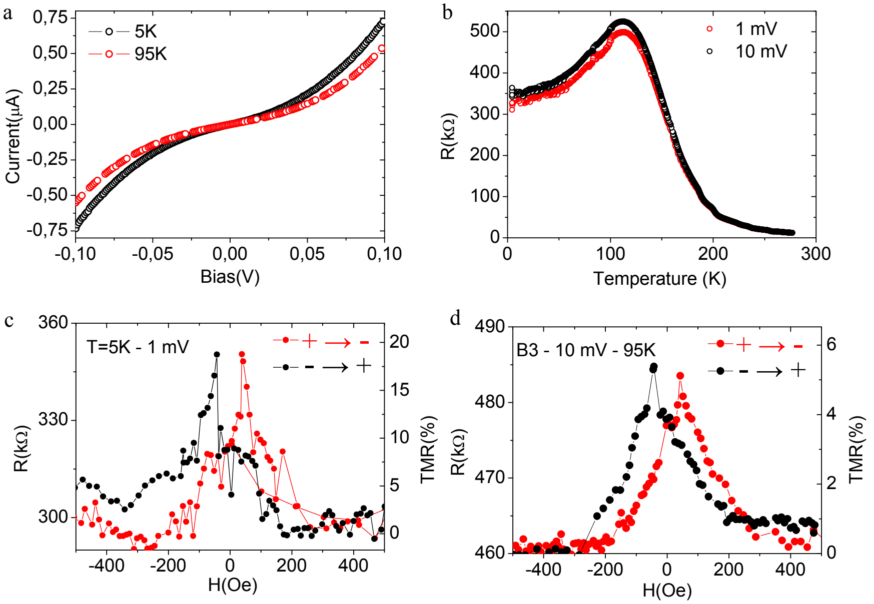

Figure 5.13. Measurements performed on a [LSMO$_{90}$/LFO$_{9}$/Au] nanojunction. (a) Current - Voltage characteristics at T= 5 (black) and 95 K (red). (b) Resistance as a function of temperature measured with 1 mV applied bias (red) and 10 mv applied bias (black). (c-d) Magnetoresistance loops measured at 5 K and 95 K respectively. The field is swept from 5 kOe to -5 kOe (red) and from -5kOe to 5 kOe (black).

In Figure 5.13 (a) we show the I-V characteristics obtained at 95K (red) and 5K (black) were the non-linear behavior associated with tunneling is observed. The resistance vs. temperature measurement of the nanojunction (Figure 5.13(b)) displays a similar behavior than the MTJ (section 5.2.1). This, together with the fact that the bottom electrode is metallic in all the temperature range demonstrates that the maximum in resistance observed at 100 K is related to the LSMO/LFO interface. The resistance vs. magnetic field measurements gives completely unexpected results. In fact a clear MR effect is observed and reaches 5% when measured at 10 mV and 95K, and 15% at 5K and 1mV (Figure 5.13(c) and (d)). In the absence of a ferromagnetic top electrode we ascribe this MR to an induced magnetic moment either on the LFO tunnel barrier or in the LSMO/LFO interfacial region. However the MR peaks appear for positive (negative) magnetic field when changing the field from positive to negative (negative to positive). This is exactly opposite to what is observed in conventional MTJs. One can imagine that there is an interfacial region in the junction which has a net magnetic moment but is weakly AF coupled with the ferromagnetic electrode. In this way a strong positive magnetic field would align both layers (minimum resistance) when the applied field is low but still positive the AF coupling will make the interfacial region flip and a maximum in MR will arise (see Figure 5.14). The idea of an induced magnetic moment at the interface of a non-ferromagnetic material was extensively discussed in chapter 4. Moreover it was shown in ref [41] that a magnetic moment was induced in a $La_{0.3}Ca_{0.7}MnO_3$ tunnel barrier. Here the particularity of this experiment is that $La_xSr_{1-x}FeO_3$ is not ferromagnetic for any value of the doping level x, yet the appearance of MR in the nanojunctions proves that there is a net ferromagnetic moment induced in the interfacial LFO region. An alternative explanation that does not require the presence of ad induced magnetic moment in LFO is the following. Although LFO is an antiferromagnet, the (100) planes may present uncompensated magnetic moments. These uncompensated moments at the interface may be switched with the applied magnetic field, notice that this is not implying that LFO is ferromagnetic. However it is known that the interface states have a great influence on the tunneling probabilities, so the relative alignment of the uncompensated moments in LFO with the ferromagnetic electrode may determine the transport properties of this tunneling junction.

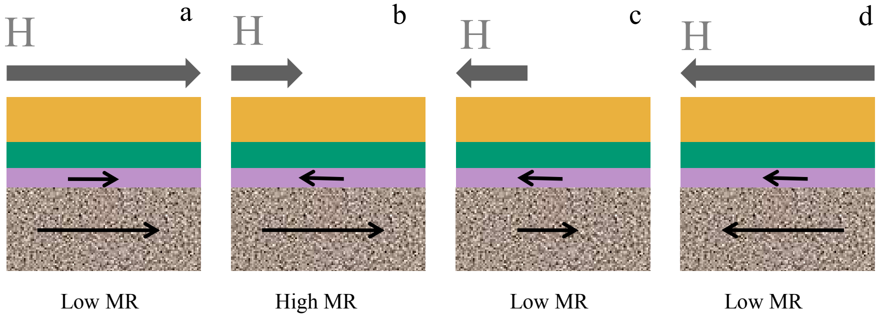

Figure 5.14. Schematic of the [$LSMO_{90}/LFO_9$/Au] nanojunction. The different materials are: LSMO (grey), LFO (green), Au (yellow) and LSMO/LFO interfacial region (purple). The grey thick arrows indicate the applied magnetic field. The thin black arrows indicate the magnetization of the layers.

7 Discussion

In this chapter we have shown that LFO is a suitable material to fabricate tunnel barriers in manganite based MTJs. Moreover the AF character of LFO gave us the possibility of studying the behavior of an AF material as tunnel barrier. Although relatively high values of TMR were obtained, this TMR vanished with temperature at much lower values than expected for an LSMO electrode with T_c=350K. Nevertheless, interesting features in LSMO/LFO/LSMO MTJs were observed like the absence of the ZBA and the non-monotonic behavior of TMR with temperature. Although it may seem counterproductive to use an AF material as a tunnel barrier because it lowers the interfacial T_c of the manganite due to the competition of F and AF order parameters at the interface, new possibilities have emerged from this competition. We were able to use the induced magnetic moment in the interfacial LFO region due to interaction with LSMO to create a spin filtering (LSMO/LFO/Au) device. It remains to be seen if this net moment is an induced moment on the LFO barrier or if the interfacial $La_{0.7}Sr_{0.3}Mn_{1-x}Fe_xO_3$ is acting as a magnetic barrier.

7.1 Perspectives

No doubt more experiments are needed to explore the magnetotransport properties of LSMO/LFO/Au nanojunctions. The behavior of the MR with bias should be measured to look for further confirmation of the spin filtering effect. A second set of experiments that should be carried out are measurements of the magnetic properties of the LSMO/LFO interface. X-ray magnetic circular dichroism and polarized neutron reflectometry appears as two ideal candidates to confirm the induced magnetic moment in LFO.

8 Sample summary

Sample	Type	Thickness LSMO		Thickness LFO	
		nm	(u.c.)	nm	(u.c.)
SFL19a	superlattice	2.7	7	2.7	7
SFL14a	superlattice	3.5	9	2.7	7
SFL15a	superlattice	4.7	12	2.7	7
SFL17a	superlattice	5.8	15	2.7	7
BLF8a1	bilayer	12	31	2.7	7
BLF9a1	bilayer	12	31	3.1	8
BLF11a1	bilayer	12	31	2	5
BLF13a1	bilayer	12	31	4.3	11
BLF14a1	bilayer	35	90	3.5	9
BLF16a1	bilayer	35	90	1.2	3
BLF17a1	bilayer	35	90	5.8	15
BLF18a1	bilayer	35	90	2.7	7
BFL9a1	bilayer	8	20	3.5	9
LSMO48a1	Thin Film	12	31	-	-
TLFL4a1	trilayer	35/8	90/20	3.5	9
TLFL5a1	trilayer	35/8	90/20	5.8	15
TLFL9a1	trilayer	35/8	90/20	1.2	3

9 References

[1] J. M. D. Coey, M. Viret, and S. von Molnar, Adv. Phys. **48**, 167 (1999).

[2] Y. Lu, X. W. Li, G. Q. Gong, G. Xiao, A. Gupta, P. Lecoeur, J. Z. Sun, Y. Y. Wang, and V. P. Dravid, Phys. Rev. B **54**, R8357 (1996).

[3] M. Bibes, and A. Barthelemy, IEEE Trans. Electron Devices **54**, 1003 (2007).

[4] M. Bibes, J. Villegas, and A. Barthelemy, Adv. Phys. **60**, 5 (2011).

[5] J. Park, E. Vescovo, H. Kim, C. Kwon, R. Ramesh, and T. Venkatesan, Nature (London) **392**, 794 (1998).

[6] Y. Lu, X. Li, G. Gong, G. Xiao, A. Gupta, P. Lecoeur, J. Sun, Y. Wang, and V. Dravid, Phys. Rev. B **54** (1996).

[7] J. Z. Sun, W. J. Gallagher, P. R. Duncombe, L. Krusin-Elbaum, R. A. Altman, A. Gupta, Y. Lu, G. Q. Gong, and G. Xiao, Appl. Phys. Lett. **69**, 3266 (1996).

[8] M. Viret, M. Drouet, J. Nassar, J. P. Contour, C. Fermon, and A. Fert, Europhys. Lett. **39**, 545 (1997).

[9] M. Bowen, M. Bibes, A. Barthelemy, J.-P. Contour, A. Anane, Y. Lemaitre, and A. Fert, Appl. Phys. Lett. **82**, 233 (2003).

[10] M. Julliere, Phys. Lett. A **54**, 225 (1975).

[11] J. Sun, L. Krusin-Elbaum, P. Duncombe, A. Gupta, and R. Laibowitz, Appl. Phys. Lett. **70**, 1769 (1997).

[12] P. Lyu, D. Y. Xing, and J. Dong, Phys. Rev. B **60**, 4235 (1999).

[13] T. Obata, T. Manako, Y. Shimakawa, and Y. Kubo, Appl. Phys. Lett. **74**, 290 (1999).

[14] J. O'Donnell, A. Andrus, S. Oh, E. Colla, and J. Eckstein, Appl. Phys. Lett. **76**, 1914 (2000).

[15] M. Jo, N. Mathur, N. Todd, and M. Blamire, Phys. Rev. B **61**, 14905 (2000).

[16] J. M. De Teresa, A. Barthelemy, A. Fert, J. P. Contour, F. Montaigne, and P. Seneor, Science **286**, 507 (1999).

[17] J. H. Park, E. Vescovo, H. J. Kim, C. Kwon, R. Ramesh, and T. Venkatesan, Phys. Rev. Lett. **81**, 1953 (1998).

[18] J. Sun, D. Abraham, R. Rao, and C. Eom, Appl. Phys. Lett. **74**, 3017 (1999).

[19] M. Bibes, L. Balcells, S. Valencia, J. Fontcuberta, M. Wojcik, E. Jedryka, and S. Nadolski, Phys. Rev. Lett. **87**, 67210 (2001).

[20] M.-H. Jo, N. D. Mathur, J. E. Evetts, M. G. Blamire, M. Bibes, and J. Fontcuberta, Appl. Phys. Lett. **75**, 3689 (1999).

[21] M. Izumi, Y. Ogimoto, Y. Okimoto, T. Manako, P. Ahmet, K. Nakajima, T. Chikyow, M. Kawasaki, and Y. Tokura, Phys. Rev. B **64**, 064429 (2001).

[22] J. Sun, T. Palstra, J. Evetts, J. Coey, and J. Cooper, Philosophical Transactions: Mathematical, Physical and Engineering Sciences **356**, 1693 (1998).

[23] M. Bowen, A. Barthélémy, M. Bibes, E. Jacquet, J. Contour, A. Fert, F. Ciccacci, L. Duo, and R. Bertacco, Phys. Rev. Lett. **95**, 137203 (2005).

[24] R. Gu, L. Sheng, and C. Ting, Phys. Rev. B **63**, 220406 (2001).

[25] N. D. Browning, M. F. Chisholm, and S. J. Pennycook, Nature (London) **366**, 143 (1993).

[26] L. Kourkoutis, D. Muller, Y. Hotta, and H. Hwang, Appl. Phys. Lett. **91**, 163101 (2007).

[27] M. Izumi, Y. Ogimoto, Y. Konishi, T. Manako, M. Kawasaki, and Y. Tokura, Mater. Sci. Eng., B **84**, 53 (2001).

[28] A. Berkowitz, and K. Takano, J. Magn. Magn. Mater. **200**, 552 (1999).

[29] H. Kumigashira, D. Kobayashi, R. Hashimoto, A. Chikamatsu, M. Oshima, N. Nakagawa, T. Ohnishi, M. Lippmaa, H. Wadati, and A. Fujimori, Appl. Phys. Lett. **84**, 5353 (2004).

[30] M. Izumi, Y. Murakami, Y. Konishi, T. Manako, M. Kawasaki, and Y. Tokura, Phys. Rev. B **60**, 1211 (1999).

[31] M. Mathews, F. Postma, J. Lodder, R. Jansen, G. Rijnders, and D. Blank, Appl. Phys. Lett. **87**, 242507 (2005).

[32] N. Nemes, M. Garcia-Hernandez, Z. Szatmari, T. Feher, F. Simon, C. Visani, V. Pena, C. Miller, J. Garcia-Barriocanal, and F. Bruno, IEEE Trans. Magn. **44**, 2926 (2008).

[33] F. Houzé, R. Meyer, O. Schneegans, and L. Boyer, Appl. Phys. Lett. **69**, 1975 (1996).

[34] I. Infante, F. Sánchez, V. Laukhin, A. del Pino, J. Fontcuberta, K. Bouzehouane, S. Fusil, and A. Barthélémy, Appl. Phys. Lett. **89**, 172506 (2006).

[35] A. Tiwari, and K. Rajeev, J. Appl. Phys. **86**, 5175 (1999).

[36] F. Montaigne, J. Nassar, A. Vaures, F. Van Dau, F. Petroff, A. Schuhl, and A. Fert, Appl. Phys. Lett. **73**, 2829 (1998).

[37] J. Bland, and B. Heinrich, *Ultrathin Magnetic Structures III: Fundamentals of Nanomagnetism* (Springer Verlag, 2005).

[38] J. Simmons, J. Appl. Phys. **34**, 1793 (1963).

[39] J. Moodera, T. Santos, and T. Nagahama, J. Phys.: Condens. Matter **19**, 165202 (2007).

[40] K. Bouzehouane, S. Fusil, M. Bibes, J. Carrey, T. Blon, M. Le Du, P. Seneor, V. Cros, and L. Vila, Nano Lett. **3**, 1599 (2003).

[41] Z. Sefrioui, C. Visani, M. Calderón, K. March, C. Carrétéro, M. Walls, A. Rivera Calzada, C. León, R. Anton, and T. Charlton, Adv. Mater. **22**, 5029 (2010).

6

TRANSPORT PROPERTIES OF ALL OXIDE PN JUNCTIONS

Heterointerfaces between transition metal oxides (TMOs) have attracted a great interest for oxide electronic applications in which a broad range of electronic functionalities of TMOs is used to realize devices with novel properties. Diverse devices were fabricated like magnetic tunnel junctions [1] and field effect transistors [2] however it was only in the last 5 years when a large amount of experiments on more simple devices like PN or Schottky junctions were made. The interest in these devices besides the novel properties of TMOs interfaces is its simple structure. Before going for that objective an understanding of the mechanisms governing the transport phenomena across the basic building blocks, PN junctions, has to be developed. With this objective the simple models that explain the behavior of PN junctions made of conventional semiconductors (Si, GaAs, etc) may be used as a first approximation. However, the subtleties of correlated electrons in heterointerfaces of TMOs will emerge to bring new possibilities and at the same time new difficulties in understanding the transport mechanisms. In this chapter we will describe our work on the transport properties of $La_{0.8}Sr_{0.2}CoO_3/SrNb_{0.01}Ti_{0.99}O_3$ (LSCO/NSTO) P-N Junctions [3]. More specifically we will apply two different models to analyze the transport properties of the junctions and we will address the effects of interface states when characterizing these types of junctions.

1 Introduction

The realization of p-n and Schottky junctions fabricated from transition metal oxides (TMOs) [4-6] is a route to change carrier concentration at the interface without the structural distortions and / or chemical disorder characteristic of doping by element substitution. From the applied point of view, devices made of these materials are promising due to the fact that interface properties can be modified by external stimuli, giving rise to a wide variety of phenomena such as magnetoresistance [7], magnetocapacitance [8], electroresistance [9], photocarrier control of ferromagnetism [10], etc. In this context, the study of the electronic properties of the interface is relevant [11, 12] in elucidating the mechanisms governing the aforementioned phenomena. Motivated by the finding of resistive switching phenomenon [13] in transition metal oxides PN junctions and its relation with interfacial defects, we will analyze the role played by interface states in LSCO/NSTO junctions using capacitance measurements at variable frequencies.

1.1 $SrNb_{0.01}Ti_{0.99}O_3$ and $La_{0.8}Sr_{0.2}CoO_3$

The SrTiO3 (STO) is a band insulating material with a band gap of ~3.2 eV and an electron affinity of ~3.9 eV [14]. Single crystals of STO are the most common substrates for the growth of high quality TMO thin films. Its perovskite cubic structure with lattice parameter of 0.39 nm closely matches a wide variety of oxides. Upon being doped with Nb, each atom contributes with one extra electron, and for doping level of $SrNb_{0.01}Ti_{0.99}O_3$ it becomes a degenerate n-type semiconductor with carrier concentration N_d=1.7 x 10 ^{20} cm^{-3}.

The $LaCoO_3$ is a Mott insulating material with a charge transfer gap of ~1eV [15]. Upon being doped with Sr^{2+}, $La_{1-x}Sr_xCoO_3$ develops a “glassy ferromagnetism”, the system evolves from a cluster-glass phase at low Sr doping, to a ferromagnetic state at higher doping. In essence at low doping level the system is separated in ferromagnetic-metallic clusters embedded in an insulating matrix. When doping increases the clusters coalesce and the system becomes ferromagnetic [16]. This transition occurs at a doping level x~0.18-0.20, as is shown in the cobaltites phase diagram (Figure 6.1). The reason to make PN junctions with this material is the possibility of obtaining bias modulated charge transfer, to modify the doping level of LSCO near the interface changing the properties of the system.

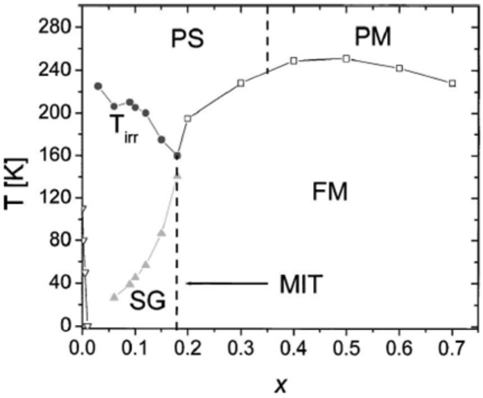

Figure 6.1. Magnetic phase diagram of the $La_{1-x}Sr_xCoO_3$. PS = paramagnetic semiconductor, PM = paramagnetic metal, FM = ferromagnetic metal, SG = spin glass MIT = metal insulator transition.

Another interesting characteristic of the cobaltites is the still controversial spin state of the Co atoms. In $La_{1-x}Sr_xCoO_3$, Co atoms are in a mixed valence state. We will have (1-x) Co^{4+} ions and x Co^{3+} ions. The possible spin states for these ions are shown in Figure 6.2 . It is believed that in the composition $La_{0.8}Sr_{0.2}CoO_3$ the Co ions are in the intermediate spin state [16].

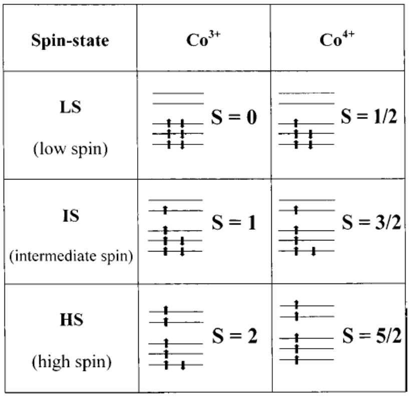

Figure 6.2. The possible spin states of the Co^{3+} and Co^{4+} ions in $La_{1-x}Sr_xCoO_3$. The lower energy levels correspond to the t_{2g} electrons, while the highest levels correspond to e_g states.

2 Sample Growth and Characterization

All the samples in this study have been grown by RF sputtering on STO or $SrNb_{0.01}Ti_{0.99}O_3$ (NSTO) (001) oriented substrates. The pressure during deposition of the thin films and heterostructures was fixed at 2.8 mbar of pure oxygen and the temperature was 750ºC. After deposition the temperature is fixed at 550ºC and the growth chamber is filled with pure oxygen up to P=900 mbar. Following an annealing step of 5 minutes the cool down at 20K/min to room temperature takes place.

2.1 X-ray diffraction

We have used x-ray diffraction experiments to determine the crystalline structure of LSCO and to confirm the c-axis oriented growth of the thin films. In Figure 6.3 (a) and (b) we observe the x-ray reflectivity and diffraction spectra for a series of [$LSCO_N/STO_5$] superlattices consisting of 8 bilayers of N u.c. thick LSCO and 5 u.c. thick STO layers. Many finite size oscillations and superlattice Bragg peaks are observed in these spectra proving the high quality of the LSCO-STO interfaces and c-axis oriented growth of the heterostructures. Figure 6.3 (c) and (d) show reflectivity and diffraction spectra for a LSCO thin film. The thickness of the film obtained from the reflectivity spectra (see chapter 2) is 57 nm. The presence of only [001] Bragg peaks confirms the c-axis oriented growth and allows us to calculate the c lattice parameter obtaining a value of c = 0.379 nm, this lattice parameter is shorter than the pseudocubic lattice parameter of LSCO (0.384nm). This corresponds to an in plane expansion of the lattice parameter to match the substrate lattice parameter (a_{STO} = 0.3905 nm) and an out of plane contraction to conserve the volume of the unit cell.

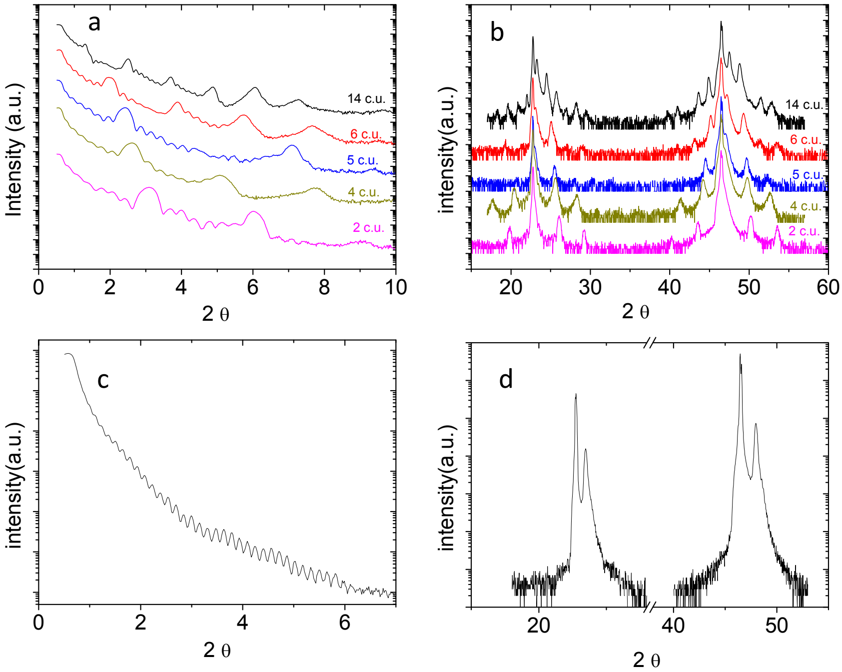

Figure 6.3**.** (a) X-ray reflectivity and (b) X-ray diffraction spectra of $[LSCO_N/STO_5]_8$ superlattices. (c) X-ray reflectivity and (d) X-ray diffraction spectra of a LSCO thin film.

2.2 Scanning Transmission Electron Microscopy

Figure 6.4 displays Z-contrast scanning transmission electron microscopy (STEM) image of a $[LSCO_6/STO_5]$ superlattice. In Figure 6.4 (a) it can be observed in the high magnification STEM images that layers show good epitaxial properties and coherent growth, which is in agreement with the X-ray results. The interface between LSCO and STO is sharp and flat, but presents occasionally one unit cell steps which are indicated by a red arrow in Figure 6.4 (a) and (c). Figure 3 (b) shows low magnification STEM image in which we can observe that the layers are flat over long lateral distances and no precipitates are observed.

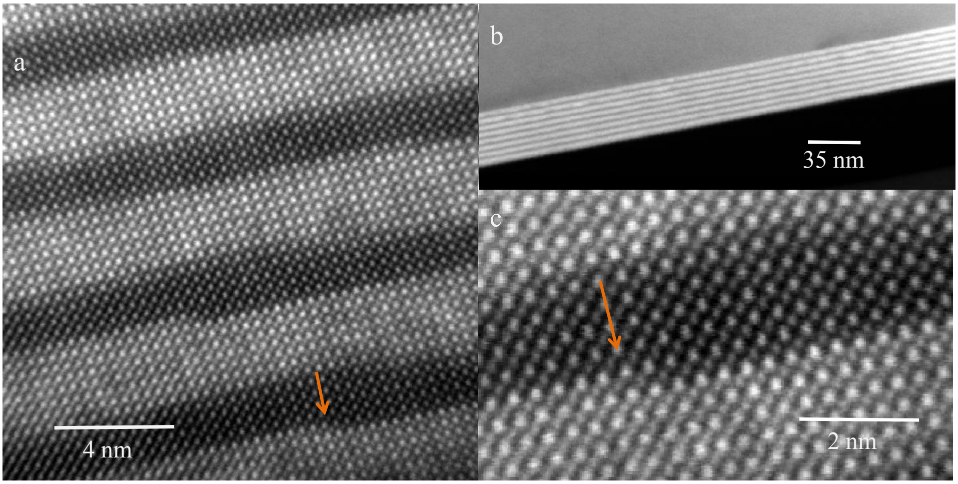

Figure 6.4. Annular dark field scanning transmission electron microscopy image of a [$LSCO_6/STO_5$] superlattice obtained with different magnifications.

2.3 Transport properties

We have measured the resistivity as a function of temperature of an LSCO thin film 57 nm thick deposited on (001) STO substrate. The sample show semiconductive behavior in all the temperature range (Figure 6.5). This may seem to be in conflict with the cobaltite phase diagram nevertheless it is known that in cobaltite thin films the dopant threshold to obtain metallic and ferromagnetic behavior is moved to x=0.22.

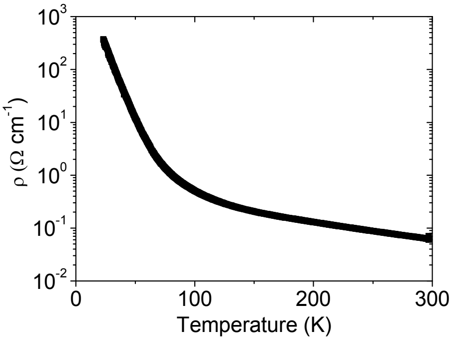

Figure 6.5. Resistivity as a function of temperature of a LSCO thin film measured in Van der Pawn configuration.

3 $La_{0.8}Sr_{0.2}CoO_3$-$SrNb_{0.01}Ti_{0.99}O_3$ PN junctions

We have investigated the transport properties of LSCO-NSTO P-N junctions by measuring the current density-voltage (J-V), capacitance-voltage (C-V) and capacitance-frequency (C-f) characteristics at temperatures ranging from 20K to 280K.

3.1 Junction patterning

We have fabricated P-N junctions by deposition of 57 nm thick LSCO thin film on top of a NSTO substrate. A small area of the substrate is covered during the thin film deposition in order to make electrical contact to the substrate polished surface. Two Al spots were evaporated on the exposed part of the substrate surface. Ag spots of different sizes 0.6-1 mm^2 were evaporated on top of the LSCO thin film. A schematic of the sample and junctions is shown in the inset of Figure 6.6. We fabricated and measured junctions on at least three different samples. In the following we show the electrical transport characteristics of the junctions with the best rectifying properties, the area of this junction is 0.6 mm^2.

3.2 J-V characteristics

We have measured the J-V characteristics of the junctions by grounding the substrate and applying a voltage to the LSCO electrode. Thus we define the forward bias direction as current flowing from the LSCO to the NSTO.

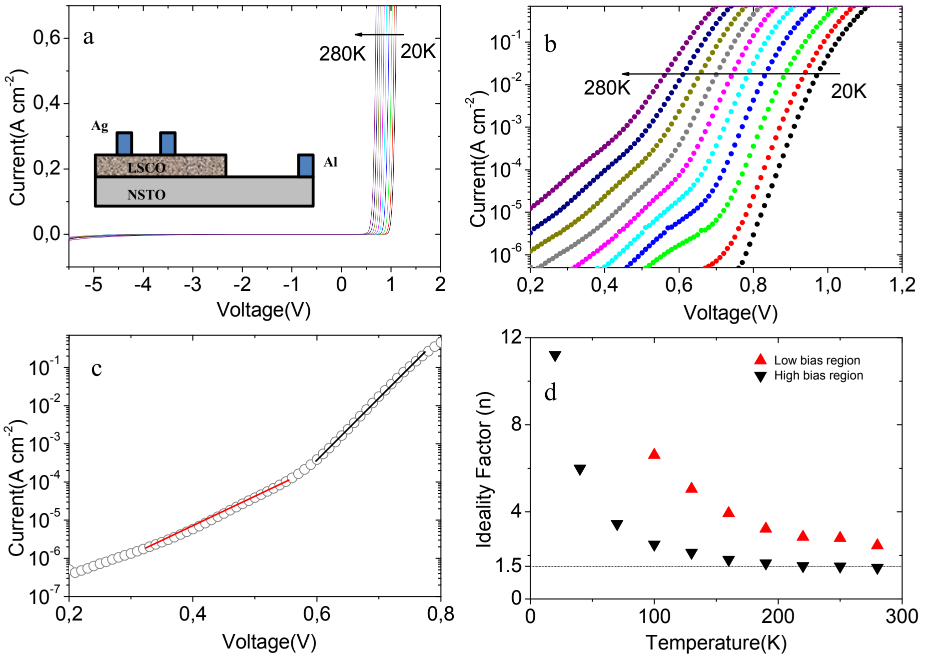

Figure 6.6 (a), (b) Current density as a function of applied voltage for LSCO/NSTO PN junctions measured at temperatures: 20, 40, 70, 100, 130, 160, 190, 220, 250 and 280K. Inset sketch of the heterojunction sample geometry. (c) Current voltage characteristic of the LSCO/NSTO heterojunction measured at 190K, the low bias (red) and high bias(black) regions are indicated. (d) Ideality factor calculated in the low (red) and high (black) bias region.

Figure 6.6 shows temperature dependent J-V characteristics for the LSCO-STNO junction. Good rectifying behaviour is found in the whole temperature range with small current values in reverse bias (J=5 x 10^{-5} A cm^{-2} at V=-0.7 V), as compared to forward bias (J=0.7 A cm^{-2} at V=0.7V).

3.2.1 Abrupt heterojunction model.

In the abrupt pn heterojunction model, when $V>k_BT/q$, we can approximate the forward bias current density (J_F) as [17]

$$J_F = J_S(T)\exp\left(\frac{qV}{nkT}\right), \qquad (6.1)$$

here, $J_S(T)$ is the saturation current density, q is the electronic charge, n is the ideality factor, and k is the Boltzmann constant. In the ideal diffusion mechanism n equals to 1, whereas n equals 2 when current transport is dominated by recombination of charge carriers in the space charge region[17]. Current density is in fact exponential with the forward bias voltage (Figure 6.6 (b)), although for temperatures between 300K and 100K there are two distinct regions at low and high bias with different slopes (Figure 6.6(c)). Figure 6.6 (d) displays the ideality factor obtained from the slopes of the J-V curves. The value n~1.5 obtained in the high bias region at room temperature is similar to that obtained by other authors for other TMO high quality junctions[4]. On the other hand, we obtain n~2.7 in the low bias region at high temperatures. This is the signature of two different mechanisms for current transport, one in the low bias region dominated by recombination of carriers and other in the high bias region dominated by diffusion. At low temperatures, below 130 K, the ideality factor reaches unphysical values, which implies that equation (6.1) is no longer applicable. In this temperature range (20K-100K) the slope of the log J vs. V plot no longer varies as 1/T, actually it is almost temperature independent. This result points to charge carrier tunnelling in the junction, most likely assisted by interface states. This mechanism has been previously observed in a manganite-titanate p-n and Schottky junctions [6, 18]. At temperature above 150 K we can estimate the built-in potential (V_{bi}) in the diffusion regime (high bias) from the temperature dependence of $J_S(T)$ [17, 19]

$$J_S(T) = \frac{A^* q T V_{bi}}{k} \exp\left(-\frac{qV_{bi}}{nkT}\right), \tag{6.2}$$

where we consider the effective Richardson constant A^* to be 156 A cm^{-2} K^{-2}, which corresponds to the effective mass m^*/m_0 = 1.3 for NSTO[20]. In this equation we have introduced the same ideality factor n that was used in equation (6.1). In Figure 6.7 (a) we show the temperature dependence of $J_S(T)$ and in Figure 6.7 (b) we show a plot of log $J_S(T)/T$ vs. 1/T. According to equation (6.2) log $J_S(T)/T$ should be proportional to 1/T, and while at temperatures above 160K the dependence is linear, this no longer holds at low temperatures. This fact together with the observation that the ideality factor increases rapidly below 160K is an indication that probably another mechanism is in action at low temperatures. The calculated built-in potential from the slope of the linear fit in Figure 6.7 (b) is $V_{bi} = 0.65 \pm 0.1$ V.

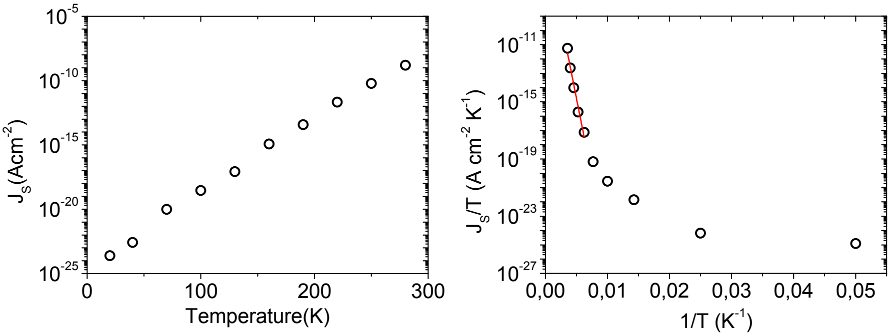

Figure 6.7. (a) Saturation current density as a function of temperature in a LSCO/NSTO pn junction. (b) Saturation current density as a function of inverse tempreature. The red line is a linear fit to points with temperaturas in the range 280K-160K.

3.2.2 Thermally assisted tunneling

The fact that we observe a temperature independent slope in J-V characteristics at low temperature leads us to analyze the J-V characteristics with a different model that is usually applied to Schottky junctions. It may seem strange to apply a model for Schottky junctions to this case but this is justified if we take into account the fact that ($\varepsilon_{LSCOr}/N_{LSCO}$) << ($\varepsilon_{sr}/N_D$), where the relative dielectric constants of LSCO and NSTO, ε_{LSCOr} and ε_{sr}, are about 20 and 150, respectively; N_{LSCO} is the acceptor concentration, equal to 0.2 per unit cell and N_D is the donor concentration, equal to 0.01. Consequently the depletion layer width in the LSCO side will be much smaller than in the NSTO side. This model [21] considers that at low temperatures electrons tunnel between the Fermi level (E_F) of NSTO to the conduction band (CB) bottom of LSCO in forward bias. While at higher temperatures, they are first thermally excited to energy between E_F and the top of the barrier and then tunnel to the CB bottom. The forward bias J-V characteristics are described in this model [21] as

$$J_F = J_S \exp\left(\frac{qV}{E_{00}}\right) \tag{6.3}$$

Where Js depends weakly on the temperature as cT/sin(cT), where c is a constant. E_{00} is given by

$$E_{00} = \frac{qh}{4\pi}\left(\frac{N_d}{m^*\varepsilon_s}\right)^{1/2} \tag{6.4}$$

Where *h* is Planck`s constant, N_d is the donor concentraition, ε_S is the permittivity of NSTO and m^* is the effective electron mass in NSTO. Although the model considers E_{00} a temperature independent parameter, in our case due to the dependence of ε_S with temperature in NSTO [22] we should consider this as a temperature dependent parameter. From equation (6.3) we calculate values of E_{00} between 19 meV and 22 meV in the temperature range 20-100K. In the thermally assisted tunneling regime, the energy of tunneling electrons is distributed around E_m, the peak position of the energy distribution of tunneling electrons, and both E_m and the distribution energy width increase as the temperature increases. Then, the J-V characteristics are given by

$$J_F = J_S \exp\left(\frac{qV}{E_0}\right) \tag{6.5}$$

$$E_0 = E_{00} \coth\left(\frac{E_{00}}{kT}\right) \tag{6.6}$$

Where E_0 approaches E_{00} at low temperatures. As we mentioned before, in our case E_{00} depends on temperature, so we modify equation (6.6) to consider this dependence as follows.

$$E_0 = E_{00}^{eff} \exp\left(\frac{T}{2b}\right) \coth\left(\frac{E_{00}^{eff} \exp\left(T/2b\right)}{kT}\right) \tag{6.7}$$

here we have defined

$$E_{00} = E_{00}^{eff} \exp\left(T/2b\right) \tag{6.8}$$

with the new phenomenological parameter b.

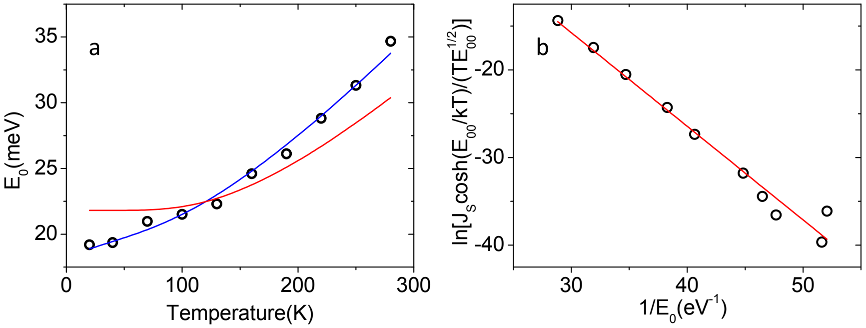

Figure 6.8 (a) Temperature dependence of the E_0 parameter obtained as the inverse of the slope in a ln (J) vs. V plot. (b) ln[$J_S$cosh(E_{00}/kT)/ $E_{00}{}^{1/2}$T] plotted as a function of 1/E_0, the temperature dependent correction on E_{00} is considered (red). Lines are linear fit to the data.

In Figure 6.8 (a) we show the fit of the experimental data to equation (6.6) (red) and (6.7) (blue). It is clear that the equation with the phenomenological introduced term gives a better fit to the data, the obtained parameters are E_{00}^{eff} = 18meV and b = 347K. The obtained values of E_{00} with this modification are: E_{00}(T=300K)= 28 meV and E_{00}(T=20K)=18 meV. Taking into account that N_d=1.7 x 10^{20} cm^{-3} for NSTO we can calculate the permittivity of NSTO from equation (6.4) obtaining ε_{sr}(T=20K) = 140 and ε_{sr}(T=300K) = 60, where we have considered m^*/m^0 = 1.3. This values are in agreement with other published results for the permittivity of NSTO[23, 24]. In the thermally assisted tunneling regime Js is given by

$$J_S = \frac{A^* T^2 \pi^{1/2} E_{00}^{1/2} \left[q\left(\varphi_b - V\right) + \xi \right]^{1/2}}{kT \cosh\left(E_{00}/kT\right)} \exp\left(\frac{\xi}{kT} - \frac{q\varphi_b + \xi}{E_0} \right) \tag{6.9}$$

where ξ is the energy difference between E_F and the CB bottom of NSTO. If ξ is small compared with $q\varphi_b$ (ξ = 6meV for NSTO[18]), the slope of ln[$J_S$cosh(E_{00}/kT)/ $E_{00}{}^{1/2}$T] vs. 1/E_0 plot corresponds to -$q\varphi_b$ according to equation

(6.9). In Figure 6.8 (b) we show the above mentioned plot (black dots), the obtained values for the barrier from the linear is 1.05 V ± 0.1V.

3.3 Capacitance measurements

The depletion capacitance is defined as C = dQ/dV, where dQ is the incremental change in the depletion layer charge for an incremental change in the applied voltage dV. This is the only significant contribution to the capacitance under reverse bias. In the abrupt junction (or Schottky) model the voltage dependence of $1/C^2$ can be expressed as[17]

$$\frac{1}{C^2} = \frac{2\left(V_{bi} - V\right)}{\varepsilon_s N_D} \tag{6.10}$$

where V_{bi} is the built-in potential voltage.

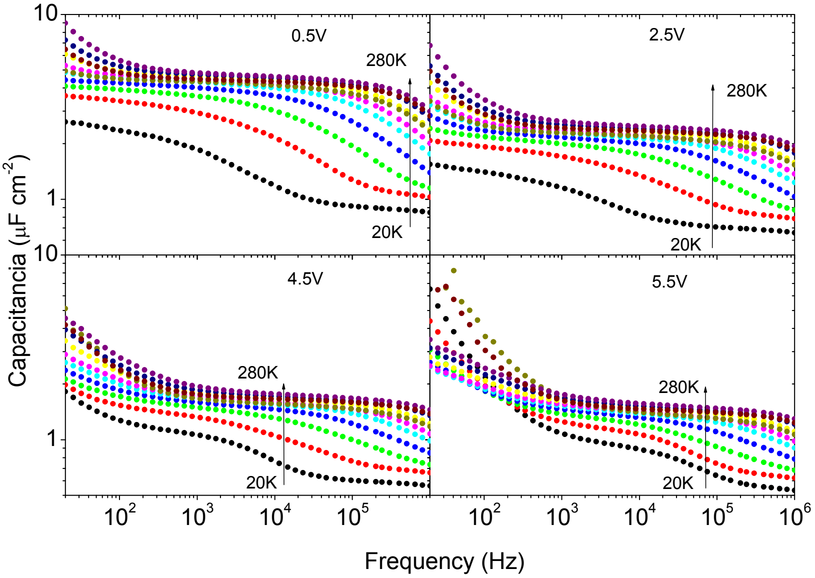

Figure 6.9.Temperature dependent capacitance-frequency characteristics of a LSCO-STNO p-n junction at different reverse bias voltages (indicated in the figures).

Figure 6.9 depicts capacitance-frequency measurements at fixed reverse bias voltage of -0.5 V, -2.5V, -4.5V and -5.5V. A capacitance relaxation is observed at a temperature dependent (but essentially bias independent) frequency. Capacitance relaxations at high frequencies are typically due to charge trapping / detrapping processes at interface states or deep levels. It may also arise from electric field relaxation which occurs at frequencies $f_r \sim 1/2\pi R_s C$, where R_s is the series resistance associated with the junction ($\sim 0.1\Omega$). We estimate this frequency to be $f_r \sim 10^7$ Hz at 20K and even larger at higher temperatures, and since this value is more than 4 orders of magnitude larger than the relaxation frequency observed at this temperature, we can exclude this mechanism as being responsible for capacitance relaxation. The bias independence of the characteristic frequency also excludes deep levels within the space charge region, and points to charge trapped at (electron like) interface states in equilibrium with the electron quasi-Fermi level on the STNO side. On the other hand, the low frequency dispersion of the capacitance below 300Hz for different temperatures depends on the bias voltage, and is most likely due to hole (like) deep levels at the LSCO side. C-V plots will be thus influenced by relaxation phenomena and the use of equation (6.10) may produce unrealistic values of the built in potential. It is thus important to determine the region in which equation (6.10) remains valid.

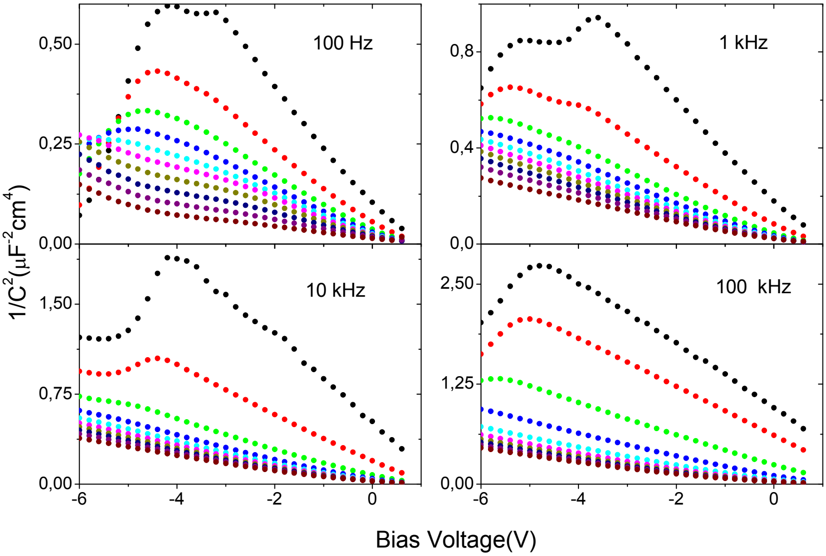

Figure 6.10. Temperature dependent capacitance-voltage characteristics of a LSCO-STNO p-n junction at different frequencies (indicated in the figures).

Figure 6.10 show C-V characteristics at four different frequencies: 100Hz, 1kHz, 10kHz and 100kHz. A linear dependence of $1/C^2$ on V is observed at low values of the reverse bias voltage. We have used linear fits to equation (6.10) between –1 to 0V to obtain (from the intercepts with the voltage axis) the built-in potential, V_{bi}, for each temperature and frequency (Figure 6.11). The unphysical high values below 100 K at frequencies greater that 100 Hz result from the relaxation of the capacitance. Notice, however, that for temperatures above 200K, V_{bi} values obtained with different measurement frequencies (1, 10 and 100 kHz) coincide, providing a measure of V_{bi}, which should be in fact independent of frequency. The value obtained from the 100 Hz measurement is abnormally high as a consequence of the low frequency dispersion of the capacitance (see Figure 6.9). From the above experimental results it is clear that it is not possible to obtain the built-in potential using $1/C^2$ – V characteristics using a single frequency measurement over the whole temperature range. Instead, different frequencies should be used to ascertain the relative influence of the different contributions to the capacitance on the V_{bi} determination. Within the appropriate frequency range (see Figure 6.11), different frequencies provide the same consistent value of the built in potential, V_{bi} =0.6±0.1 V, almost temperature independent.

From the slope on the $1/C^2$ vs V and using equation (6.10) we can calculate the permittivity of NSTO as a function of temperature. At room temperature we obtain ε_{sr} (T=280K) = 20, which should be compared with the value of 60 obtained from J-V measurements or the value of 50 obtained by other authors[25]. However as a function of temperature the permittivity calculated by this method decreases which is in contradiction with the known fact that the permittivity of NSTO increases as temperature is lowered.

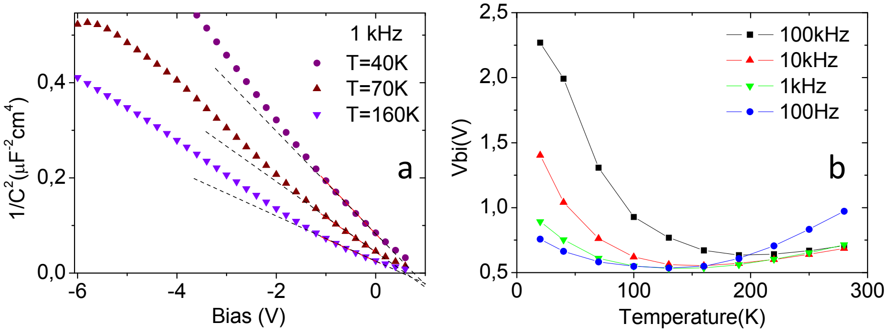

Figure 6.11 (a) Capacitance as a function of bias in a LSCO/NSTO pn junction. Dashed lines are linear fits between -1 and 0V. (b) Built in potential as a function of temperature at different frequencies calculated from equation (6.10).

4 Summary

We have analyzed the transport properties of a non conventional PN junction formed between LSCO and NSTO. The analysis of the J-V characteristics above 150K has yielded a built in potential of $V_{bi} = 0.65 \pm 0.1$ V. We have shown that if the relaxation mechanisms of the depletion capacitance are taken into account the obtained values of V_{bi} from the C-V characteristics are consistent with those obtained in the J-V measurements. This shows that diffusion current dominates the transport properties at high temperatures in the high bias region. However the low temperature data cannot be explained with this model. In view of the temperature independence of the slope of the log J vs. V plots at low temperature we have analyzed these data with a model where the major contribution to the forward bias current is due to electrons tunneling from the CB of the NSTO into LSCO, the tunneling process maybe assisted by interface states. This model allows us to obtain a Schottky barrier of $\varphi_b \sim 1$V. This value should be similar to the built in potential, the large difference between the value of φ_b and V_{bi} tells us that this model does not describe accurately the transport mechanism.

5 References

[1] M. Bibes, J. Villegas, and A. Barthelemy, Adv. Phys. **60**, 5 (2011).

[2] T. Yajima, Y. Hikita, and H. Y. Hwang, Nature Mater. **10**, 198 (2010).

[3] F. Y. Bruno, J. Garcia-Barriocanal, M. Torija, A. Rivera, Z. Sefrioui, C. Leighton, C. Leon, and J. Santamaria, Appl. Phys. Lett. **92**, 082106 (2008).

[4] A. Yamamoto, A. Sawa, H. Akoh, M. Kawasaki, and Y. Tokura, Appl. Phys. Lett. **90**, 112104 (2007).

[5] J. Zhang, H. Tanaka, and T. Kawai, Appl. Phys. Lett. **80**, 4378 (2002).

[6] Y. Xie, J. Sun, D. Wang, S. Liang, W. Lü, and B. Shen, Appl. Phys. Lett. **90**, 192903 (2007).

[7] H. Tanaka, J. Zhang, and T. Kawai, Phys. Rev. Lett. **88**, 27204 (2001).

[8] N. Nakagawa, M. Asai, Y. Mukunoki, T. Susaki, and H. Hwang, Appl. Phys. Lett. **86**, 082504 (2005).

[9] T. Fujii, M. Kawasaki, A. Sawa, Y. Kawazoe, H. Akoh, and Y. Tokura, Phys. Rev. B **75**, 165101 (2007).

[10] H. Katsu, H. Tanaka, and T. Kawai, J. Appl. Phys. **90**, 4578 (2001).

[11] A. Sawa, A. Yamamoto, H. Yamada, T. Fujii, M. Kawasaki, J. Matsuno, and Y. Tokura, Appl. Phys. Lett. **90**, 252102 (2007).

[12] Y. Kozuka, T. Susaki, and H. Hwang, Appl. Phys. Lett. **88**, 142111 (2006).

[13] A. Sawa, Mater. Today **11**, 28 (2008).

[14] J. Robertson, Journal of Vacuum Science & Technology B: Microelectronics and Nanometer Structures **18**, 1785 (2000).

[15] T. Arima, Y. Tokura, and J. B. Torrance, Phys. Rev. B **48**, 17006 (1993).

[16] J. Wu, and C. Leighton, Phys. Rev. B **67**, 174408 (2003).

[17] S. Sze, and K. K. Ng, *Physics of semiconductor devices* (Wiley-Blackwell, 2007).

[18] T. Susaki, N. Nakagawa, and H. Hwang, Phys. Rev. B **75**, 104409 (2007).

[19] A. Sawa, T. Fujii, M. Kawasaki, and Y. Tokura, Appl. Phys. Lett. **86**, 112508 (2005).

[20] Z. Sroubek, Phys. Rev. B **2**, 3170 (1970).

[21] F. A. Padovani, and R. Stratton, Solid-State Electronics **9**, 695 (1966).

[22] R. Van der Berg, P. Blom, J. Cillessen, and R. Wolf, Appl. Phys. Lett. **66**, 697 (1995).

[23] S. Suzuki, T. Yamamoto, H. Suzuki, K. Kawaguchi, K. Takahashi, and Y. Yoshisato, J. Appl. Phys. **81**, 6830 (1997).

[24] O. Copie, V. Garcia, ouml, C. defeld, Carr, eacute, C. ro, M. Bibes, G. Herranz, E. Jacquet, J. L. Maurice, B. Vinter, S. Fusil, K. Bouzehouane, Jaffr, egrave, H. s, Barth, and A. my, Phys. Rev. Lett. **102**, 216804 (2009).

[25] T. Fujii, M. Kawasaki, A. Sawa, Y. Kawazoe, H. Akoh, and Y. Tokura, Phys. Rev. B **75**, 165101 (2007).

7

Conclusions

In this thesis we explored the electronic and spin reconstruction at complex oxide interfaces. We started in chapter 3 by analyzing the charge transfer that takes place at the interface between the parent compound of the electron doped high temperature superconductor Sm_2CuO_4 and $LaFeO_3$. We demonstrated that electrons are transferred from LFO to SCO. Moreover we showed that an artificial structure is created at the interface where the CuO_2 planes of the SCO meet the LaO planes of the LFO. There, the Cu orbitals hybridize with the orbitals of the O atoms of the LaO plane, as demonstrated by X-ray absorption spectroscopy. As a consequence of this electronic and orbital reconstruction the electronic transport properties of SCO/LFO heterostructures are modified, and these heterostructures, formed by insulating materials, become metallic. The idea that the properties of a heterostructure are modified by an interface reconstruction is again explored in chapter 4. At the $La_{0.7}Sr_{0.3}MnO_3/SrTiO_3$ (LSMO/STO) interface the charge transfer and orbital reconstruction, cause a deep modification of the spin state. We proved that a magnetic moment is induced in STO, a nominally insulating and diamagnetic compound. More precisely, a magnetic moment is induced in the Ti atoms as a consequence of the orbital reconstruction at the LSMO/STO interface. This induced moment in the STO controls the bulk magnetic and transport properties of the superlattices when the titanate layer thickness is below 1 nm. In fact, the so called magnetic dead layer is partially suppressed when the STO layers are ultrathin. In chapter 5 and 6 we explored the possibility of exploiting the interface reconstruction to tailor new device functionalities. We fabricated LSMO/LFO/LSMO magnetic tunnel junctions with a tunneling magnetoresistance of 30%. When we replace one of the magnetic electrodes with a non-ferromagnetic material (Au) to form LSMO/LFO/Au tunnel-junctions, we still obtain magnetoresistance of 15%, which we attributed to spin filtering by a modified magnetic state at the LSMO/LFO interface. Finally, we studied $La_{0.8}Sr_{0.2}CoO_3$/Nb:STO junctions. The transport properties of these junctions at room temperature can be described by conventional semiconductor models. However, when the temperature is lowered deviation from these models caused by interface states and by the complex behavior of STO at low temperatures is observed.

Throughout this thesis we have explored the new physics occurring at the interfaces between complex oxides. We demonstrated that these new properties are not only interesting from a basic science point of view but are also important to design new device-concepts. We learned that orbital reconstruction, charge transfer and spin reconstruction are tools that we can use to create new and exciting functionalities in complex oxides interfaces.

Resumen en Español

EL estudio de las propiedades de las interfases de óxidos complejos es objeto de interés creciente en los últimos años y, de hecho, se puede afirmar que ha dado lugar a una nueva dirección de investigación en Física de Materiales. Estas interfases, debido a su gran complejidad, ofrecen una variedad de ingredientes adicionales (efectos de proximidad, transferencia de carga, desacoplo de valencia, etc.) que se constituyen en un mayor número de grados de libertad a la hora de producir efectos físicos nuevos. Las superredes epitaxiales crecidas alternando dos materiales diferentes con la misma o diferente estructura cristalina son un banco de pruebas para el diseño de materiales artificiales con nuevas funcionalidades. Los avances producidos en las técnicas de fabricación de estas superredes nos permiten el crecimiento de heteroestructuras epitaxiales de óxidos de metales de transición, donde las interfases entre los dos materiales muestran una gran coherencia y una elevada calidad cristalina.

1 Objetivos

El objetivo central de esta tesis es el estudio de propiedades emergentes en interfases entre óxidos complejos. Uno de los ejemplos más notables, y ya conocido cuando se inicio esta tesis doctoral, es el del gas bidimensional de electrones en la interfase entre dos materiales aislantes: el $LaAlO_3$ y el $SrTiO_3$(STO) [1]. Este sorprendente hecho es consecuencia de una reconstrucción electrónica en la interfase que tiene como consecuencia el dopado con electrones del STO. Otro ejemplo sorprendente de reconstrucción electrónica es el que se encuentra en el caso de la interfase $LaTiO_3$ y STO [2, 3]

Conocidos estos casos de fases emergentes en las interfases entre óxidos complejos planteamos el objetivo de esta tesis; esto es, el estudio de propiedades emergentes en interfases entre óxidos complejos utilizando materiales que no se hayan combinado anteriormente, o bien, analizar interfases ya estudiadas con nuevas técnicas experimentales. Más concretamente, en el capítulo 3 estudiamos el dopado del compuesto padre de un superconductor de alta temperatura crítica en una interfase por transferencia de carga. En el capítulo 4 examinamos la "capa muerta" en la interfase $La_{0.7}Sr_{0.3}MnO_3/SrTiO_3$. En el capítulo 5 analizamos la influencia de la interacción ferromagnetico-antiferromagnetico en la interfase $La_{0.7}Sr_{0.3}MnO_3/LaFeO_3$ en uniones magnéticas túnel formadas con el mismo material. En el capítulo 6 estudiamos las propiedades de transportes en heterouniones $La_{0.8}Sr_{0.2}CoO_3/SrTi_{0.98}Nb_{0.02}O_3$.

2 Resultados

Todas las muestras de esta tesis han sido crecidas mediante pulverización catódica (*sputtering*). En todos los casos las muestras crecidas fueron caracterizadas por técnicas de microscopía de transmisión-barrido, difracción de rayos x y microscopía de fuerzas atómicas. Esto permite asegurar la alta calidad estructural de las muestras y, en concreto, de las interfases estudiadas.

En el capítulo 3 estudiamos la posibilidad de dopar con electrones el Sm_2CuO_4 (SCO) en la interfase con $LaFeO_3$. El SCO es un material aislante que al ser dopado con electrones mediante la sustitución de Sm por Ce se vuelve metálico y, eventualmente, superconductor. Hemos demostrado mediante el análisis de espectroscopía de pérdida de energía de electrones que el estado de oxidación del Cu en el SCO corresponde al del cuprato dopado con electrones. El análisis de absorción de rayos-X también demuestra, consistentemente con el primer método, la presencia de electrones extra en el SCO. Finalmente demostramos en este capítulo que las películas delgadas epitaxiales de SCO son aislantes, sin embargo, las heteroestructuras SCO/LFO son metálicas en el rango de temperaturas comprendido entre 150 K y 300K y atribuimos este estado metálico a la capa de SCO cercana a la interfase, dopada con electrones.

En el capítulo 4 analizamos la interfase $La_{0.7}Sr_{0.3}MnO_3/SrTiO_3$ (LSMO/STO). Esta interfase es interesante tanto desde un punto de vista fundamental como tecnológico. El LSMO es un material que presenta magnetoresistencia colosal [4] y, debido a su carácter de medio-metal [5], es empleado en gran cantidad de dispositivos para espintrónica [6]. Uno de los inconvenientes en su utilización en espintrónica es que cuando el LSMO se crece en forma de película delgada las propiedades magnéticas y de transporte se deterioran rápidamente cerca de la interfase. Esto dio origen al término “capa muerta” para referirse a la capa de LSMO que por estar cerca de una interfase no presenta las propiedades de volumen del material. Comenzamos el capítulo con una extensa caracterización estructural de superredes LSMO/STO que nos permiten probar que las interfases en las superredes LSMO/STO estudiadas son de alta calidad estructural. Mediante medidas de magnetotransporte en superredes con espesor fijo de LSMO de 6 celdas unidad y variando el espesor de STO entre 0 y 20 celdas unidad, demostramos que la imanación de saturación de estas muestras es equivalente a la de películas delgadas de LSMO cuando el espesor de STO es inferior a 2 celdas unidad. Mediante técnicas de absorción de rayos x con el haz circularmente polarizado demostramos la presencia de momento magnético en los átomos de Ti en la interfase LSMO/STO. Más aun, mediante técnicas de espectroscopía de pérdida de energía de electrones probamos que en las superredes con capas ultra delgadas de STO, el estado de oxidación del Ti es 3.7+ en vez del esperado 4+. Esto es el resultado fundamental del capítulo y fundamenta nuestra conclusión. En superredes LSMO/STO con capas ultra delgadas de STO existe un acoplamiento magnético entre estas mediado por el STO. La posibilidad de que el STO medie este acoplo magnético existe debido a que como consecuencia de la reconstrucción orbital en la interfase LSMO/STO, el STO está dopado con electrones y el Ti presenta un momento magnético.

Como hemos mencionado, el LSMO es un material muy utilizado en dispositivos de espintrónica debido a su naturaleza medio metálica. Nosotros hemos estudiado en el capítulo 5 de esta tesis la posibilidad de utilizar este material como electrodo en uniones magnéticas túnel $La_{0.7}Sr_{0.3}MnO_3/LaFeO_3/La_{0.7}Sr_{0.3}MnO_3$. El material utilizado como barrera, el LFO, es un material antiferromagnético. Al utilizar este tipo de material como barrera túnel tenemos la posibilidad de estudiar los efectos de la interacción ferromagnético-antiferromagnético en la interfase y sus consecuencias sobre el transporte túnel. Las heteroestructuras LSMO/LFO/LSMO fueron crecidas en el departamento de Física Aplicada III de la U.C.M.. La fabricación de uniones magnéticas túnel mediante técnicas de litografía óptica y las medidas de magnetotransporte se llevaron a cabo en el grupo de óxidos funcionales en el laboratorio "Unite Mixte de Physique CNRS/THALES" durante una estancia de 4 meses. Encontramos que la magnetoresistencia túnel en estas uniones alcanza valores del 30% a una temperatura de 100K. La particularidad de estas uniones es que la magnetoresistencia decrece tanto al aumentar como al disminuir la temperatura. Para estudiar la posible existencia de un momento ferromagnético inducido en la barrera túnel fabricamos uniones tipo $La_{0.7}Sr_{0.3}MnO_3/LaFeO_3/Au$ mediante técnicas de nano litografía [7]. Medidas de magnetotransporte en estas uniones revelan la existencia de magnetoresistencia que alcanza el 15% a una temperatura de 100 K. Aunque este hecho no demuestra la existencia de un momento ferromagnético inducido en el LFO por sí mismo, es un fuerte indicio en este sentido.

En el capítulo 6 estudiamos las propiedades de transporte de heterouniones $La_{0.8}Sr_{0.2}CoO_3/SrTi_{0.98}Nb_{0.02}O_3$ [8]. Demostramos que con estos materiales se pueden fabricar uniones tipo PN con propiedades rectificantes y encontramos una barrera de potencial inducida de 0.9 eV entre la cobaltita y el titanato. El análisis de las curvas de capacidad-tensión (C-V) y capacidad-frecuencia (C-f) a temperatura variable, nos permite identificar la presencia de estados electrónicos en la interfase, "trampas", que influencian el comportamiento de la unión. En el estudio de la capacidad de la unión en función de la frecuencia encontramos una relajación de la capacidad causada por estos estados en la interfase. Demostramos que las curvas de capacidad tensión son un método útil para obtener la barrera de potencial inducido en la unión, siempre que se elija de forma adecuada la frecuencia a la que se mide la capacidad.

3 Bibliografía

[1] A. Ohtomo, and H. Y. Hwang, Nature (London) **427**, 423 (2004).

[2] A. Ohtomo, D. A. Muller, J. L. Grazul, and H. Y. Hwang, Nature (London) **419**, 378 (2002).

[3] S. Okamoto, and A. Millis, Nature (London) **428**, 630 (2004).

[4] A. Urushibara, Y. Moritomo, T. Arima, A. Asamitsu, G. Kido, and Y. Tokura, Phys. Rev. B **51**, 14103 (1995).

[5] J. Park, E. Vescovo, H. Kim, C. Kwon, R. Ramesh, and T. Venkatesan, Nature (London) **392**, 794 (1998).

[6] M. Bibes, J. Villegas, and A. Barthelemy, Adv. Phys. **60**, 5 (2011).

[7] K. Bouzehouane, S. Fusil, M. Bibes, J. Carrey, T. Blon, M. Le Du, P. Seneor, V. Cros, and L. Vila, Nano Lett. **3**, 1599 (2003).

[8] F. Y. Bruno, J. Garcia-Barriocanal, M. Torija, A. Rivera, Z. Sefrioui, C. Leighton, C. Leon, and J. Santamaria, Appl. Phys. Lett. **92**, 082106 (2008).

A

Transition Metal Ions in Crystal Fields

If we consider the transition metal elements from Ti to Cu we found that the electrons are distributed in these atoms with configuration $1s^2\ 2s^2\ 2p^6\ 3s^2\ 3p^6\ 3d^x$ with a varying number of 3d electrons. The radial quantum number n and orbital quantum number l of 3d electrons are n=3 and l=2, respectively. The angular part of the wave function corresponds to the spherical harmonics $Y_m^2(\theta,\phi)$ written here in terms of the spherical polar coordinates. Here, m is the magnetic quantum number and has the value $-2 \le m \le 2$. The 3d states are five-fold degenerate in a spherical potential since 2l + 1 = 5, but they are not in a crystal [1]. In many transition metal oxides, transition metal ions are surrounded by six oxygen ions (O^{2-}), making octahedron as in Figure A.1(a). Oxides with the perovskite crystal structure are examples (Figure A.1(b)).

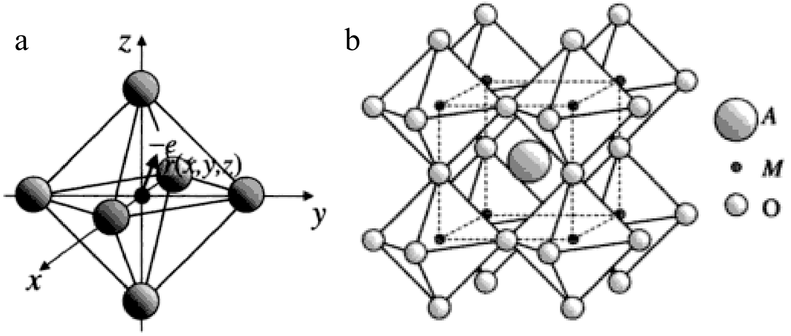

Figure A.1. (a) An electron in the crystal field of the octahedron. (b) Crystal structure of perovskite AMO_3. Adapted from ref [1].

Each O^{2-} ion has a charge distribution with spherical symmetry. Neglecting the overlap of the 3d wave function with the surrounding ions, we treat each ion as a point charge. So, the potential acting on a 3d electron from the surrounding ions is expressed as

$$V(\boldsymbol{r}) = \sum_i \frac{Z_i e^2}{|\boldsymbol{r} - \boldsymbol{R}_i|}, \tag{A.1}$$

where **r** is the position vector of the 3d electron, $\mathbf{R}_i$ and $Z_i e$ denote the position vector and charge of the i-th ion, respectively. The expression in (A.1) is called the crystal field potential. In particular, when the 3d electron is taken to be a point charge, the quantity,

$$V_0 = \sum_i \frac{Z_i e^2}{|\boldsymbol{R}_i|}, \tag{A.2}$$

is called the Madelung potential. In a cubic crystal field, the potential acting on the 3d electron is expressed in rectangular coordinates as,

$$V_4(\boldsymbol{r}) = \frac{5}{2} V_{40} \left(x^4 + y^4 + z^4 - \frac{3}{5} r^4 \right) \tag{A.3}$$

where V_{40} is a constant. In the cubic crystal field given by (A.3), the eigen-functions of a 3d electron are not spherical harmonics but are given by the linear combination of them as follows:

$$\begin{aligned}
d(x^2-y^2) &\propto \sqrt{\frac{2\pi}{5}}(Y_2^2+Y_2^{-2}) = \frac{\sqrt{3}}{2}\frac{(x^2-y^2)}{r^2} \\
d(3z^2-r^2) &\propto \sqrt{\frac{4\pi}{5}}Y_2^0 = \frac{1}{2}\frac{(3z^2-r^2)}{r^2} \\
d(xy) &\propto \frac{1}{i}\sqrt{\frac{2\pi}{5}}(Y_2^2-Y_2^{-2}) = \sqrt{3}\frac{xy}{r^2} \\
d(yz) &\propto \sqrt{\frac{2\pi}{5}}(Y_2^{-1}+Y_2^1) = \sqrt{3}\frac{yz}{r^2} \\
d(zx) &\propto \frac{1}{i}\sqrt{\frac{2\pi}{5}}(Y_2^{-1}-Y_2^1) = \sqrt{3}\frac{zx}{r^2}
\end{aligned} \tag{A.4}$$

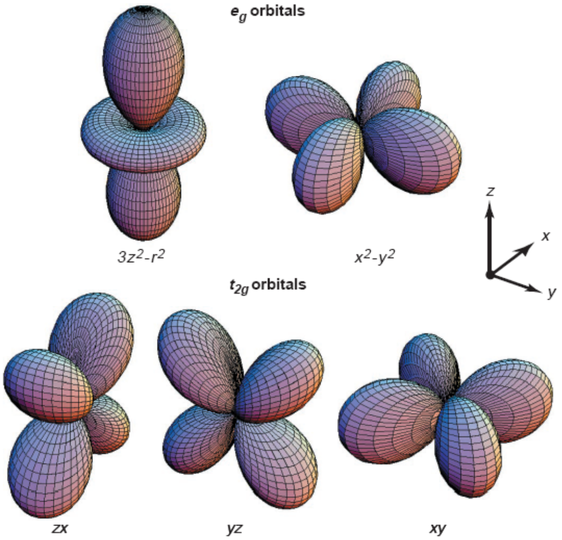

Figure A.2. Five d orbitals in a cubic crystal field. Adapted from ref [2].

In Figure A.2 these five eigen-functions are plotted. In Figure A.**3**, the energy level schemes in spherical, cubic and tetragonal (elongated in the z direction) crystal fields are shown. In a cubic crystal field, the two higher energy states are $d_{x^2-y^2}$ and $d_{3z^2-r^2}$, and are often referred to as the e_g orbitals. The three lower energy states, t_{2g} orbitals, comprise d_{xy}, d_{yz}, and d_{zx}. The e_g orbitals extend towards the oxygen ions which have a negative charge so that a 3d electron in these orbitals has its energy raised by the Coulomb interactions. On the Other hand, the t_{2g} orbitals, point away from the oxygen ions so that electrons in these orbitals have an energy which is less affected by these Coulomb interactions. As a result, the degeneracy is partly removed. The splitting between e_g and t_{2g} orbitals is written as 10Dq. The value of this splitting is about 2-3 eV in typical oxides with perovskite structure.

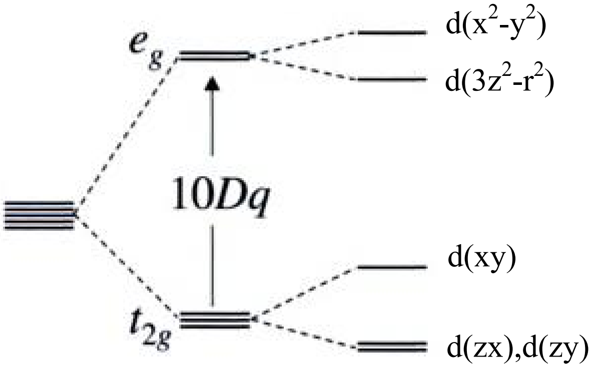

(a) spherical (b) cubic (c) tetragonal

Figure A.3. Energy levels in the crystal fields. (a) Spherical symmetry, (b) cubic symmetry, (c) tetragonal symmetry where the octahedron is elongated along the z direction. Adapted from ref [1].

1 References

[1] S. Maekawa, *Physics of transition metal oxides* (Springer Verlag, 2004).

[2] Y. Tokura, and N. Nagaosa, Science **288**, 462 (2000).

B

Tunneling Basics

In this appendix we will describe the basic physics behind the tunneling phenomenon and some simple models that can be used to obtain parameters of tunnel junctions such us barrier height and barrier thickness through fitting of experimental current – voltage characteristics [1].

1 Electron Tunneling

Electron tunneling is a quantum phenomenon by which an electric current may flow from one electrode, through an insulating barrier, into another electrode. A simple way to understand how tunneling is possible is by considering an electron wave which encounters a potential step, see Figure B.1. Though most of the intensity is reflected at the potential step, a portion decays exponentially through the barrier. For sufficiently thin barriers (typically few nm thick), some intensity remains on the other side of the potential step, and therefore, the electron will have a finite probability of being found on the other side of the potential barrier. The most straightforward realization of this structure is in a metal-insulator-metal (M-I-M) trilayer structure commonly called a tunnel junction, with the insulator typically provided by a metal oxide (e.g. Al_2O_3).

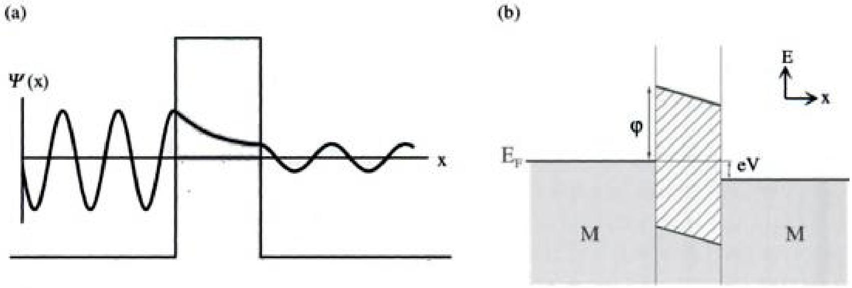

Figure B.1. (a) Tunneling in metal-insulator-metal structures. (a) Electron wave function decays exponentially in the barrier region, and for thin barriers, some intensity remains in the right side. (b) Potential diagram for a M-I-M structure with applied bias eV- Shaded areas represent filled states, open areas are empty states, and the hatched area represents the forbidden gap in the insulator. Adapted from ref [1].

In most studies, tunneling phenomenon in M-I-M structures are studied by observing the current (or its derivative) as a function of applied voltage across the junction. As an illustration, we consider phenomenologically an idealized M-I-M structure, with the electrode-tunnel barrier system modeled as a step potential Figure B.1. Without a voltage across the junction, the two metals will equilibrate, and the Fermi levels will be at the same energies for the two electrodes. When a bias V is applied across the junction, one Fermi level shift by eV with respect to the other, where e is the electron charge Figure B.1. The number of electrons tunneling from one electrode to the other is given by the product of the density of states at a given energy in the left electrode $\rho_l(E)$, and the density of states at a given energy in the right electrode, $\rho_r(E)$, multiplied by the square matrix element $|M|^2$, which is essentially the probability of transmission through the barrier. One must also then multiply by the probabilities that the states in the left electrode are occupied, f(E), and that the states in the right electrode are empty, 1-f(E-eV)), where f(E) is the Fermi-Dirac function. This product is an expression of the requirement that electrons on one side of the barrier must have empty states to tunnel into on the other side of the barrier. For the general case, the tunnel current I from the left electrode (l) to the right electrode (r) is given by:

$$I_{l\rightarrow r}(V)=\int_{-\infty}^{\infty}\rho_l(E)\rho_r(E+eV)\left|M\right|^2 f(E)[1-f(E+eV)]dE \qquad \text{(B.1)}$$

where the subscript l(r) refers to the left (right) electrode. The total tunnel current is then given by $I_{l\rightarrow r}-I_{r\rightarrow l}$. Simmons [2] used the WKB approximation to obtain the matrix elements $|M|^2$ for an arbitrary barrier of average height $\overline{\varphi}$ above the common Fermi level E_F. He then calculated the tunnel current from (B.1), using a free electron relation for $\rho_l(E)$, and approximating the Fermi-Dirac functions as step functions (i.e., T = 0). His well known result for a trapezoidal barrier (Figure B.1) is

$$\begin{aligned} J(V)=&\frac{J_0}{d^2}\left(\overline{\varphi}-\frac{eV}{2}\right)\exp\left[-Ad\sqrt{\overline{\varphi}-\frac{eV}{2}}\right]\\ &-\frac{J_0}{d^2}\left(\overline{\varphi}+\frac{eV}{2}\right)\exp\left[-Ad\sqrt{\overline{\varphi}+\frac{eV}{2}}\right]\end{aligned} \qquad \text{(B.2)}$$

Where J is the tunnel current density, $A=4\pi\sqrt{2m_e^*}/h$ and $J_0=e/2\pi h$ are constants, m^*_e is the electron effective mass, d is the barrier thickness, $\overline{\varphi}$ is the average barrier height above the Fermi level, and V is the applied bias. If we take the barrier thickness in Angstroms, the barrier height in electron Volts, and the bias in Volts, then A = 1.025 $eV^{-0.5}$ $Å^{-1}$ and J_0= 6.2 x 10^{10} eV^{-1} $Å^2$, with the resulting current density J in A/cm^2. This equation, or its variants [3], are often used to fit experimental J(V) characteristics to obtain effective barrier heights and thicknesses [3]. At moderate voltages, Simmons showed that $J \sim \alpha V + \beta V^3$, which leads to one of the hallmark characteristics of tunneling: a parabolic dependence of conductance (G≡dI/dV) on voltage, which is often observed experimentally for tunnel junctions. Nevertheless, any dependence of the current density on the electronic density of states (DOS) in the electrodes is suspiciously absent [4], which is a direct result of the over-simplified model used [5, 6].

2 References

[1] J. Bland, and B. Heinrich, *Ultrathin Magnetic Structures III: Fundamentals of Nanomagnetism* (Springer Verlag, 2005).

[2] J. G. Simmons, J. Appl. Phys. **34**, 1793 (1963).

[3] W. Brinkman, R. Dynes, and J. Rowell, J. Appl. Phys. **41**, 1915 (1970).

[4] W. A. Harrison, Phys. Rev. **123**, 85 (1961).

[5] J. Bardeen, Phys. Rev. Lett. **6**, 57 (1961).

[6] S. Zhang, and P. Levy, Eur. Phys. J. B **10**, 599 (1999).